

8-2021

## TRIM24 promotes mammary tumor development by upregulating metabolic reducing power

Shucheng Miao

Follow this and additional works at: [https://digitalcommons.library.tmc.edu/utgsbs\\_dissertations](https://digitalcommons.library.tmc.edu/utgsbs_dissertations)



Part of the [Medicine and Health Sciences Commons](#)

---

### Recommended Citation

Miao, Shucheng, "TRIM24 promotes mammary tumor development by upregulating metabolic reducing power" (2021). *The University of Texas MD Anderson Cancer Center UTHealth Graduate School of Biomedical Sciences Dissertations and Theses (Open Access)*. 1131.  
[https://digitalcommons.library.tmc.edu/utgsbs\\_dissertations/1131](https://digitalcommons.library.tmc.edu/utgsbs_dissertations/1131)

This Thesis (MS) is brought to you for free and open access by the The University of Texas MD Anderson Cancer Center UTHealth Graduate School of Biomedical Sciences at DigitalCommons@TMC. It has been accepted for inclusion in The University of Texas MD Anderson Cancer Center UTHealth Graduate School of Biomedical Sciences Dissertations and Theses (Open Access) by an authorized administrator of DigitalCommons@TMC. For more information, please contact [digitalcommons@library.tmc.edu](mailto:digitalcommons@library.tmc.edu).

# **TRIM24 promotes mammary tumor development by upregulating metabolic reducing power**

By

Shucheng (Anna) Miao, B.S.

APPROVED:

---

**Michelle Barton, Ph.D.**  
Advisory Professor

---

**Guillermina Lozano, Ph.D.**  
Advisory Professor

---

**Powel Brown, Ph.D.**

---

**Wenbo Li, Ph.D.**

---

**Wenliang Li, Ph.D.**

---

**Sendurai Mani, Ph.D.**

---

APPROVED:

---

Dean, The University of Texas  
MD Anderson Cancer Center UTHHealth Graduate School of Biomedical  
Sciences

**TRIM24 promotes mammary tumor development by upregulating  
metabolic reducing power**

A

Thesis (Dissertation)

Presented to the Faculty of

The University of Texas

MD Anderson Cancer Center UTHealth

Graduate School of Biomedical Sciences

in Partial Fulfillment

of the Requirements

for the Degree of

**Master of Science**

by

**Shucheng (Anna) Miao, B.S.**

Houston, Texas

August, 2021

## **Dedication**

For my parents Xuguang and Zexun



## **Acknowledgment**

Throughout my master's studies and the writing of this dissertation, I have received a great deal of guidance and support. To my supervisors, mentors, committee members, colleagues, friends and families, my plain words are not sufficient to express my gratitude. To my advisor Dr, Michelle Barton, I'm eternally thankful for seeing the potentials in me, always being supportive and patient, and guiding me throughout the amazing exploration in science. She is a true inspiration and a role model that I would want to live up to. I'm also extremely thankful to my co-mentor Dr. Guillermina Lozano, for the opportunities of continuing my studies in her laboratory, the encouragement, and insightful advice. I would like to thank my committee members, Dr. Sendurai Mani, Dr. Wenliang Li, Dr. Powel Brown, and Dr. Wenbo Li – for your positive feedback, challenge questions, critical advice and inspiring scientific discussion.

I would like to thank former Barton lab members, Sabrina Stratton, Kendra Allton, Cem Dede, Dr. Jain Abhinav, Lalit Patel and Patrick Krause who have assisted in my experiment and encouraged me during difficult times. I would especially like to thank Dr. Vrutant Shah, for always helping me find the lead in the tangles and thinking outside the box. I would also like to thank the Lozano lab members, Dr. Xiao Zhao, Dr. Denada Dibra, Dr. Amanda Wasylshen, Peirong Yang, Patty Chau, Dr. Joy McDaniel, Dr. Shubin Xiong, Dr. Vinod Pant, and Dr. Xiaojie Yu for their warm advice and making the workplace enjoyable. I would also like to thank everyone in the CCC2021 team The Guardians, Dhruv Chachad, Rhiannon Morrissey, Jovanka Gencel Augusto and Chang Sun for together exploring the career beyond being bench scientists.

My appreciation also extends to collaborators. I would like to thank Dr. Phil Lorenzi and Lin Tan for helping me with the foundation of my project. I also would like to thank Dr. Adrianna Paulucci, Xiaorui Zhang, Dr. Kevin Roarty and Dr. Hongjiang Si at Baylor Medical College for helping me with the specific experimental techniques. I would also like to thank the G&E community, it's such a privilege to be a member of this big family. I especially thank Elisabeth Lindheim, Dr. Michelle Hildebrandt, Dr. Yejing Ge for organizing events together and their genuine care toward us students during the pandemic. I would also like to thank G&E director Dr. Jichao Chen and co-director Dr. Francesca Cole for their approval of my service to our community.

To my friends at GSBS, Ciara Chen, Cheryl Jiang, Yiming Cai, Pujun Guan, Melanie Woods, Yitao Tang, Lisa Huang, and Zian Liao, having your friendship during my journey means as much as the scientific accomplishments. I'm also deeply thankful to my dear friends Sherry Han, Yan Sun, Cali Zhang, Helen Li, Chuqing Zhang, Rachel Fang for your virtual heart-warming support from a long distance. Words cannot express my gratitude and love for my parents, thank you for being my listeners, confidants, teachers and my motivation. I'm also deeply grateful for the unconditional love from my grandparents, aunts and uncles, and cousins. Last but not least, I would really like to thank the mice for their sacrifice to science; my hamsters Zozo and Zaizai for being my comfort during the lock-down period; and Maomao the cat, for being a cheerful companion during the late-night study.

# **TRIM24 promotes mammary tumor development by upregulating metabolic reducing power**

Shucheng (Anna) Miao, B.S.

Advisory Professors: Michelle Barton, Ph.D.

and Guillermina Lozano, Ph.D.

Metabolic reprogramming is an emerging hallmark of cancer cells. Changes in cellular metabolism can contribute to cancer cell survival and tumor progression. Tripartite motif-containing protein 24 (TRIM24) is an E3 ligase for p53, a nuclear receptor co-regulator, and a histone reader. Over expression of TRIM24 correlates with poor overall survival of breast cancer patients. Previously, our lab created a mouse model that conditionally over-expresses (COE) TRIM24 protein in mammary epithelia (*Trim24<sup>COE</sup>*) and develops carcinosarcoma or metaplastic mammary tumors (70% of all *Trim24<sup>COE</sup>* tumors), a rare and aggressive triple-negative subtype called metaplastic TNBC in humans (MpBC). RNA-sequencing revealed that *Trim24<sup>COE</sup>* mouse mammary tumors have upregulated glycolysis and epithelial-to-mesenchymal transition (EMT). *Trim24<sup>COE</sup>* carcinosarcoma cell-derived spheroids showed irregular, poorly differentiated structures that were more invasive compared to spontaneous, control MMTV-cre mammary tumor-derived spheroids. Using <sup>13</sup>C<sub>6</sub>-glucose/glutamine tracing, we found *Trim24<sup>COE</sup>* spheroids recapitulated some of the metabolic features of *Trim24<sup>COE</sup>* carcinosarcomas like upregulated glycolysis and exhibited aberrantly upregulated antioxidant defenses. We found *Trim24<sup>COE</sup>* spheroids exhibited low intracellular and mitochondrial ROS, an increased NADP(H) pool, and were more resistant to oxidative stress. Quantitative reverse-transcriptase polymerase chain reaction (qRT-PCR) and immunoblotting

validated that enzymes of one-carbon metabolism and *de novo* glutathione synthesis pathways were upregulated in *Trim24*<sup>COE</sup> spheroids and that upregulation was depended on TRIM24 over expression. NRF2 is a key regulator of cellular antioxidant response and often found over expressed in many different types of cancers. *Nrf2* mRNA level and NRF2 protein expression were both upregulated in the *Trim24*<sup>COE</sup> spheroids and knocking down TRIM24 significantly decreased *Nrf2* expression as well as NRF2-regulated gene expression. Metabolic inhibitors that target enzymes in one-carbon metabolism and *de novo* glutathione synthesis effectively decreased *Trim24*<sup>COE</sup> spheroids viability. The effect of PHGDH inhibitor CBR5884, GLS inhibitors CB839, and GCLC inhibitor was enhanced with TRIM24 knock-down, indicating that TRIM24 plays a critical role in oxidation-reduction (REDOX)-related cell survival.

Here, with metabolomic studies, we uncovered the potential metabolic vulnerabilities in *Trim24*<sup>COE</sup> MpBC spheroids. TRIM24 over expression led to upregulated production of reducing equivalents which further reduce oxidative stress and increase antioxidant defense in *Trim24*<sup>COE</sup> spheroids. Targeting TRIM24 and the corresponding metabolic enzymes in combination could shed light on potential strategies for inhibiting tumor progression of TRIM24-overexpressing MpBC. The work described here supports further investigations of these pathways in MpBC, for which no targeted therapies exist.

## Table of Contents

Approval Sheet.....	i
Title Page.....	ii
Dedication.....	iii
Acknowledgements.....	iv
Abstract.....	vi
Table of Contents.....	viii
List of Figures.....	ix
List of Tables.....	xiii
List of Abbreviations.....	xiii
Introduction.....	1
Materials and Methods.....	6
Results.....	18
Discussion.....	68
Appendix .....	77
References.....	82
Vita.....	103

## List of Figures

### List of Figures

Figure 1: TRIM24 protein structure and domains.....	4
Figure 2: Generation of mammary spheroids culture. ....	7
Figure 3: Workflow of isotope tracing (LC/IC- HRMS).....	10
Figure 4: Generation of <i>Trim24</i> <sup>COE</sup> mouse line. ....	19
Figure 5: Overexpression of TRIM24 in <i>Trim24</i> <sup>COE</sup> spheroids confirmed by western blot .....	20
Figure 6: Overexpression of TRIM24 in <i>Trim24</i> <sup>COE</sup> spheroids confirmed by IF staining....	21
Figure 7: Morphology of <i>Trim24</i> <sup>COE</sup> spheroids. ....	23
Figure 8: Knock- down of TRIM24 in shTrim24-64 and shTrim24-897 spheroids confirmed by western blots and IF staining. ....	24
Figure 9: Quantification of spheroid diameters showed TRIM24-dependent spheroid size.....	26
Figure 10: Quantification of spheroid invasion percentage showed TRIM24-dependent invasiveness. ....	26
Figure 11: Western blots of EMT markers in <i>Trim24</i> <sup>COE</sup> spheroids.....	28
Figure 12: Different EMT transcription factor mRNA expression across <i>Trim24</i> <sup>COE</sup> spheroid lines.....	29
Figure 13: Western blots of c-MYC and their quantification showed TRIM24-dependnet c-MYC at protein level. ....	30
Figure 14: Western blots and their quantification showed different BCSCs marker levels in <i>Trim24</i> <sup>COE</sup> , shCT-897 and shTrim24-897 spheroids.....	31
Figure 15: IF staining of K8 (luminal epithelial cell) and K14 (basal epithelial cell) in <i>Trim24</i> <sup>COE</sup> spheroids.....	32
Figure 16: IF staining of K8 (luminal epithelial cell) and K14 (basal epithelial cell) in shCT-897 and shTrim24-897 spheroids. ....	33

Figure 17: Western blot of K8 (luminal epithelial cell) and K14 (basal epithelial cell) in shCT-897 and shTrim24-897 spheroids.....	34
Figure 18: RNA sequencing data revealed heterogeneity in <i>Trim24</i> <sup>COE</sup> spheroids.....	35
Figure 19: CellROX staining showed low intracellular ROS in <i>Trim24</i> <sup>COE</sup> spheroids compared to the MMTV <sup>Cre-823</sup> control.....	36
Figure 20: Low intracellular ROS levels in spheroids were dependent upon TRIM24 overexpression.....	37
Figure 21: Intracellular ROS increased in MMTV <sup>Cre-823</sup> spheroids after 24 hours of H <sub>2</sub> O <sub>2</sub> treatment but not in <i>Trim24</i> <sup>COE</sup> spheroids.....	38
Figure 22: Intracellular ROS increased in shTrim24-897 spheroids after 24 hours of H <sub>2</sub> O <sub>2</sub> treatment but not in shCT spheroids. ....	39
Figure 23: MitoSOX staining of mitochondrial ROS after 24 hours of H <sub>2</sub> O <sub>2</sub> treatment did not change in MMTV <sup>Cre-823</sup> or <i>Trim24</i> <sup>COE</sup> spheroids.....	41
Figure 24: <i>Trim24</i> <sup>COE</sup> spheroid showed decreased overall response to Seahorse Mito Stress Test and TRIM24 knock down further decreased the responses.....	42
Figure 25: Total NADP(H) and reduced NADPH levels were upregulated in <i>Trim24</i> <sup>COE</sup> spheroids while decreased upon TRIM24 knock down. ....	43
Figure 26: <sup>13</sup> C <sub>6</sub> -glucose isotope tracing revealed increased glycolysis diversion to PPP shunt and 1C metabolism in <i>Trim24</i> <sup>COE-897</sup> spheroids.....	44
Figure 27: Western blots of PPP and 1C metabolism pathway showed increased enzyme levels in <i>Trim24</i> <sup>COE</sup> spheroids TRIM24-dependent enzyme levels in 1C metabolism.....	45
Figure 28: CTG viability assays showed PHGDH inhibitor CBR5884 decreased <i>Trim24</i> <sup>COE</sup> spheroid viability; the decrease in viability was enhanced upon TIRM24 knock down.....	47
Figure 29: Total NADP(H) and reduced NADPH assays revealed decreased reduced-NADPH level in <i>Trim24</i> <sup>COE</sup> spheroids after treated with CBR5884.....	47

Figure 30: 3PG supplement rescued <i>Trim24</i> <sup>COE</sup> spheroids viability but failed to rescue up TRIM24 knock down.....	48
Figure 31: <sup>15</sup> C <sub>5</sub> -glutamine tracing of <i>Trim24</i> <sup>COE</sup> spheroids and GSH/GSSG ratio assay revealed increased reduced glutathione level in <i>Trim24</i> <sup>COE</sup> spheroids.....	49
Figure 32: Western blot quantification of enzyme levels showed increased glutaminolysis pathway and <i>de novo</i> GSH synthesis pathway in <i>Trim24</i> <sup>COE-897</sup> spheroids.....	50
Figure 33: Western blot quantification showed downregulated enzymes in glutamate metabolism pathway and <i>de novo</i> GSH synthesis pathway in shTrim24-897 spheroids...	51
Figure 34: GLS inhibitor CB839 inhibits the conversion of glutamine to glutamate.....	53
Figure 35: CB839 treatment for 48 hours increased intracellular and mitochondrial ROS levels in <i>Trim24</i> <sup>COE</sup> spheroids. ....	54
Figure 36: Viability of <i>Trim24</i> <sup>COE</sup> spheroids was decreased after 48-hours CB839 treatment; the drug effect was enhanced by TRIM24 knock down.....	55
Figure 37: Total NADP(H) and NADP <sup>+</sup> /NADPH ratio assay of <i>Trim24</i> <sup>COE</sup> spheroids, showed increased NADP <sup>+</sup> abundance after CB839 treatment.....	56
Figure 38: CTG viability assay showed BSO treatment had additive effect with TRIM24 knock down. ....	57
Figure 39: Total NADP(H) levels were increased in <i>Trim24</i> <sup>COE-567</sup> and <i>Trim24</i> <sup>COE-64</sup> spheroids but not <i>Trim24</i> <sup>COE-897</sup> spheroids.....	58
Figure 40: CTG viability assay showed different responses to combined GSH synthesis inhibitor treatment in <i>Trim24</i> <sup>COE</sup> spheroids, shCT-897 and shTrim24-897.....	59
Figure 41: CTG viability assay showed resistance to H <sub>2</sub> O <sub>2</sub> was TRIM24 dependent.....	61
Figure 42: Usage of reduced NADPH in response to H <sub>2</sub> O <sub>2</sub> treatment was impaired by TRIM24 knock down.....	62
Figure 43: Nrf2 and its target genes mRNA expression in <i>Trim24</i> <sup>COE</sup> spheroids was induced by 24-hour 1mM H <sub>2</sub> O <sub>2</sub> treatment.....	64



Figure 44: Nrf2 and its target gene mRNA expression was decreased upon Trim24 knock down but induced after 24-hour 1mM H <sub>2</sub> O <sub>2</sub> treatment in shTrim24-897.....	65
Figure 45: Western blots and their quantification of NRF2 showed TRIM24-dependent NRF2 protein level.....	66
Figure 46: Western blot quantification showed NRF2 downstream pathway enzyme levels were increased in <i>Trim24</i> <sup>COE</sup> spheroids after 24-hour 1mM H <sub>2</sub> O <sub>2</sub> .....	67
Figure 47: Western blot quantification showed NRF2 downstream pathway enzyme levels were downregulated in shTrim24-897 spheroids compared to shCT-897 after 24-hour 1mM H <sub>2</sub> O <sub>2</sub> .....	68

## List of Tables

Table 1: Summary of rewired glycolysis and 1C-metabolism in <i>Trim24</i> <sup>COE</sup> spheroids and shCT/shTrim24-897 spheroids .....	74
--	----

Table 2: Summary of rewired GSH synthesis pathway in <i>Trim24</i> <sup>COE</sup> spheroids and shCT/shTrim24-897 spheroids .....	74
---	----

Table 2: Summary of NRF2-regulated response under oxidative stress in <i>Trim24</i> <sup>COE</sup> spheroids and shCT/shTrim24-897 spheroids.....	75
---	----

## Appendix

List of antibodies.....	71
List of primers.....	73
List of drugs and reagents.....	75

## List of Abbreviations

3PG/2PG	3-phosphoglycerate/3-phosphoglycerate
AKT	Protein kinase-B
ASCT	Alanine-serine-cysteine transporter
ASNS	Asparagine synthase
ARE	Antioxidant response element
ATP	Adenosine triphosphate
BCA	Bicinchoninic acid assay
BSCs	Breast cancer stem cells
BSO	Buthionine sulfoximine
Bromo	Bromodomain
cDNA	Complementary deoxyribonucleic acid
COE	Conditionally overexpressed
CTG	CellTitor-Glo <sup>®</sup> viability assay
CTF	CellTitor-Flour <sup>™</sup> viability assay
CUL	Cullin
DMSO	Dimethyl sulfoxide
DNA	Deoxyribonucleic acid
DMEM	Dulbecco's Modified Eagle Medium
ECAR	Extracellular Acidification Rate
EDTA	Ethylenediaminetetraacetic acid
EMT	Epithelial-mesenchymal transition
ER	Estrogen receptor
ERK	Extracellular signal regulated protein
FBS	Fetal bovine serum
FCCP	Carbonyl cyanide 4-(trifluoromethoxy)phenylhydrazone

G6PD	Glucose-6-phosphate dehydrogenase
GCL	Glutamate-cysteine ligase
GluD	Glutamate dehydrogenase
GluL	Glutamine synthase
GLS	Glutaminase
GPX	glutathione peroxidase
GSH	Reduced glutathione
GSS	glutathione synthase
GSSG	Oxidized glutathione
GSR	Glutathione reductase
GST	Glutathione transferase
KLF4	Kruppel-like factor 4
HER2	Epidermal growth factor receptor 2
HRMS	High-resolution mass spectrometry
H <sub>2</sub> O <sub>2</sub>	Hydrogen peroxide
IF	Immunofluorescence
iHMECs	Isogenic human mammary epithelial cells
K8/K14	Cytokeratin 8/ Cytokeratin 14
KEAP	Kelch-like associated protein
LC/MS	Liquid chromatography/mass spectrometry
MAPK	Mitogen-activated protein kinase
MDACC	M.D. Anderson Cancer Center
MpBC	Metaplastic breast cancer
mRNA	Messenger ribonucleic acid
mtDNA	Mitochondrial deoxyribonucleic acid
MTHFD	Methylenetetrahydrofolate dehydrogenase
mTOR	Mammalian target of rapamycin

NADPH	Nicotinamide adenine dinucleotide
NOX	Nicotinamide adenine dinucleotide oxidase
NRF2	Erythroid2-related factor
$O_2^-$	Superoxide anion
$\cdot OH$	Hydroxyl radical
OCR	Oxygen consumption rate
OXPHOS	Mitochondrial respiration or oxidative phosphorylation
p53	Tumor protein p53
P5CDH	Delta-1-pyrroline-5-carboxylate dehydrogenase
PGD	6-phosphogluconate dehydrogenase
PHGDH	Phosphoglycerate dehydrogenase
PFA	Paraformaldehyde
PGK	Phosphoglycerate kinase
PHD	Plant homeodomain
PI3K	Phosphoinositide 3-kinase
PPP	Pentose phosphate pathway
PR	Progesterone receptor
PRODH	Proline dehydrogenase
PSAT	Phosphoserine aminotransferase
PYCR	Pyrroline-5-Carboxylate Reductase 1
Redox	Reduction-oxidation
TALDO	Transaldolase
TCA	Tricarboxylic acid cycle
TNBC	Triple negative breast cancer
Trim	Tripartite motif containing family of proteins
TWIST	Twist Basic Helix-Loop-Helix Transcription Factor
qRT-PCR	Quantitative Real-time polymerase chain reaction

ROS	Reactive oxygen species
RNA	Ribonucleic acid
SHMT	Serine hydroxymethyltransferase
shRNA	Short hairpin ribonucleic acid
SMA	Smooth muscle actin
SNAI	Snail Family transcriptional repressor
SOX	SRY-Box transcription factor
siRNA	Small interfering ribonucleic acid
ZEB	Zinc Finger E-Box Binding Homeobox 1

## Introduction

One hundred and one years ago in 1920, pioneering biochemistry researcher Otto Warburg discovered aerobic glycolysis in tumor tissues cultured in vitro. This finding revolutionized the field by linking cancer biology to metabolism [1, 2]. His observation became known as the Warburg Effect, which describes the high rate of glucose uptake, glycolysis and lactate secretion exhibited by cancer cells under non-hypoxic conditions, even with a high concentration of oxygen [3]. The Warburg effect was once considered a hallmark of aggressive cancer cells, but later was found in highly proliferative non-transformed cells [4]. Historically, aerobic glycolysis was thought to be a consequence of impaired mitochondrial respiration [5] as hyperactive glycolysis eliminates carbon sources from the TCA cycle. However, in the past decades, the origin of aerobic glycolysis has been questioned as more studies reveal that mitochondria in cancer cells are still functional with relatively lower activity [6].

Increased glucose uptake and glycolysis allow cancer cells to feed macromolecular synthesis pathways, other than the mitochondrial citric acid cycle (TCA cycle). These pathways include pentose-phosphate pathway (PPP) that produces ribose ring for DNA/RNA synthesis and reducing agent NADPH; serine-glycine-one-carbon-metabolism (1C metabolism) that produces folate, NADPH, and glutathione synthesis substrate; and the hexosamine pathway that produces metabolites for protein glycosylation [2]. Nicotinamide adenine dinucleotide phosphate (NADPH) is a major reducing equivalent in antioxidant systems such as glutathione (GSH) and catalase, and it plays a critical role in the maintenance of enzyme-catalyzed reduction-oxidation (Redox) balance in the cells [7].

Redox is a principle biochemical reaction in all living cells by which oxidative atoms are exchanged. Oxygen ( $O_2$ ) is an essential molecule for mammalian cells to produce adenosine triphosphate (ATP) through mitochondrial respiration also known as oxidative phosphorylation (OXPHOS).  $O_2$  is a relatively unreactive molecule, however, incomplete

reduction of  $O_2$  will lead to the formation of reactive oxygen species (ROS). ROS is a collective term for hydrogen peroxide ( $H_2O_2$ ), hydroxyl radical ( $\cdot OH$ ) and superoxide anion ( $O_2^-$ ) [8]. They are mainly produced by the mitochondrial electron transport chain (ETC) during oxidative respiration, peroxisomes through fatty acid  $\beta$ -oxidation, and endoplasmic reticulum through oxidation of proteins [9]. ROS are chemically highly reactive and they can cause structural or functional damage to proteins and lipids, as well as DNA strand breaks to potentially induce genomic instability [10].

ROS had been thought to be a deleterious metabolite until the 1990s. Studies of the past decades set the stage for the role of ROS in cellular signaling cascades and driving tumorigenesis [11]. Low doses of ROS (around  $1\ \mu M$ ) are capable of stimulating cellular adaptation and proliferation; however, as ROS level increases, cell death signaling pathways such as apoptosis or ferroptosis are initiated [12]. ROS are both initiators and promoters of cancer. During the transformation process, activation of oncogenes, loss of tumor suppressor genes, and mutations in mitochondrial DNA (mtDNA) lead to a surge in ROS level in cells [13]. This allows activation of phosphoinositide 3-kinase/protein kinase-B/mammalian target of rapamycin pathways (PI3K/AKT/mTOR), mitogen-activated protein kinase/extracellular signal regulated kinase (MAPK/ERK) and nuclear factor  $\kappa B$  (NF $\kappa B$ ) pathways [11, 12, 14]. Continuously increased ROS further can induce more mutations in cancer cells and promote tumor growth, resistance to chemotherapy and metastasis [8].

According to the Global Cancer Observatory(GCO), breast cancer (BC) had the highest incidence worldwide in 2020, with approximately 2.2 million diagnosed cases [15]. It is the most common malignancy and also the top cause of cancer-related deaths among women [16]. BC is a highly heterogeneous disease and is characterized into three major subtypes in the clinic: estrogen and/or progesterone receptor (ER/PR)-positive, epidermal growth factor receptor 2 (ERBB2/ HER2)-positive, as well as triple-negative breast cancer (TNBC) which lack of ER, PR and HER2 [17]. At a molecular level, BC is divided into four



subtypes based on the gene expression signatures. In order of better clinical prognosis to worse prognosis, they are luminal A (ER-positive and/or PR-positive, HER2-negative), luminal B (ER-positive and/or PR-positive, HER2-positive), HER2-enriched (ER-negative and PR-negative, HER2-positive) and basal-like (ER-negative, PR-negative, and HER2-negative) breast tumors [18]. The presence of these hormone receptors ER, PR, and HER2 determines therapeutic strategies.

Without hormone receptors as molecular targets, TNBC patients have poorer clinical outcomes compared to other subtypes [19]. TNBC is associated with high tumor histologic grade, heterogeneity, aggressive phenotype and high metastatic rate [19-21]. Although standard treatment chemotherapy like epirubicin and capecitabine [22] provides some benefit for the TNBC patient, the high rate of recurrence and resistance to chemotherapy are still major problems [19]. Metabolic reprogramming is an emerging hallmark of cancer cells, which may offer potential vulnerabilities that may lead to new therapeutic approaches [12]. Major metabolic pathways, primarily glucose, glutamine, serine and fatty acid metabolism are rewired to support anabolism, catabolism and redox regulation in TNBC [23, 24]. Alterations of these metabolic pathways may reflect their regulation by upstream signaling pathways, such as RTK/KRAS, PI3K/AKT/mTOR, p53 and c-Myc which are commonly aberrant in TNBC [25].

Metaplastic breast cancer (MpBC) is a rare and less studied TNBC subtype, representing 0.2%-5% of all breast cancers [26]. It is identified by the presence of both epithelial features (carcinoma) and mesenchymal/stromal cell characteristics (sarcoma) [27]. With dismal clinical outcomes even worse than other subtypes of TNBC, MpBC is very aggressive and highly metastatic. These characteristics are attributed to highly expressed epithelial-to-mesenchymal transition (EMT) signature genes and tumor stem cell marker gene expression [26]. Previous work from our lab revealed that, TRIM24 was overexpressed in MpBC patients and high TRIM24 levels also correlated with poor prognosis and overall survival of patients [28]. TRIM24 is over expressed in multiple

cancers [29]. It has a RING-domain E3 ligase for p53 degradation, binds and ubiquitinates p53 and keeps p53 level low at steady state. TRIM24 and p53 interaction forms an autoregulatory loop: when DNA damage accumulates in the cells, degradation of p53 by TRIM24 is inhibited which leads to increased p53 level and also results in increased TRIM24 transcription. Higher TRIM24 level again degrade p53 through ubiquitylation and negatively regulates p53 level in the cells [30]. In contrast, TRIM24 depletion in human breast cancer cells induces spontaneous apoptosis in a p53-dependent manner [31]. TRIM24 also has a LXXLL domain for binding nuclear receptor ER; and plant homeodomain (PHD)/bromodomain (Bromo) histone reader of unmodified H3K4(H3K4me0) as well as acetylated H3K23 (H3K23ac) [28, 30, 31] (Figure 1). Studies from our lab showed that aberrant expression of TRIM24 in isogenic human mammary epithelial cells (iHMECs) induces malignant transformation and promotes glycolytic and tricarboxylic acid (TCA) gene upregulation [32]. However, it remains unclear how TRIM24 over expression reprograms metabolic pathways that contribute to survival and proliferation of TRIM24-over expressing breast cancer cells.

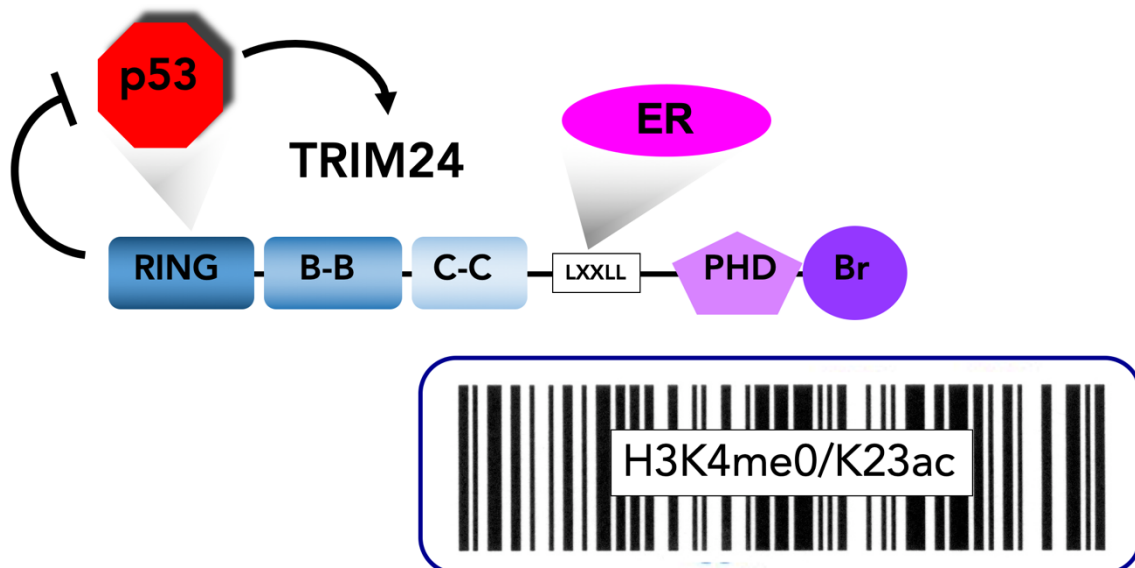


**Figure 1: TRIM24 protein structure and domains.**

TRIM24, 116KD, is a multi-domain protein. The RING domain ubiquitinates and degrades phosphorylated p53; the B-boxes (B-B) are zinc finger domains; the coiled-coil

domain (C-C) is required for hetero-oligomerization with other TRIM family proteins; The LXXLL motif interacts with nuclear hormone receptors; PHD and Bromo domains are histone readers which recognize demethylated H3K4 and acetylated H3K23. Overall, TRIM24 recruit ER to chromatin and activate ER-targeted gene expression in breast cells.

TRIM24 over expression plays a causal role in cancer cell proliferation, tumor initiation and progression [28, 32]. To further study the mechanism and consequences of TRIM24 over expression, our lab generated a mouse model that conditionally overexpresses (COE) TRIM24 protein in mouse mammary epithelia (*Trim24<sup>COE</sup>*), which resulted in development of carcinosarcoma or metaplastic mammary tumors. Global gene expression analysis revealed that *Trim24<sup>COE</sup>* mammary tumors exhibit highly activated glycolysis, EMT, and cMET-PI3K-mTOR pathways [33]. Glycolysis, as the most upregulated pathway in *Trim24<sup>COE</sup>* tumors, reflects a typical Warburg effect that also fuels multiple metabolic branches, such as PPP and 1C metabolism for NADPH production. As an essential reducing equivalent, NADPH levels are closely associated with redox balance in cells. Thus, I hypothesized that TRIM24 promotes breast cancer progression through rewiring redox regulation. To test this hypothesis, we performed metabolomic studies using three-dimensional mammary spheroids derived from mouse mammary MpBC cells, with the goal of understanding redox regulation in MpBC tumor model cells to reveal potential metabolic vulnerabilities.

## Methods

### Embedded spheroid culture

Metaplastic breast cancer primary cell lines were generated from mouse metaplastic breast tumors as our recently published paper described [33]. Adherent cells were trypsinized (0.05% Trypsin, Gibco, 25300120) and resuspended with breast cancer spheroids medium. The spheroid culture medium consists of DMEM/F12 (Gibco 11330-032), 10% FBS (Gemini Bioproducts, 100-106), 100 U/mL Penicillin/Streptomycin (Gibco, 15140122), 1x B27 supplement (Gibco, 17504044), 5 µg/mL Insulin (Sigma I-5500), 1 µg/mL Hydrocortisone (Sigma, H0888), and 10 ng/mL EGF (ThermoFisher, PHG0310). Matrigel Matrix for organoid culture (Corning, 356255) was thawed at 4°C and kept on ice. Tissue culture-treated 24-well plates (Corning, 3524) needed to be coated with Matrigel to prevent monolayer formation, the coated plates were then placed in 37°C and 5% CO<sub>2</sub> incubator for the Matrigel to solidify. The plating procedure was modified from the previously published protocol [34] (Figure 2). Approximately 2500 cells were mixed in 50 µL Matrigel and plated on top of the Matrigel coating with cold pipette tips. The plate was put back to the 37°C and 5% CO<sub>2</sub> incubator for 15 minutes. Once the Matrigel dome solidifies, 1 mL spheroid culture medium was added to each well and the medium was changed every 3 to 4 days.

To retrieve the spheroids for subsequent functional studies, the spheroids culture medium was removed and the Matrigel domes that contained embedded spheroids were gently washed with room temperature PBS (Hyclone, SH30256.01). 500 µL cold Cell Recovery Solution (Corning, 354253) was added to each well and kept on ice for 15 to 20 minutes to dissolve the Matrigel. The spheroids were collected in 1.5 mL tubes from each well and centrifuge at 4°C and 500 rpm for 5min. Cell pellets were washed with cold PBS three times and the pellets can be stored at -80°C.

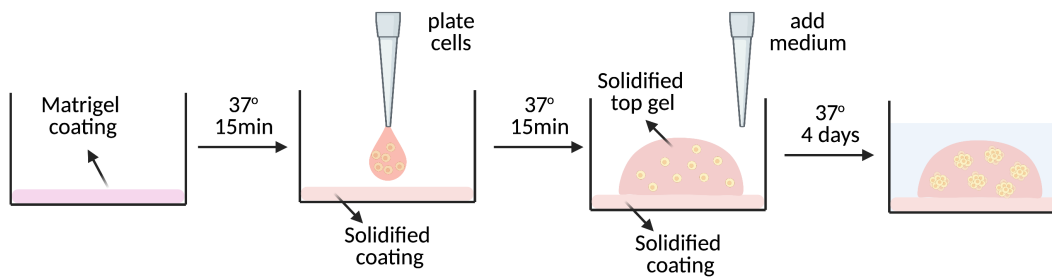


**Figure 2: Generation of mammary spheroids culture.**

(Figure made in BioRender.com)

### Immunofluorescence staining

Whole-culture immunofluorescence staining was performed as previously described [34, 35]. 8-chamber cover glass slide (Lab-Tek II, 155409) was coated with pre-thawed 10  $\mu$ L Matrigel (Corning, 356255) per chamber. The coated slide was placed at room temperature for 15 minutes. After the coating gel was solidified, mixed approximately 2000 cells with 50  $\mu$ L Matrigel and plated it on top of the coating. The slide was put into the 37°C and 5% CO<sub>2</sub> incubator for 15 minutes, then 500  $\mu$ L complete spheroid culture medium was added to each well. On day 4 of culturing, the spheroids were fixed with 200  $\mu$ L/well 4% paraformaldehyde (Sigma, P6148) at room temperature for 10 to 15 minutes. Each well was then washed with PBS (Hyclone, SH30256.01) twice. 0.5% Triton X-100 (Fisher Bioreagents, BP151-500) was used to permeabilize the samples, by adding 200  $\mu$ L/well to each well at room temperature for 30 minutes. After removing the 0.5% Triton X, the samples were immediately blocked with 10% FBS for 2 to 3 hours at room temperature. Primary antibodies (Appendix 1) were diluted to the 1:200 with 10% FBS and incubated with the sample at 4°C overnight. After removing the primary antibodies, the samples were washed with 10% FBS three times, 10 minutes each time at room temperature. Secondary antibody Alexa Fluor 647 Goat anti-mouse IgG (Invitrogen, A21236) or Alexa Fluor 488 goat anti-rabbit IgG (Invitrogen, A11034) were diluted to 1:500 with 10% FBS. The samples were incubated with the secondary antibodies for 1 to 2 hours

at room temperature. After the removal of secondary antibodies, the samples were washed with PBS for three times at room temperature, 10 minutes each time. Finally, the samples were stained with 1:500 DAPI, diluted with PBS, for 20 minutes at room temperature, followed by three 10 minutes wash with PBS. Olympus Fluoview 1000 confocal microscopy was used to take the z-stacked images of the spheroids. Z-stacked images were assembled and with Fiji, as well as the 3D reconstruction.

### **Invasion analysis**

About 3000 cells were plated in 24-well plates (Corning, 3524) coated with Matrigel, following the procedure described above. On day 4, brightfield images of ten randomly selected areas were taken from each well. With Celigo Image Cytometer (Nexcelom Biosciences), invasion area could be scanned and quantified. With an image processing software Fiji, fifteen spheroids were randomly selected and the number of invasive/non-invasive spheroids were counted by hand and the invasion percentage was calculated ( $\text{invasion \%} = \# \text{ of invasive spheroids} / \# \text{ of total spheroids}$ ). Ten image fields were quantified from each cell lines and an average invasion percentage was calculated.

### **Cellular ROS and mitochondrial ROS staining**

Reactive oxygen species (ROS) level was measured with CellROX<sup>®</sup> Orange (Life Technologies, C10443), CellROX<sup>®</sup> Deep Red Reagents (Life Technologies, C10422), and MitoSOX<sup>™</sup> (Molecular Probes, M36008) following the manufacturer's protocol. Spheroids were stained with 1:500 CellROX or 1:1000 MitoSOX reagent in an 8-chamber cover glass slide (Lab-Tek II, 155409), with DAPI (1:300 dilution) as a counterstain. The spheroids were incubated with the ROS stain in 37°C and 5% CO<sub>2</sub> incubator for 1 hour. PBS was used to wash the slides three times. Fluorescent signals were detected with Olympus Fluoview 1000 confocal microscopy, and Fiji was used to quantify the signal intensity.

## **Cell viability assay**

Spheroid viability was assessed using CellTiter-Glo<sup>®</sup> Luminescent Cell Viability Assay (CTG) (Promega, G7570) and CellTiter-Fluor<sup>™</sup> Cell Viability Assay (CTF) (Promega, G6080), following the manufacturer's protocols. After adding the reagent directly to the spheroid culture, the samples were put on a horizontal rocker for 15 minutes at room temperature and protected from light. Luminescent (CTG) or fluorescence (CTF) indicating cell viability was measured with FLUOstar Omega plate reader.

## **LC/IC- HRMS analysis of polar metabolites**

To assess the incorporation of carbon from glucose or glutamine into glycolysis pathway, Pentose Phosphate Pathway (PPP) and intracellular tricarboxylic acid (TCA) cycle, metabolites extracts from cell lysate were prepared and analyzed by high-resolution mass spectrometry (HRMS). Spheroids embedded in Matrigel were harvested on Day 4 of culturing from 10 cm dishes (about thirty 50  $\mu$ L Matrigel domes per plate) in triplicate. Cells were washed with glucose-free or glutamine-free medium then cells were incubated in fresh complete medium containing 11.1 mM  $^{13}\text{C}_6$ -Glucose for 6 hours; or 2 mM  $^{13}\text{C}_5$ -Glutamine for 24 hours. Spheroid-containing Matrigel domes were washed with cold PBS and 5 mL Cell Recovery solution (Corning, 354253) was added to reach plate, following by 15 minutes incubation at 4°C. After the Matrigel dissolved, spheroids were transferred to 15 mL tubes and pellets were washed with PBS twice (Figure 2). Metabolites were extracted with cold 80% methanol with 0.1% ammonium hydroxide. Cell lysates were centrifuged at 17,000 g for 5 min at 4°C. The supernatants were then transferred to clean tubes, followed by evaporation under nitrogen until the samples were complete dry. Dried samples were then reconstituted with deionized water, then 5  $\mu$ L was injected into a Thermo Scientific Dionex ICS-5000+ capillary ion chromatography (IC) system that contains a Thermo IonPac AS11 250 $\times$ 2 mm 4  $\mu$ m column (ThermoFisher, 078035) for

glycolysis and TCA cycle metabolites analysis. IC flow rate was 360  $\mu\text{L}/\text{min}$  at  $30^\circ\text{C}$  and the gradient conditions were as follows: started with 1 mM KOH, increased to 35 mM at 25 minutes, then to 99 mM at 39 minutes, held at 99 mM for 10 minutes. The total duration of the experiment took 50 minutes. Methanol was administered by an external pump and combined with the eluent via a low dead volume mixing tee, in order to assist the desolation for better sensitivity. Metabolite data was acquired with a Thermo Orbitrap Fusion Tribrid Mass Spectrometer under ESI negative mode.

To analyze amino acids, samples were diluted in 90% acetonitrile containing 1% formic acid, then 15  $\mu\text{L}$  sample was injected into a Thermo Vanquish liquid chromatography (LC) system containing an Intrada Amino Acid 2.1 x 150 mm column (Imtakt, WAA25) with 3  $\mu\text{m}$  particle size. Mobile phase A (MPA) was acetonitrile with 0.1% formic acid and mobile phase B (MPB) was 50 mM ammonium formate. The flow rate was set to 300  $\mu\text{L}/\text{min}$  at  $35^\circ\text{C}$ , and the gradient conditions were: 15% MPB in the beginning, increased to 30% MPB at 20 min, then increased to 95% MPB at 30 min, held at 95% MPB for 10 minutes, returned to initial conditions followed by equilibration for 10 minutes. The total run time took 50 minutes and the data was acquired by Thermo Orbitrap Fusion Tribrid mass spectrometer under ESI positive ionization mode, at a resolution of 240,000. Then the raw data was imported to Thermo Trace Finder software for further analysis. The fractional abundance of each isotopologue was determined by the peak area of the corresponding isotopology normalized by the sum of all isotopology areas.

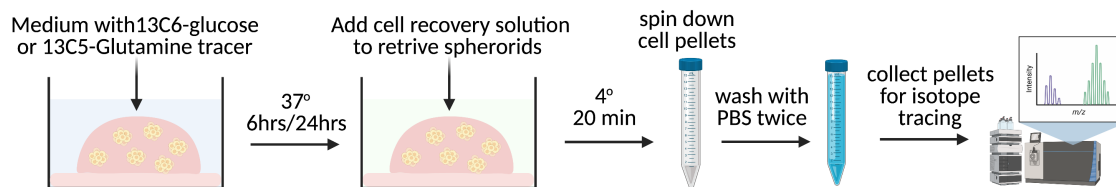


**Figure 3: Workflow of isotope tracing (LC/IC- HRMS).**

(Figure made in BioRender.com)



## **Protein extraction and Western Blotting**

Spheroids embedded in Matrigel were collected following the protocol described above. 150  $\mu$ L or 200  $\mu$ L 1% SDS was added to the cell pellets, depended on the size of the cell pellets. The protein lysate was homogenized by sonification at 40% power for 5 seconds, repeated three times. The debris was removed through centrifugation at 14000 rpm for 15 minutes at 4°C. Protein concentration was estimated by Pierce™ BCA Protein Assay Kit (ThermoFisher, 23227) and diluted to the desired concentration with 1% SDS. 5x SDS loading dye was added to the normalized lysate then separated by electrophoresis on a 1.5mm 10% SDS-PAGE gel. Resolved proteins were transferred to nitrocellulose membrane through Trans-blot®Turbo™ Transfer System (BioRad, 1704150) as the manufacturer instructed. The membranes were stained with Ponceau S solution (Fisher Scientific, NC9099742) to confirm the transfer of protein bands. 3% milk was made by adding 3g of milk powder to 100 mL 1X TBST and it was used to block the membrane at room temperature, rocking for 1 hour. Primary antibodies (Table S2) was diluted according to the manufacturer's recommendation with 3% milk and incubated with the membrane at 4°C, rocking overnight. The membranes were then washed with 1X TBST for 10 minutes, repeated 3 times, followed by secondary antibodies (Goat anti-Mouse, Invitrogen 35518; Goat anti-Rabbit, Invitrogen SA5-10036) incubation at room temperature for 1 hour. After three washes with 1X TBST for 10 minutes and two washes with 1X TBS, the membranes were imaged with the ChemiDoc™ Imaging System (BioRad, 12003153)

## **RNA Extraction, reverse transcription and RT-qPCR**

To collect spheroids embedded in Matrigel, the desired amount of cold Cell Recovery Solution (Corning, 354253) was used following the procedure described above. 300  $\mu$ L Trizol was added to the spheroid pellets and stored in -80°C. To extract RNA, 300  $\mu$ L 100% ethanol was added to the lysate and mixed well. Zymo-Spin IICR Column (Zymo Research,

C1078) was used to collect the RNA referring to the manufacturer's instruction. The samples were transferred to the spin column, and the flow-through was discarded. 400  $\mu$ L of RNA Wash Buffer (Zymo Research, R1003) was added to the column followed by centrifugation. 80  $\mu$ L of DNase I treatment was prepared from 5  $\mu$ L DNase I (Zymo, E1010), and 75  $\mu$ L DNA Digestion Buffer (Zymo, E1010) and then the mixture was added to the spin columns followed by room temperature incubation for 15-minutes. After centrifugation, 400  $\mu$ L of Direct-zol RNA PreWash (Zymo Research, R2050) was added to the spin columns and centrifuged. Flow-through was discarded and the washing step was repeated. 700  $\mu$ L RNA Wash Buffer was then added to the spin column, centrifuged and the flow-through was discarded. To remove excess washing buffer, spin columns were transferred to new collection tubes and centrifuged for 2 minutes. The spin columns were transferred to new 1.5 mL Eppendorf tubes and 30  $\mu$ L of DNase/RNase-Free Water was added to the spin columns and incubated at room temperature for 5 minutes before centrifugation. The eluted RNA was then added back into the spin column and centrifuged again. The eluted RNA was then analyzed via Nanodrop for quality and concentration of RNA yield.

The cDNA was made using the iScript Reverse Transcription Supermix (BioRad, 1708841) as per the manufacturer's guidance. Thermocycler was used to carry out the reverse transcription with the setting of: 25°C for 5 minutes, 46°C for 20 minutes 96°C for 1 minute. The cDNA product was diluted to 1:20 with RNase-free water for real-time quantitative PCR. All RT-qPCR primers were designed with the primer picking tool Primer-BLAST and Mouse Genome Informatics Database Ensemble on the NCBI website (Table S3). Stock solutions of primers were diluted at a concentration of 100  $\mu$ M in RNase-free sterile water. Working primer dilutions were made of a 1:10 of the stock primer solution. Master mix for qPCR was made with 5  $\mu$ L Syber Green (BioRAD, 1725270), 0.05  $\mu$ L of the forward or reversed primer, 1.9  $\mu$ L RNase-free sterile water, and 3  $\mu$ L cDNA of each sample. RT-qPCR reactions were performed with the these conditions: 95°C holding for 5 minutes, 95°C for 30 seconds, 55°C to 60°C for 30 seconds which depends on primer sets'

annealing temperature, and 72°C elongations for 30 seconds, repeat to step 2 for 40 cycles. 18S ribosomal RNA was used as a housekeeping gene for normalization.

### **Oxygen Consumption Assays (Seahorse)**

Seahorse XFe96 Extracellular Flux Analyzer (Aligent Technologies) was used to quantify the cellular oxygen consumption rate (OCR). 2D cells were seeded at 10,000 cells per well in a 96-well cell culture plate (Agilent Technology, 102340-100) with 200 µL/per well DMEM (Corning, 10-017-cv) which supplemented with 10% FBS (Gemini Bioproducts, 100-106) and 100 U/mL Penicillin/Streptomycin (Gibco, 15140122). The culture plate was incubated in a 37°C and 5% CO<sub>2</sub> incubator overnight. The sensor cartridge was hydrated in the Seahorse XF calibrant in a 37°C and non-CO<sub>2</sub> incubator overnight (Aligent Technologies, 100804-000) following the manufacturer's guide. On the day of assay, 1 hour before the experiment, cells were washed with PBS and incubated in 180 µL/well serum-free Seahorse XF DMEM (Aligent Technologies, 103575-100) which was supplemented with 1 mM pyruvate (Aligent Technologies, 103578), 2 mM glutamine (Aligent Technologies, 103579-100) and 10 mM glucose (Aligent Technologies, 103577-100). The plate was placed in a 37°C and non-CO<sub>2</sub> incubator for 1 hour prior to the assay. Drug stock solutions from the XF Cell Mito Stress Test Kit (Aligent Technologies, 103016-100) were prepared as the user guide described (100 µM Oligomycin, 100 µM FCCP, 50 µM Rotenone and Antimycin A). The drug solutions were loaded in to the corresponding ports on the sensor cartridge, following the user guide, and the final concentration for each well was 1.5 µM Oligomycin, 1 µM FCCP and 0.5 µM Rotenone and Antimycin A. The OCR readings were determined and the OCR baseline reading before any drug treatment was define as basal respiration. After oligomycin administration, the absolute OCR reduction was defined as ATP-linked respiration. The absolute OCR reading after FCCP administration was defined as maximal respiration, and the increase above baseline after FCCP treatment was defined as spare capacity. The OCR reading after

Rotenone & Antimycin A administration was defined as non-mitochondrial oxygen consumption.

### **shRNA knockdown line generation**

For tet-inducible shRNA cell lines, we used a lentivirus system and Lipofectamine 3000 (ThermoFisher Scientific, L3000008) to transfect 293FT cells using manufacturer's recommendations on virus production. Both shControl (Horizon, RHS4743) and shTrim24 (Horizon, RMM4431-200368247) were purchased through the functional genomic core at University of Texas M.D. Anderson Cancer Center for cloning in a TRIPZ inducible lentivirus vector. Next, lentivirus was collected from 293FT cells to transduce the TRIM24-driven primary metaplastic carcinoma cell line 897. The shControl and shTRIM24-897 cells were grown under puromycin selection and sorted based on RFP after tetracycline induction (1 $\mu$ g/ml).

### **RNA Library preparation and Deep-Sequencing**

To perform deep sequencing of RNA (RNA-seq), total RNA was isolated from individual tumors, in parallel with freshly isolated, disease free mammary glands (controls), using Zymo Direct-zol RNA miniprep kit (R2050). RNA libraries were prepared using TrueSeq RNA Library Prep Kit v1 (Illumina) followed by sequencing at the MD Anderson Next Generation Sequencing Core Facility.

### **RNA-Sequencing Analysis**

Sequences were first checked for quality using FASTQC and then adapters were trimmed using Trimmomatic's default settings [36]. Trimmed reads were checked again with FastQC, and then aligned to the GRCm38 mouse genome assembly with the GENCODE Release M14 transcriptome using the STAR aligner [37]. The reads were counted with

HTSeq-Count [38] using the union mode to resolve multiple features. To determine the gene expression profile between Control and TRIM24 overexpressing spheroids, a differential expression analysis was performed to compare profiles of tumors with non-tumor control using DESeq2 [39]. Genes were selected using a false discovery rate cutoff of 5% and at least a fold change between groups. Hallmark pathways were calculated using GSEA [40].

### **Gallios flow cytometry CellRox quantification**

Spheroids embedded in Matrigel were collected according to the procedure described above. Adherent cells were washed with PBS and trypsinized. Cell pellets were spin down in the flow-cytometry tubes (Falcon, 352235). Cells were washed twice with 250 mM EDTA diluted with PBS and passed through the strainers of the flow-cytometry tubes. Gallios 561 Flow Cytometer was used to quantify the percentage of cells with certain staining as well as the signal intensities.

### **Total NADP(H) and NADP<sup>+</sup>/NADPH ratio Assays**

Spheroids embedded in Matrigel were collected according to the procedure described above. NADP<sup>+</sup> and NADPH level was measure by Total NADP and NADPH Assay Kit (Abcam, ab186033) and NADP/NADPH Assays kit (Abcam, ab65349) as the manufacturer instructed. In brief, NADPH standard or NADP/NADPH reaction mixture were reconstituted. NADPH standard solution was prepared with PBS to obtain 2  $\mu$ M, 1  $\mu$ M, 0.5  $\mu$ M, 0.25  $\mu$ M, 0.125  $\mu$ M, 0.0625  $\mu$ M, 0.0313  $\mu$ M and 0  $\mu$ M (blank control) serial dilutions of NADPH standard. 50  $\mu$ L/well cell lysate and NADPH standard dilutions were added into a clear bottom 96-well microplate. Then 50  $\mu$ L/well total NADP(H) or NADP/NADPH reaction mix was added into each well of NADPH standard and samples,

incubated at room temperature for 1 hour. The absorbance was monitored at 460 nm with the FLUOstar Omega plate reader.

### **NADPH Assays**

Spheroids embedded in Matrigel were collected according to the procedure described above. Reduced NADPH level was measure by colorimetric NADPH Assay Kit (Abcam, ab186031) as the manufacturer instructed. Frist, NADPH standard and NADPH reaction mixture were reconstituted. 100  $\mu$ L NADPH stock solution was mixed with 400  $\mu$ L PBS to obtain 200  $\mu$ M standard solution. Serial dilution was performed to obtain 100  $\mu$ M, 50  $\mu$ M, 25  $\mu$ M, 12.5  $\mu$ M, 6.25  $\mu$ M, 3.13  $\mu$ M and 0  $\mu$ M (blank control) reduced NADPH standards. 50  $\mu$ L/well cell lysate or NADPH standard dilutions were added into a clear bottom 96-well microplate. Then 50  $\mu$ L/well NADPH reaction mix was added into each well of NADPH standard or samples, incubated at room temperature for 15 minutes. The absorbance was monitored at 460 nm with the FLUOstar Omega plate reader. A standard curve was constructed based on the readings of NADPH standard solutions and NADPH concentration in each tested sample was calculated from the standard curve.

### **GSH/GSSG Ratio assays**

GSH/GSSG-Glo Assay (Promega, V6611) was used to measure reduced glutathione and oxidized glutathione as manufacturer instructed. 5 mM GSH was diluted to 320  $\mu$ M with water, 1:2 serial dilution was performed by adding 250  $\mu$ L water to 250  $\mu$ L GSH standards. The final GSH standard concentration for each well in a 96-well plate ranged from 16  $\mu$ M to 0  $\mu$ M (blank control). The tumorspheres in the 96-well plate was lysed with either 25  $\mu$ L total glutathione reagent (Luciferin-NT, 5X Passive Lysis Buffer, water) or oxidized glutathione reagent (Luciferin-NT, NEM, 5X Passive Lysis Buffer, water) and the plate was placed on a horizontal shaker at room temperature for 5 minutes. Luciferin Generation

reagent (DTT, Glutathione-S-Transferases, and Glutathione Reaction Buffer) was prepared according to the manufacturer's recommendation and 50  $\mu$ L was added to the samples as well as the GSH standard dilutions. After 30 minutes of incubation at room temperature, 100  $\mu$ L Luciferin Detection Reagent was added to each well. After another 15-minute incubation at room temperature, luciferin signals were detected with the FLUOstar Omega plate reader.

### **Statistical analysis**

Statistical tests were performed using paired or unpaired Student's *t* test, multiple t-test, one-way or two-way ANOVA by the PRISM 8 software. Values with *p* <0.05 were considered statistically significant.

## Results

The goal of this master thesis is to define how TRIM24 overexpression rewires reduction-oxidation metabolism to promote survival and proliferation of cells derived from a mouse model of metaplastic breast cancer. To study these aspects, all studies reported here were conducted *in vitro* with three-dimensional spheroids.

### TRIM24 drives EMT and stemness in mammary spheroids

To determine whether TRIM24 functions as an oncoprotein and drives tumorigenesis *in vivo*, our lab developed a mouse model that conditionally over expresses TRIM24 protein in mouse mammary epithelial cells to a level 2-3-fold greater than observed in normal, age-matched mammary gland epithelial cells [33].

A piggyBac transposon vector was constructed with a human UBC promoter, followed by loxP-lacZ-stop-loxP cassette, 5' of the mTrim24 cDNA and a FLAG tag (pBac-UbC-loxP-stop-loxP-Trim24-FLAG). After injection of the uncut construct along with transposase RNA to the zygote pronuclei, transgenic *Trim24* founder mice (*Trim24*<sup>LSL</sup>) were identified by genotyping. To drive tissue-specific expression of transgenic m*Trim24*, *Trim24*<sup>LSL</sup> mice were bred with MMTV-Cre recombinase mouse line (*MMTV-Cre*<sup>Tg/0</sup>) for Cre recombinase-mediated excision of the floxed  $\beta$ -Geo-stop codon. The resulting mice conditionally overexpressed *Trim24* in mammary epithelial cells, creating a mouse line named *Trim24*<sup>COE</sup> (Figure 4). In this model, *Trim24* over expression is sufficient for initiation and progression of mammary carcinosarcoma. In order to generate a control line for comparison to the *Trim24*<sup>COE</sup> line, MMTV-Cre virgin mice were aged in parallel, leading to a rare spontaneous mammary tumor that lacked TRIM24 over expression [33].



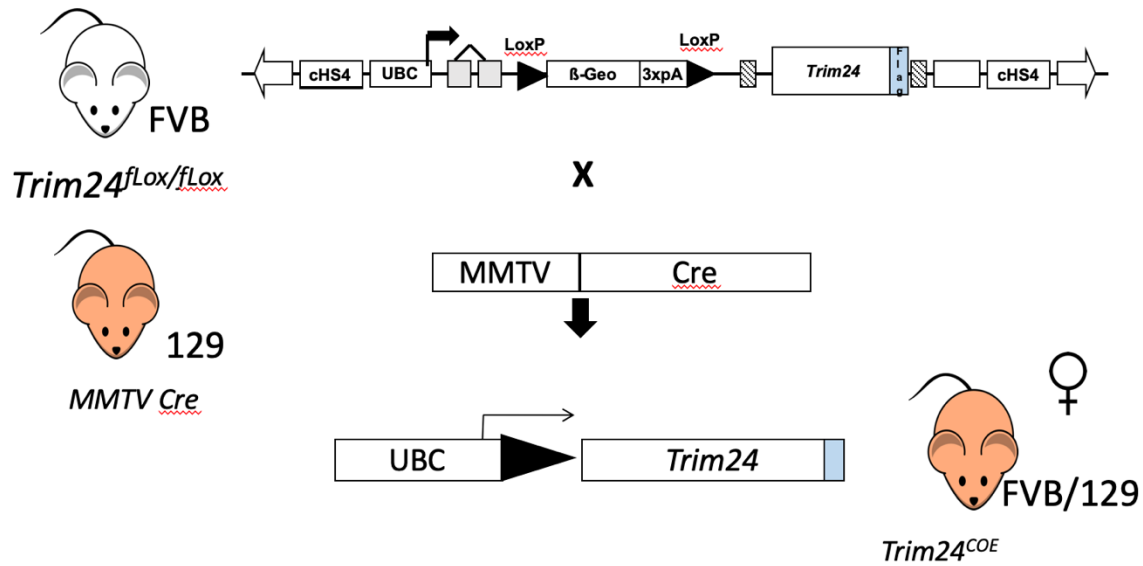


**Figure 4: Generation of *Trim24<sup>COE</sup>* mouse line.**

FVB stands for Friend Virus B, a strain used for transgenic injection; MMTV-Cre stands for mouse mammary tumor virus long terminal repeat (LTR) promoter-Cre recombinase; LoxP-β-Geo-3xpA-LoxP, the floxed stop codon; UBC promoter, human ubiquitin C. *Trim24<sup>COE</sup>*, the resulting mouse model that conditionally overexpressed TRIM24 in mammary epithelial cells.

(Figure from Dr. Shiming Jiang)

From three different *Trim24<sup>COE</sup>* mouse mammary tumor-derived cell lines (mouse tumor number 567, 64 and 897), I generated spheroid lines *Trim24<sup>COE-567</sup>*, *Trim24<sup>COE-64</sup>*, and *Trim24<sup>COE-897</sup>*. Over expression of TRIM24 was confirmed by western blot (Figure 5). Spheroids generated from an MMTV-Cre spontaneous tumor-derived cell line were used as a control (MMTV<sup>CRE-823</sup>) with low level of TRIM24 expression, also confirmed by western blot (Figure 5). TRIM24 over expression was also validated by Immunofluorescent staining, along with cytokeratin 14 staining for the cytoplasm of basal epithelial cells (Figure 6). To summarize, *Trim24<sup>COE-567</sup>* and *Trim24<sup>COE-64</sup>* spheroid expressed approximately 2-fold increase of TRIM24, while *Trim24<sup>COE-897</sup>* spheroid showed about 4-fold increase of TRIM24 compared to the TRIM24 level in MMTV<sup>CRE-823</sup> spheroids.

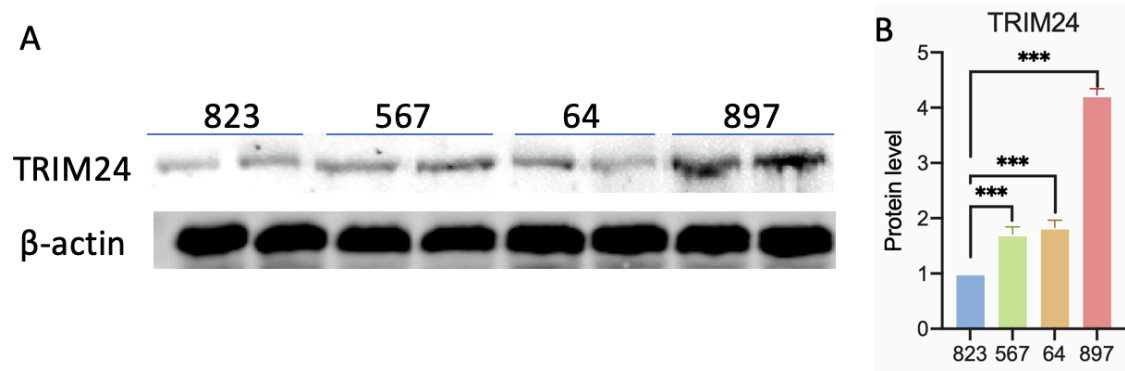


**Figure 5: Over expression of TRIM24 in *Trim24*<sup>COE</sup> spheroids confirmed by western blot.**

A) Duplicates of each sample were load to run this western blot. 823 stands for MMTV<sup>CRE</sup>-<sup>823</sup> spheroid; 567 stands for *Trim24*<sup>COE-567</sup>; 64 stands for *Trim24*<sup>COE-64</sup>; and 897 stands for *Trim24*<sup>COE-897</sup>. B) Quantification of and statistical analysis of the TRIM24 western blot;  $p < 0.0001$ , \*\*\*\*;  $p < 0.001$ , \*\*\*;  $p < 0.01$ , \*\*;  $p < 0.05$ , \*.

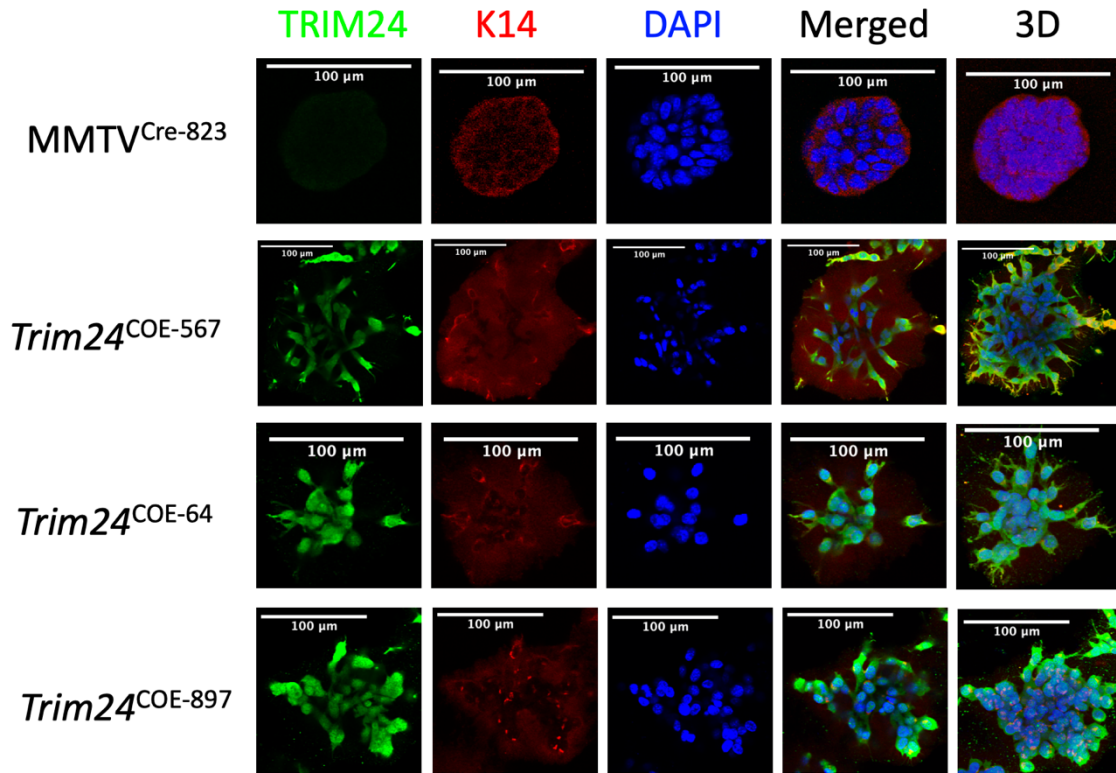


**Figure 6: Over expression of TRIM24 in *Trim24*<sup>COE</sup> spheroids confirmed by IF staining.**

TRIM24 (green), cytokeratin 14 (K14, red), and DAPI-stained nuclei (blue) IF staining was shown. *Trim24*<sup>COE</sup> spheroids showed brighter TRIM24 signals compared to the MMTV<sup>Cre-823</sup> spheroid; K14 (red) was stained to indicate the cytoplasm of basal epithelial cells and showed similar IF signals across the MMTV<sup>Cre-823</sup> spheroid and *Trim24*<sup>COE</sup> spheroids. 3D images were reconstructed from 2D z-stacks images by Fiji (ImageJ package).

In recent years, multiple studies reported that normal-like mammary spheroids display a cystic phenotype with a hollow center, while mammary spheroids derived from tumor cells often exhibit a “grape-like” or completely discohesive phenotype [1][2][41][8]. Using bright-field microscopy, I observed a distinct difference in morphology between the MMTV<sup>Cre-823</sup> control and *Trim24*<sup>COE</sup> spheroids on day 4 of culture (Figure 7). The MMTV<sup>Cre-823</sup> control formed normal-cystic spheroids with a diameter less than 100  $\mu$ m, while

*Trim24*<sup>COE</sup> spheroids were larger in size, ranged from 150 µm to 200 µm. Dysregulated cellular basal-apical polarity and planar polarity is a morphological feature of aggressive tumors [42]. Basal-apical polarity separates the basal epithelial cells, which are associated with adhesion and signaling, with the apical components; while planar polarity organizes the cells across an epithelial cell sheet surface. Disruption of these cell polarity programs contributes to cell migration and invasion in breast cancer [43]. Over expression of TRIM24 leads to the formation of irregularly shaped spheroids with filopodia extending into the surrounding Matrigel, which is a characteristic of disturbed planar polarity (Figure 7).

To further investigate the role of TRIM24 in this transformation, I created spheroids from *Trim24*<sup>COE</sup> primary cells that were transduced with vectors bearing inducible shRNAs that target *Trim24* RNA for degradation and reduced expression (knockdown) of *Trim24*. Using *Trim24*<sup>COE-64</sup> and *Trim24*<sup>COE-897</sup>, doxycycline-inducible shTrim24 lines were generated and named as shCT-64 (control) and shTrim24-64, shCT-897 (control) and shTrim24-897. After 48 hours of 1 µg of doxycycline induction, western blots showed that knockdown efficiency of shTrim24-64 was approximately 50% while shTrim24-897 has about 40% knockdown according to the quantification from western blots (Figure 8A). The knockdown of TRIM24 was also validated by IF staining – nuclear TRIM24 signal (green) was visibly decreased in the two shTrim24 lines and cytokeratin 14 (red) staining the cytoplasm of basal epithelial cells was unchanged (Figure 8B). The size of the spheroids also dramatically decreased in shTrim24-64 and shTrim24-897 and invasive filopodia were almost abolished upon TRIM24 knock down (Figure 7).

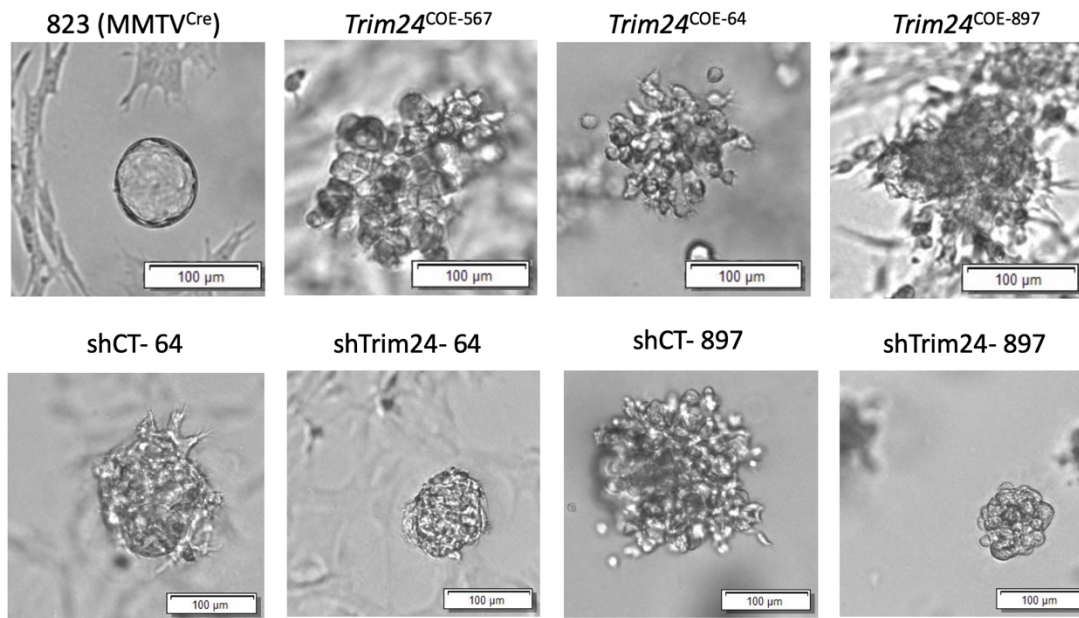


**Figure 7: Morphology of *Trim24*<sup>COE</sup> spheroids.**

Brightfield images were taken on day 4 of spheroid culture with 20x magnification. (Scale bar = 100 μm). MMTV<sup>Cre-823</sup> spheroids had circular shapes and their diameters were around 70 to 80 μm. *Trim24*<sup>COE-567</sup>, *Trim24*<sup>COE-64</sup> and *Trim24*<sup>COE-897</sup> spheroids had irregular and disorganized shapes and their long-axis diameters ranged from 150 μm to 200 μm. Spheroid diameters decreased upon TRIM24 knockdown in shTrim24-64 and shTrim24-897 compared to shCT-64 (control) and shCT-897 (control) respectively. *Trim24*<sup>COE-897</sup> spheroids grew out invasive filopodia and knocking down TRIM24 in shTrim24-897 inhibited the formation of filopodia.

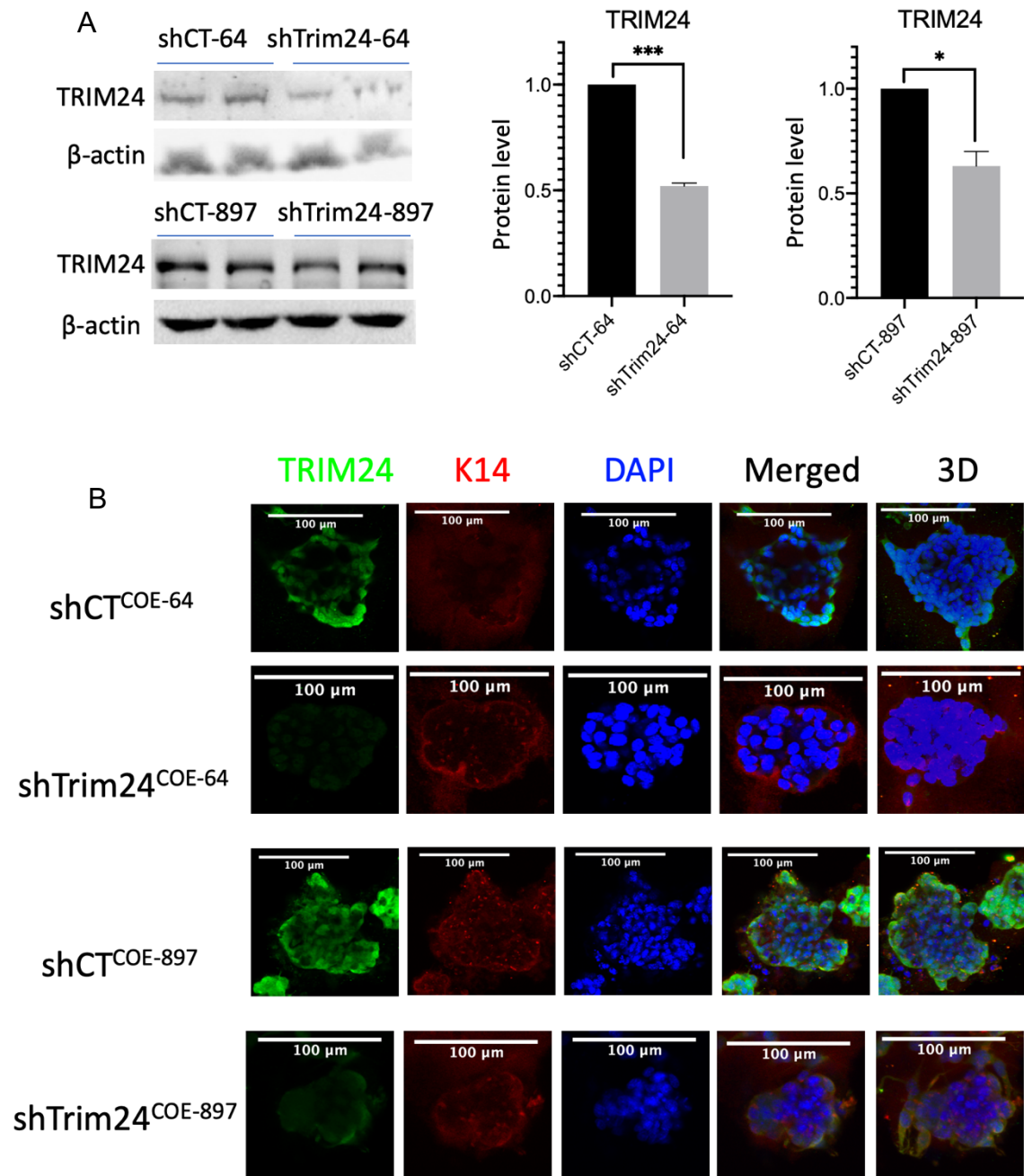


**Figure 8: Knock-down of TRIM24 in shTrim24-64 and shTrim24-897 spheroids confirmed by western blots and IF staining.**

A) All bands were normalized against a beta-actin loading control, then shTrim24 samples were normalized against shCT samples to show the decreased fold change. ( $p < 0.0001$ , \*\*\*\*;  $p < 0.001$ , \*\*\*;  $p < 0.01$ , \*\*;  $p < 0.05$ , \*) B) TRIM24 (green), cytokeratin 14 (K8, red), and DAPI-stained nuclei (blue) IF staining was shown; TRIM24 signals were greatly reduced

in shTrim24-64 and shTrim24-897 compared to the staining in their controls. Cytokeratin 14 (K14, red) signal was not altered by TRIM24 knockdown. 3D images were reconstructed with 2D z-stacks images by Fiji.

To quantify the spheroid size and invasive phenotype resulting from TRIM24 over expression, I assessed the diameter and invasion percentage (invasion %) of the *Trim24*<sup>COE</sup> spheroids with Fiji, an image processing package based on ImageJ software. Twenty spheroids were randomly picked and long-axis spheroid diameters were measured using the tool in the software. *Trim24*<sup>COE</sup> spheroids showed significantly higher spheroid diameters compared to the MMTV<sup>Cre-823</sup> control. Knocking down TRIM24 decreased the spheroid diameters to < 100  $\mu\text{m}$  in both shTrim24-64 and shTrim24-897 lines (Figure 9). To calculate invasion percentage, fifteen spheroids from each imaging fields were randomly selected, and spheroids with distinctive filopodia were counted as invasive spheroids. The total number of invasive spheroids were divided by the total amount of all spheroids to get the invasive values for one imaging field. Ten different imaging fields were used to get an average value of invasion% for each spheroid line. In this way, we showed that three *Trim24*<sup>COE</sup> spheroids have much higher invasiveness compared to the MMTV<sup>Cre-823</sup> control (Figure 10). Knocking down TRIM24 led to about 10% decrease in the percentage of invasive spheroids in the shTrim24-897 compared to the shCT-897 (Figure 10).

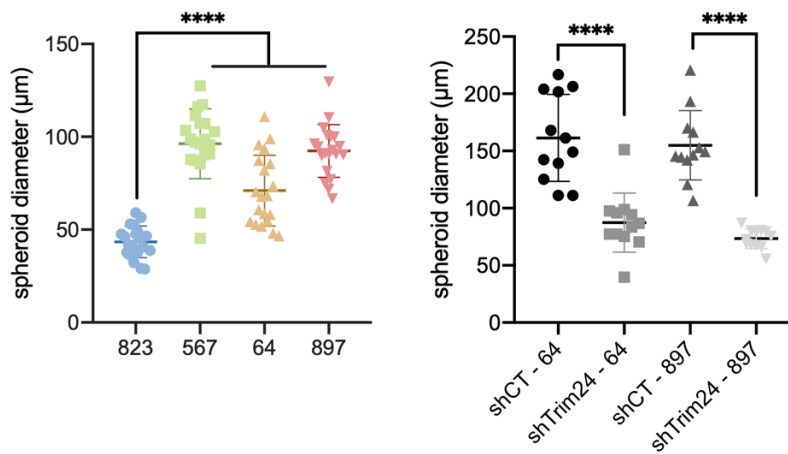


**Figure 9: Quantification of spheroid diameters showed TRIM24-dependent spheroid size.**

Twenty randomly selected spheroids in the MMTV<sup>Cre-823</sup> and three *Trim24*<sup>COE</sup> spheroid lines were measured and quantification showed *Trim24*<sup>COE</sup> spheroids had significantly larger diameters versus control. Knocking-down of TRIM24 decreased the spheroid diameters in both shTrim24-64 and shTrim24-897 compared to their controls. (p<0.0001, \*\*\*\*; p<0.001, \*\*\*; p<0.01, \*\*; p<0.05, \*)

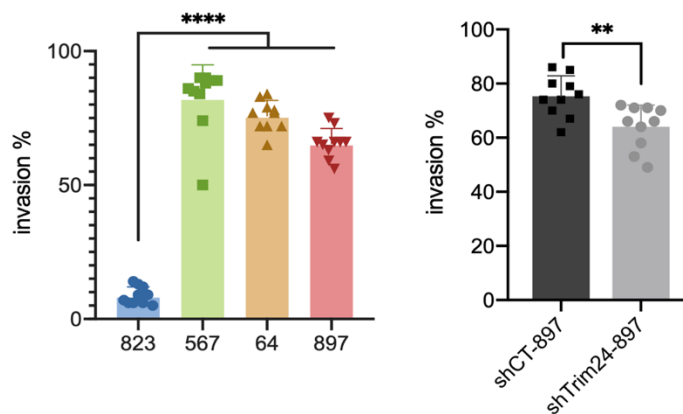


**Figure 10: Quantification of spheroid invasion percentage showed TRIM24-dependent invasiveness.**

Fifteen spheroids from ten image fields were randomly selected and invasive spheroids with filopodia were counted. The calculated invasion percentage showed 60% to 80% of *Trim24*<sup>COE</sup> spheroids were invasive, while only around 10% of MMTV<sup>Cre-823</sup> spheroids are



invasive. Knocking-down TRIM24 in shTrim24-897 decreased invasion percentage by 10%. ( $p < 0.0001$ , \*\*\*\*;  $p < 0.001$ , \*\*\*;  $p < 0.01$ , \*\*;  $p < 0.05$ , \*)

EMT is a dynamic cellular process whereby epithelial cells lose signature characteristics of cell-cell junctions, apical-basal polarity, and attachment to the basement membrane and acquire more mesenchymal cell features, e.g. back-front polarity, vimentin-based intermediate filaments [44]. Typical, although not always consistent, signs of EMT include reduced expression of epithelial cell marker E-cadherin and increased expression of mesenchymal cell marker N-cadherin [45]. In addition to gaining mobile properties during EMT, cancer cells also enhance their resistance to anticancer drug and oxidative stress, become able to escape senescence, and acquire self-renewal cancer stem cell (CSC) characteristics [46]. During the formation of metastases, it's believed that cancer cells go through mesenchymal-to-epithelial transition (MET) to regain the epithelial cell features and form the secondary tumor [44]. Some cancer cells do not reach complete EMT, but retain epithelial cell features and concurrently express both epithelial/mesenchymal (E/M) phenotype [47]. This is termed as partial EMT and it is recognized that partial EMT actually leads to higher metastatic potential than complete EMT [47]. Intriguingly, I found in *Trim24*<sup>COE</sup> spheroids, both E-cadherin and N-cadherin expression were largely reduced compared to control (Figure 11). Knocking down TRIM24 did not reverse the expression of E-cadherin or the expression of mesenchymal cell maker N-cadherin (Figure 11).

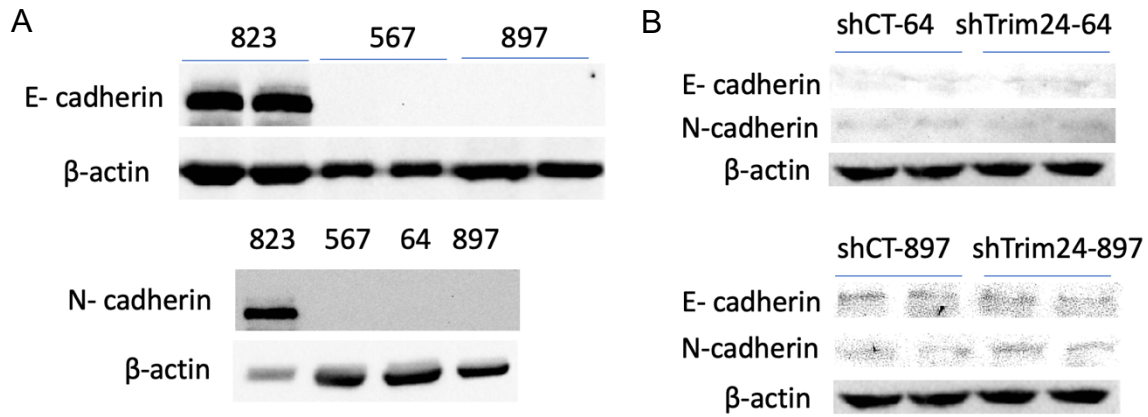


**Figure 11: Western blots of EMT markers in *Trim24*<sup>COE</sup> spheroids**

Duplicates of shCT and shTrim24 sample were load to run this western blot. 823 stands for MMTV<sup>CRE-823</sup> spheroid; 567 stands for *Trim24*<sup>COE-567</sup>; 64 stands for *Trim24*<sup>COE-64</sup>; and 897 stands for *Trim24*<sup>COE-897</sup>. A) Both epithelial cell marker E-cadherin and mesenchymal cell marker N-cadherin were downregulated in *Trim24*<sup>COE</sup> spheroids. B) Knock-down of TRIM24 only decreased N-cadherin protein expression.

The EMT process is known to be regulated by transcriptional factors (EMT-TFs): Snai1/2, Twist1/2, and Zeb1/2, which can lead to increased invasion and migration of cancer cells [44, 48-51]. Therefore, I also assessed the expression of these typical EMT-TFs in the *Trim24*<sup>COE</sup> spheroids and found that *Snai1* and *Twist1* were unchanged in *Trim24*<sup>COE-567</sup> but both were downregulated in *Trim24*<sup>COE-64</sup> and *Trim24*<sup>COE-897</sup> spheroids. *Zeb1*, however, was dramatically upregulated in *Trim24*<sup>COE-567</sup> and *Trim24*<sup>COE-64</sup>, but not in *Trim24*<sup>COE-897</sup> (Figure 12). It has been reported that over expression of NRF2 prevents cells undergo complete EMT and increased E-cadherin as well as ZEB-1 which shows a partial EMT phenotype [52]. Here, *Trim24*<sup>COE</sup> spheroids did not express epithelial cell marker E-cadherin or mesenchymal cell marker N-cadherin, but exhibit increased expression of *Zeb1*. It is possible that *Trim24*<sup>COE</sup> spheroids undergo partial EMT which could be a result of over expression of NRF2. NRF2 over expression in the *Trim24*<sup>COE</sup> lines will be elaborated in a later section.

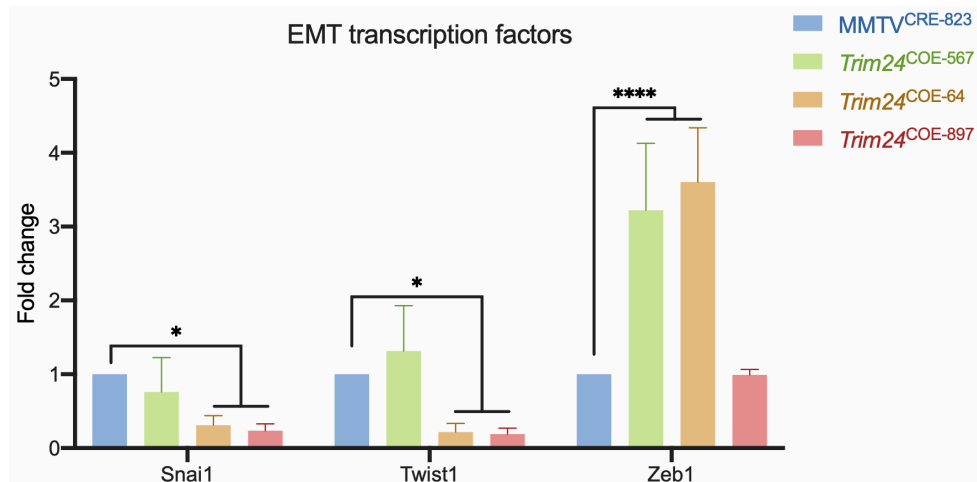


**Figure 12: Different EMT transcription factor mRNA expression across *Trim24*<sup>COE</sup> spheroid lines.**

RT-qPCR data of *Trim24*<sup>COE</sup> spheroid was normalized with ribosomal gene 18s, then normalized against MMTV<sup>Cre-823</sup>. Three *Trim24*<sup>COE</sup> spheroid lines showed different mRNA expression levels of typical EMT transcription factors. (p<0.0001, \*\*\*\*; p<0.001, \*\*\*; p<0.01, \*\*; p<0.05, \*)

As an oncogenic transcription factor in breast cancers, c-MYC is known to promote EMT, increase the proliferation of cancer stem-like cells and rewire metabolic pathways that support the bioenergetic needs of proliferating cells [53-55]. c-MYC expression was upregulated in *Trim24*<sup>COE-897</sup> spheroids, and its expression was reduced upon TRIM24 knockdown (Figure 13).

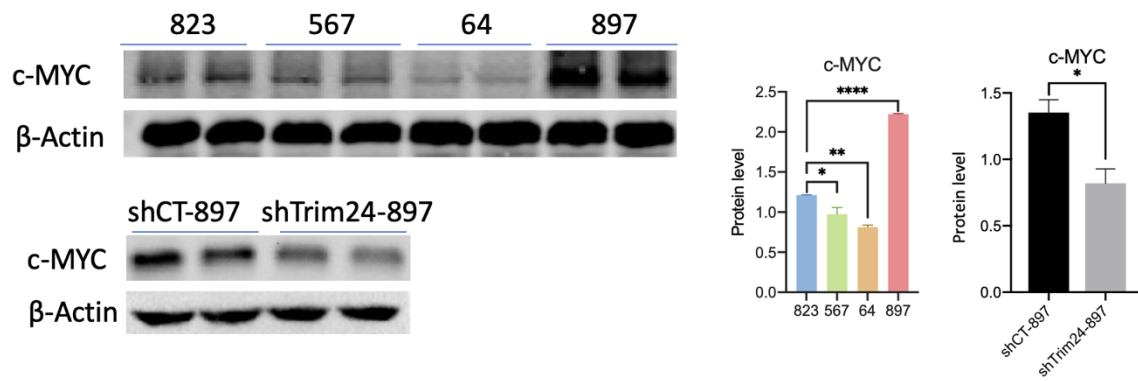


**Figure 13: Western blots of c-MYC and their quantification showed TRIM24-dependnet c-MYC at protein level.**

Duplicates of each sample were load to run this western blot. 823 stands for MMTV<sup>CRE-823</sup> spheroid; 567 stands for *Trim24*<sup>COE-567</sup>; 64 stands for *Trim24*<sup>COE-64</sup>; and 897 stands for *Trim24*<sup>COE-897</sup>. Quantification of western blot showed *Trim24*<sup>COE-897</sup> had about two-fold increase in c-MYC protein level compared to MMTV<sup>CRE-823</sup>; c-MYC protein level was decreased upon TRIM24 knock down. (p<0.0001, \*\*\*\*; p<0.001, \*\*\*; p<0.01, \*\*; p<0.05, \*)

In recent years, EMT has been linked to an increase in a self-renewing cancer stem cell (CSC) population [49, 50]. In the context of breast cancer, breast cancer stem cells (BCSCs) are rare cells that reportedly play a critical role in tumor initiation, proliferation and metastasis. Kruppel-like factor 4 (KLF4), sex determining region Y-box 2 (SOX2) and cell-surface glycoprotein CD44 are typical cancer stem cell markers that are highly expressed in cancer [56-58]. I found that CD44 and KLF4 expression were both upregulated in *Trim24*<sup>COE-897</sup> spheroids; SOX2 expression was particularly high in *Trim24*<sup>COE-64</sup> (Figure 14). Knock-down of TRIM24 decreased expression of CD44 and SOX2 but not KLF4. which indicated that stemness characteristics of *Trim24*<sup>COE</sup> cells are dependent on high levels of TRIM24 expression (Figure 14). Although driven by the same oncoprotein TRIM24, the *Trim24*<sup>COE-567</sup>, *Trim24*<sup>COE-64</sup> and *Trim24*<sup>COE-897</sup> lines were generated from three different endpoint mouse mammary tumors and showed different degrees of TRIM24 over expression at the protein level (Figure 5). Based on the findings

shown so far, three *Trim24*<sup>COE</sup> lines exhibited different levels of EMT marker and stemness markers which indicates heterogeneity among the three spheroid lines.

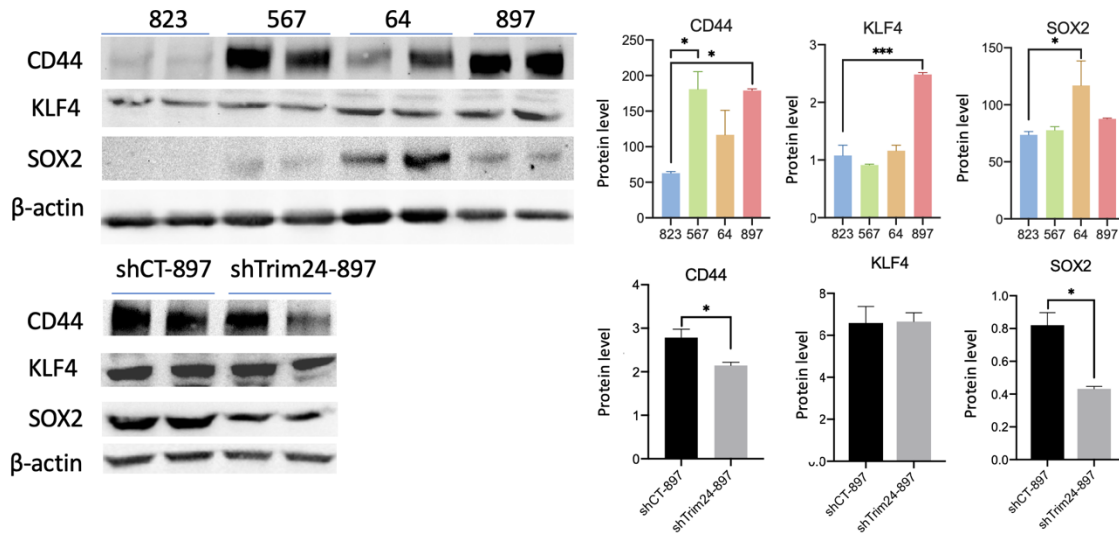


**Figure 14: Western blots and their quantification showed different BCSCs marker levels in *Trim24*<sup>COE</sup>, shCT-897 and shTrim24-897 spheroids.**

Duplicates of each sample were load to run this western blot. 823 stands for MMTV<sup>CRE-823</sup> spheroid; 567 stands for *Trim24*<sup>COE-567</sup>; 64 stands for *Trim24*<sup>COE-64</sup>; and 897 stands for *Trim24*<sup>COE-897</sup>. Quantification of western blots showed high CD44 and KLF4 in *Trim24*<sup>COE-897</sup>; high SOX2 in *Trim24*<sup>COE-64</sup> spheroids; and *Trim24*<sup>COE-567</sup> showed only high CD44. Knock-down of TRIM24 in shTrim24-897 decreased CD44 and SOX2 but not KLF at the protein level. (p<0.0001, \*\*\*\*; p<0.001, \*\*\*; p<0.01, \*\*; p<0.05, \*)

A major advantage of using three-dimensional spheroids is that they closely recapitulate the normal or pathological *in vivo* mammary duct architecture. Unlike 2D cell monolayers, the typical mammary 3D culture has multiple layers of cells that consist of outer basal membrane,  $\alpha 6/\beta 4$  integrins, and tight junctions on the luminal side that express ZO-1 [59]. This strictly defined basal-apical polarity is a key feature of the mammary gland unit and loss of this feature is a critical event of tumor development [34, 59-62]. The

literature shows that mammary organoids are arranged into two distinct layers, which are basal epithelial cell layers that express cytokeratin-14 (K14), p63 and smooth muscle actin (SMA) and luminal epithelial cells expressing cytokeratin-8 (K8) and progesterone receptor (PR) [35]. To investigate if TRIM24 over expression affected the differentiation of these cell compartments, I used IF staining and show that *Trim24*<sup>COE</sup> spheroids lacked a luminal epithelial cell population but knocking down TRIM24 increased the expression of luminal marker K8 on the inner layer of cells (Figure 15,16).

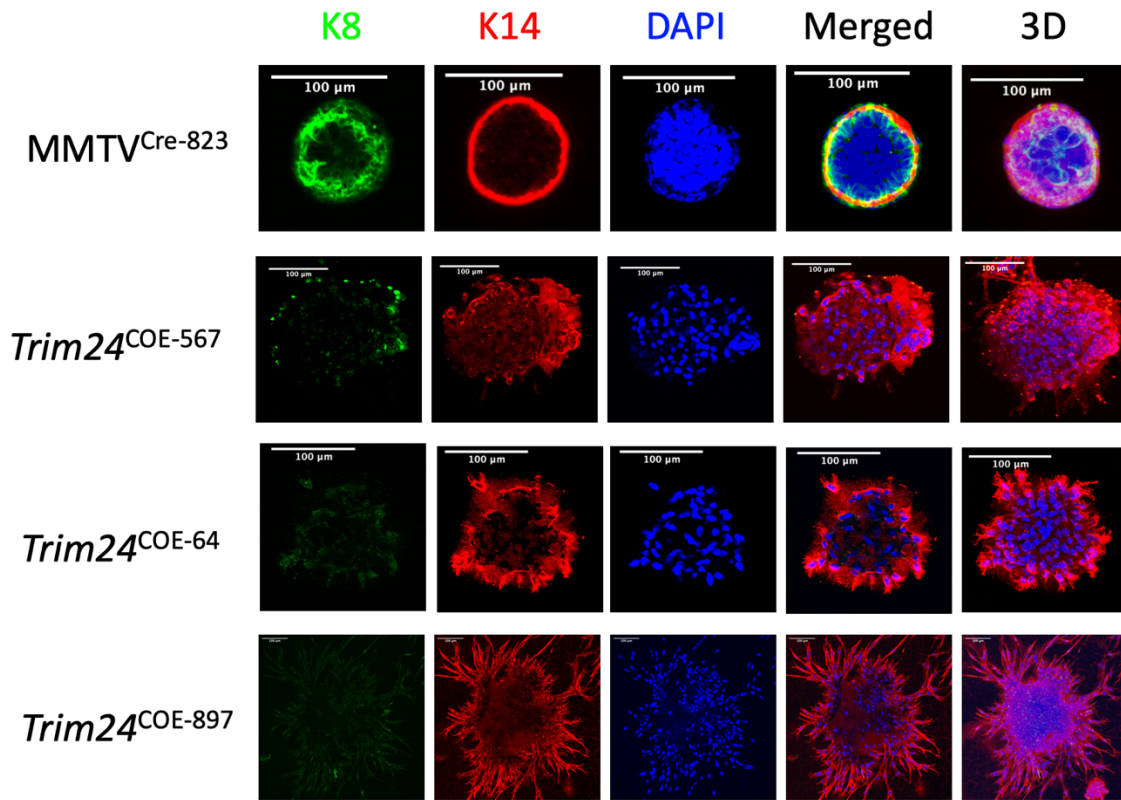


**Figure 15: IF staining of K8 (luminal epithelial cell) and K14 (basal epithelial cell) in *Trim24*<sup>COE</sup> spheroids.**

Cytokeratin 8 (K8, green), cytokeratin 14 (K14, red), and DAPI-stained nuclei (blue) IF staining showed MMTV<sup>Cre-823</sup> had strong K8 signal whereas *Trim24*<sup>COE</sup> spheroids had very weak K8 signals; K14 signals were similar across the spheroid lines. 3D images were reconstructed with 2D z-stacks images by Fiji.

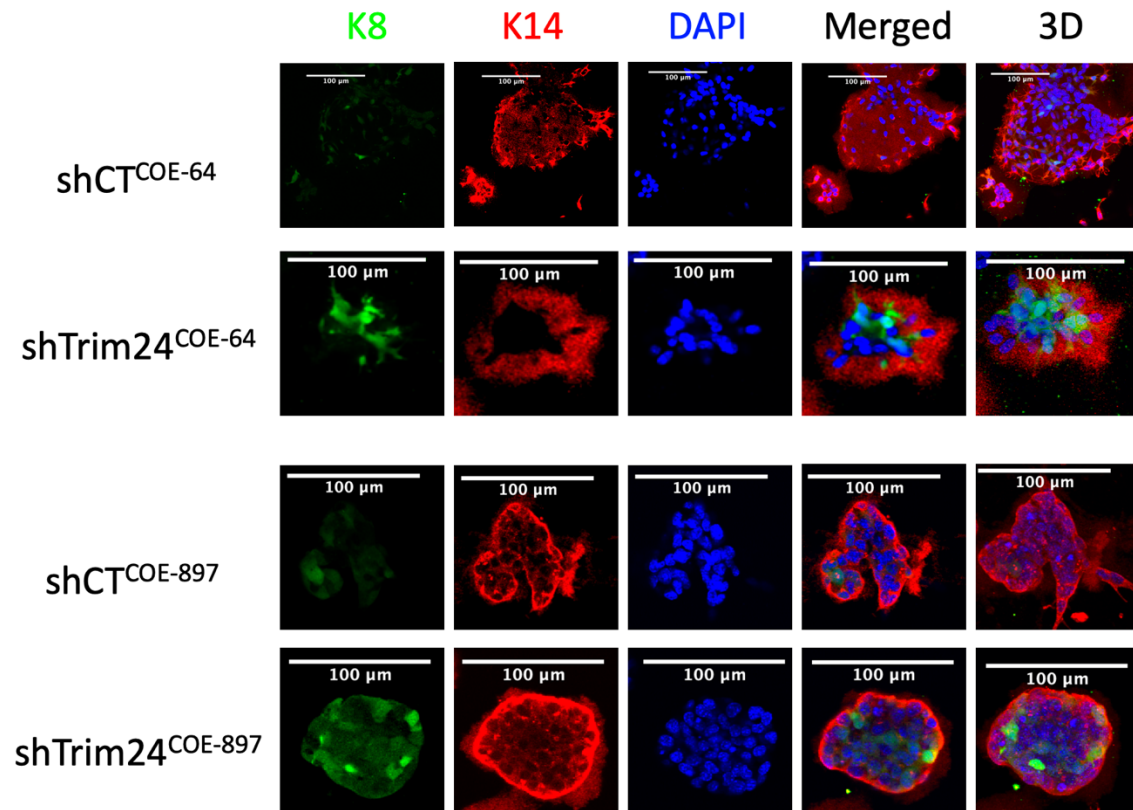


**Figure 16: IF staining of K8 (luminal epithelial cell) and K14 (basal epithelial cell) in *Trim24*<sup>COE</sup>, shCT-897 and shTrim24-897 spheroids.**

Cytokeratin 8 (K8, green), cytokeratin 14 (K14, red), and DAPI-stained nuclei (blue) IF staining showed that K8 signals recovered upon TRIM24 knockdown in shTrim24-64 and shTrim24-897; K14 signals were not affected upon TRIM24 knock down. 3D images were reconstructed with 2D z-stacks images by Fiji.

Immunoblots also showed that K8 expression was low in *Trim24*<sup>COE</sup> spheroids and knocking down TRIM24 increased K8 expression (Figure 17). These results delineated that TRIM24 over expression led to less differentiated mammary spheroids. These findings further support the results showing that TRIM24 over expression contributes to increased stemness and decreased differentiation.

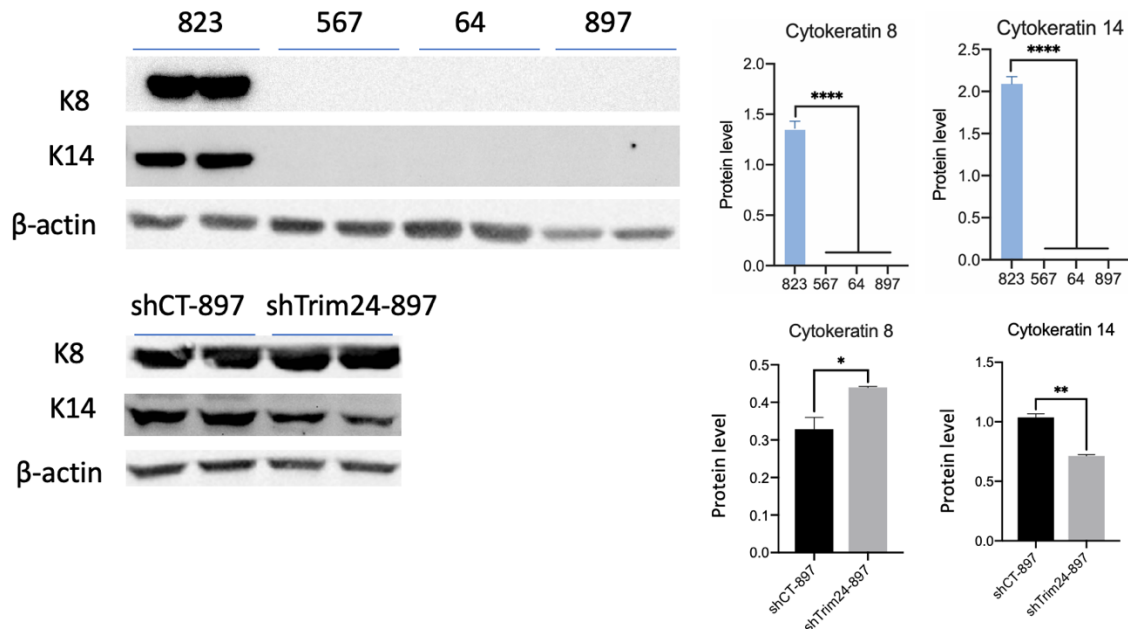


**Figure 17: Western blot of K8 (luminal epithelial cell) and K14 (basal epithelial cell) in shCT-897 and shTrim24-897 spheroids.**

Duplicates of each sample were load to run this western blot. 823 stands for MMTV<sup>CRE-823</sup> spheroid; 567 stands for *Trim24*<sup>COE-567</sup>; 64 stands for *Trim24*<sup>COE-64</sup>; and 897 stands for *Trim24*<sup>COE-897</sup>. Quantification of western blots showed no cytokeratin 8 (K8) or cytokeratin 14 (K14) expression in *Trim24*<sup>COE</sup> spheroids; knocking down TRIM24 increased K8 but decreased K14 at the protein level. (p<0.0001, \*\*\*\*; p<0.001, \*\*\*; p<0.01, \*\*; p<0.05, \*)

*Trim24*<sup>COE-567</sup>, *Trim24*<sup>COE-64</sup> and *Trim24*<sup>COE-897</sup> spheroids were generated from cells collected and cultured from endpoint mouse mammary tumors at the endpoint driven by Trim24 over expression. Consistent with spheroid type-specific, differential expression of EMT markers and stemness markers, their heterogeneity was further confirmed by RNA-sequencing (Figure 18). Three *Trim24*<sup>COE</sup> spheroid lines exhibited an RNA expression profile that was distinct from the MMTV<sup>Cre-823</sup> control. While within a broader *Trim24*<sup>COE</sup> spheroid grouping, *Trim24*<sup>COE-567</sup>, *Trim24*<sup>COE-64</sup> and *Trim24*<sup>COE-897</sup> also showed distinct clustering patterns (Figure 18). Between technical replicates, for example *Trim24*<sup>COE-897-1</sup> and *Trim24*<sup>COE-897-2</sup>, the clustering pattern is consistent with each other, indicating good



sample preparation. The heterogeneity among the three tumor-derived spheroid lines is also apparent in their metabolic characteristics, which will be elaborated further in the following sections.

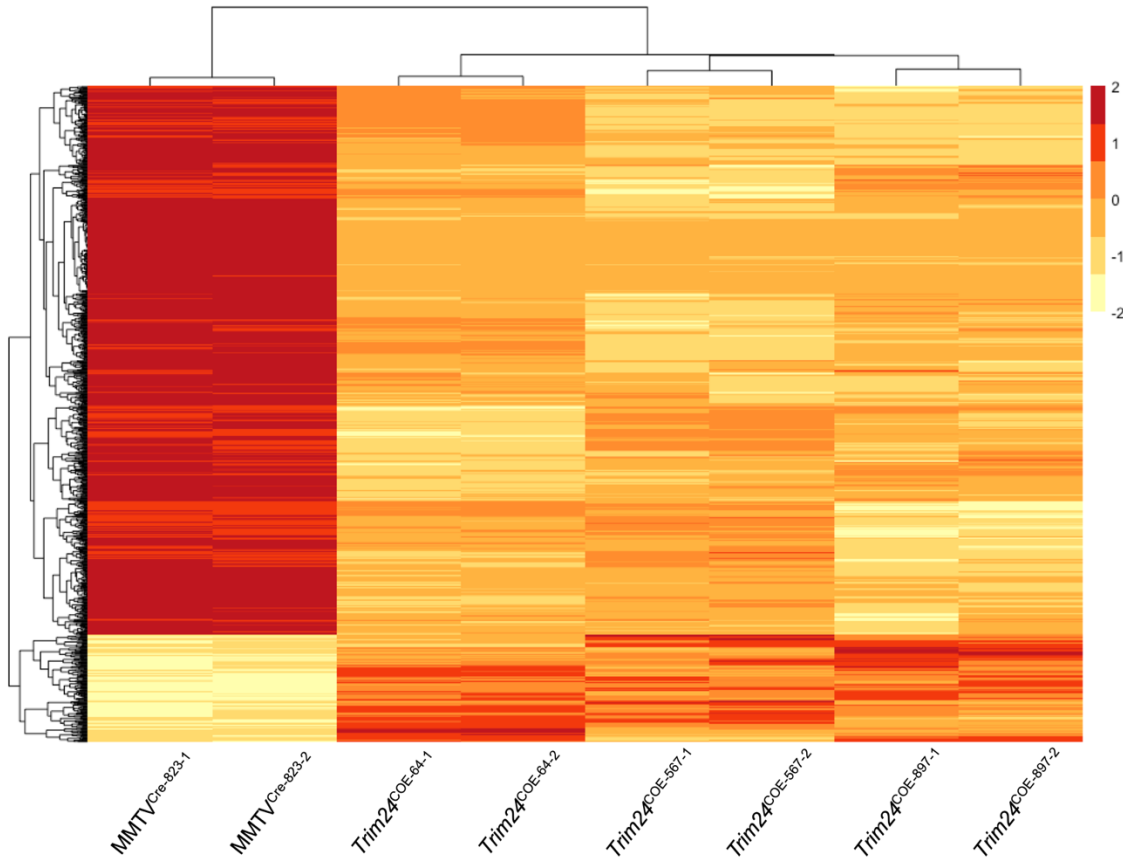


**Figure 18: RNA sequencing data revealed heterogeneity within the *Trim24*<sup>COE</sup> spheroid groups**

RNA-sequencing analysis done by Dr. Vrutant Shah; duplicates of each spheroid line were used. Three *Trim24*<sup>COE</sup> spheroid lines exhibited clustering profiles that was distinct from the MMTV<sup>Cre-823</sup> control; while *Trim24*<sup>COE-567</sup>, *Trim24*<sup>COE-64</sup> and *Trim24*<sup>COE-897</sup> showed distinct clustering patterns compared with each other.

Highly invasive cancer cells have been reported to exhibit a stronger ability to buffer reactive oxidative stress [9, 11, 14, 63-65]. Here, we used the CellRox reagent, a

fluorogenic probe that measures intracellular ROS level in live cells. In an oxidative state, CellRox emits strong fluorescent signals while in a reduced state CellRox does not or emit very weak fluorescence. We found that *Trim24*<sup>COE</sup> spheroids had lower ROS profiles than the MMTV<sup>CRE-823</sup> control (Figure 19). The shCT-64 and shCT-897 spheroid lines showed similar ROS abundance, compared to their parental lines, while both shTrim24-64 and shTrim24-897 exhibited much higher intracellular ROS compared to their knock-down controls (Figure 20).

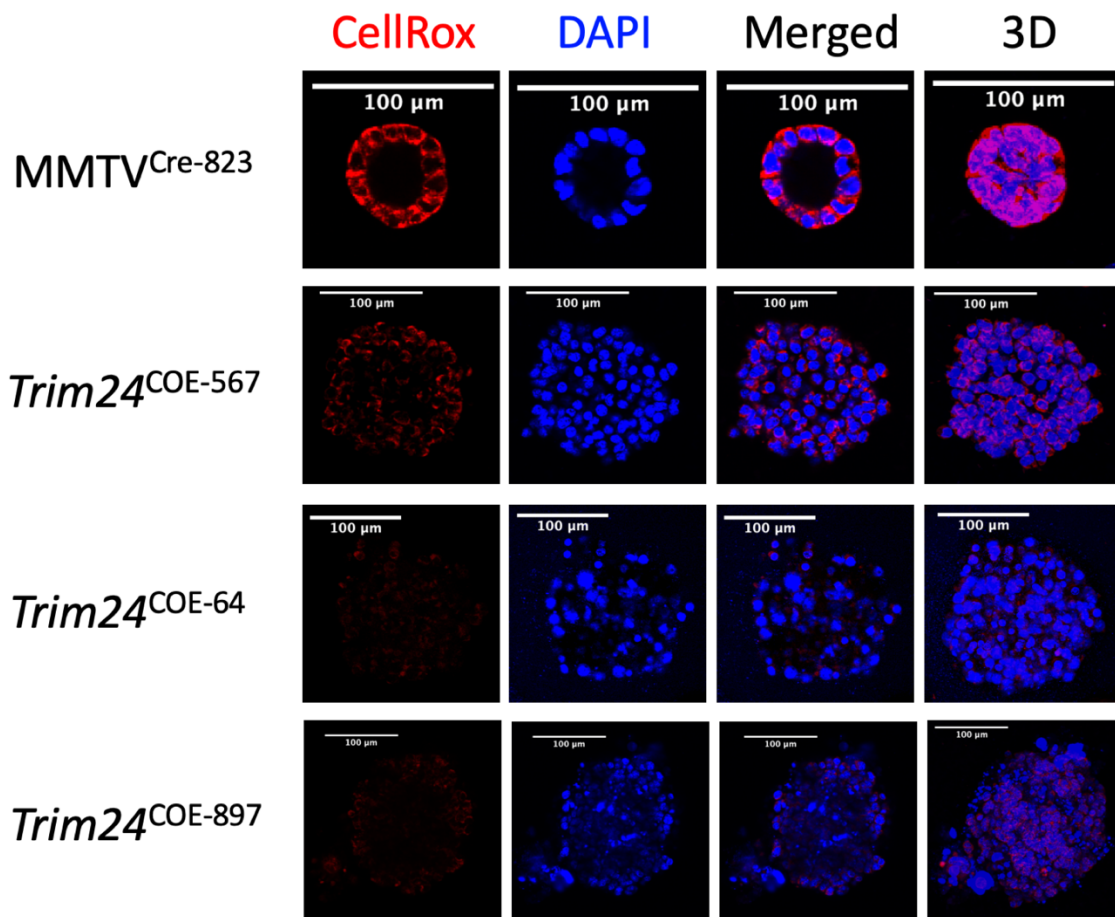


**Figure 19: CellIROX staining showed low intracellular ROS in *Trim24*<sup>COE</sup> spheroids compared to the MMTV<sup>CRE-823</sup> control.**

CellIROX Deep Red (red), a reagent that detects intracellular ROS showed three *Trim24*<sup>COE</sup> spheroid lines had lower CellIROX signals compared to the control spheroid;

DAPI nuclei (blue) staining was shown in blue; 3D images were reconstructed with 2D z-stacks images by Fiji.

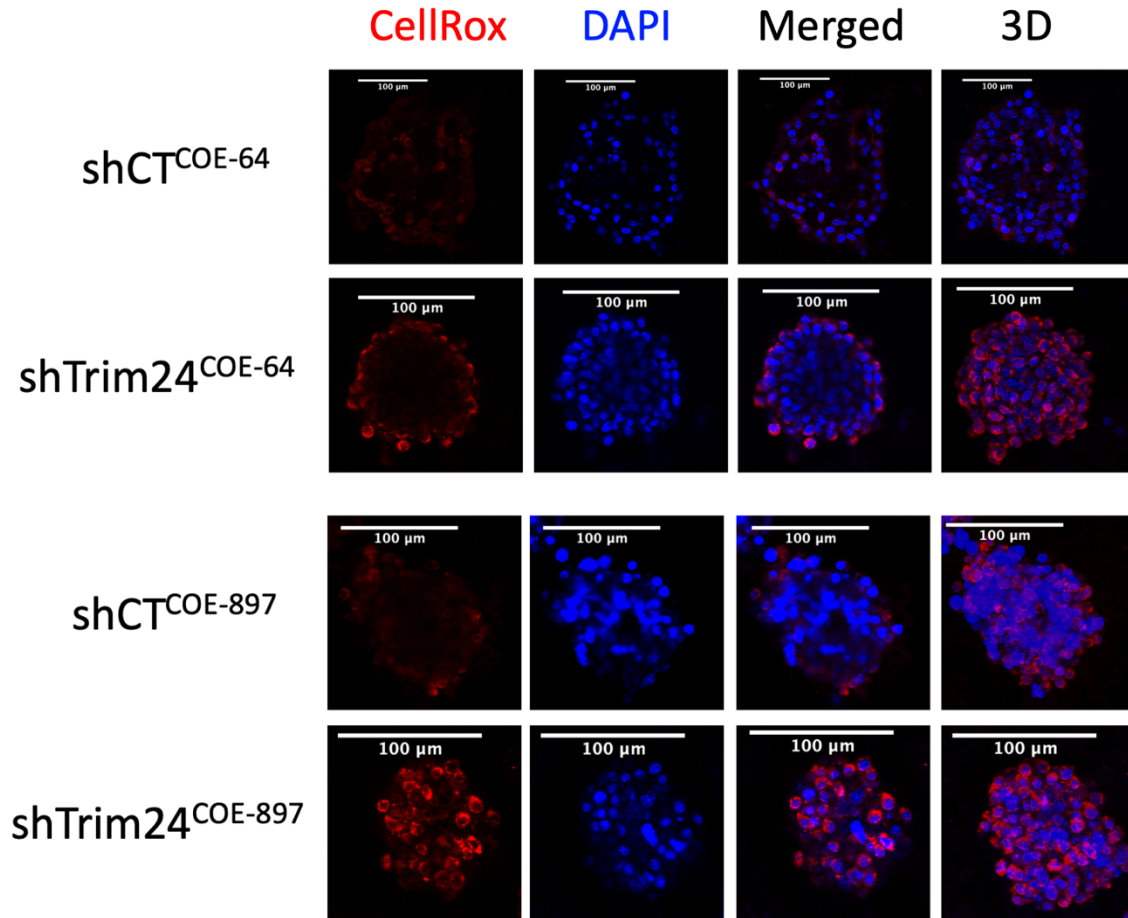


**Figure 20: Low intracellular ROS levels in spheroids were dependent upon TRIM24 overexpression**

CellROX Deep Red (red), and DAPI-stained nuclei (blue) staining was shown. Knocking down TRIM24 increased the CellROX signals in shTrim24-64 and shTrim24-897 compared to their control. 3D images were reconstructed with 2D z-stacks images by Fiji.

H<sub>2</sub>O<sub>2</sub>, a major ROS entity generated from mitochondrial oxidative respiration, was added to the spheroids to induce oxidative stress. After 24 hours of H<sub>2</sub>O<sub>2</sub> treatment, CellRox ROS staining showed increased intracellular ROS in MMTV<sup>CRE-823</sup> spheroids, while *Trim24*<sup>COE</sup> spheroids did not show significant changes in ROS level responding to

H<sub>2</sub>O<sub>2</sub> (Figure 21). In shTrim24-897, intracellular ROS was slightly induced upon H<sub>2</sub>O<sub>2</sub> treatment compared to the shCT-897, which indicated that knocking down TRIM24 diminishes adaption to oxidative stress in this spheroid tumor-derived line (Figure 22).

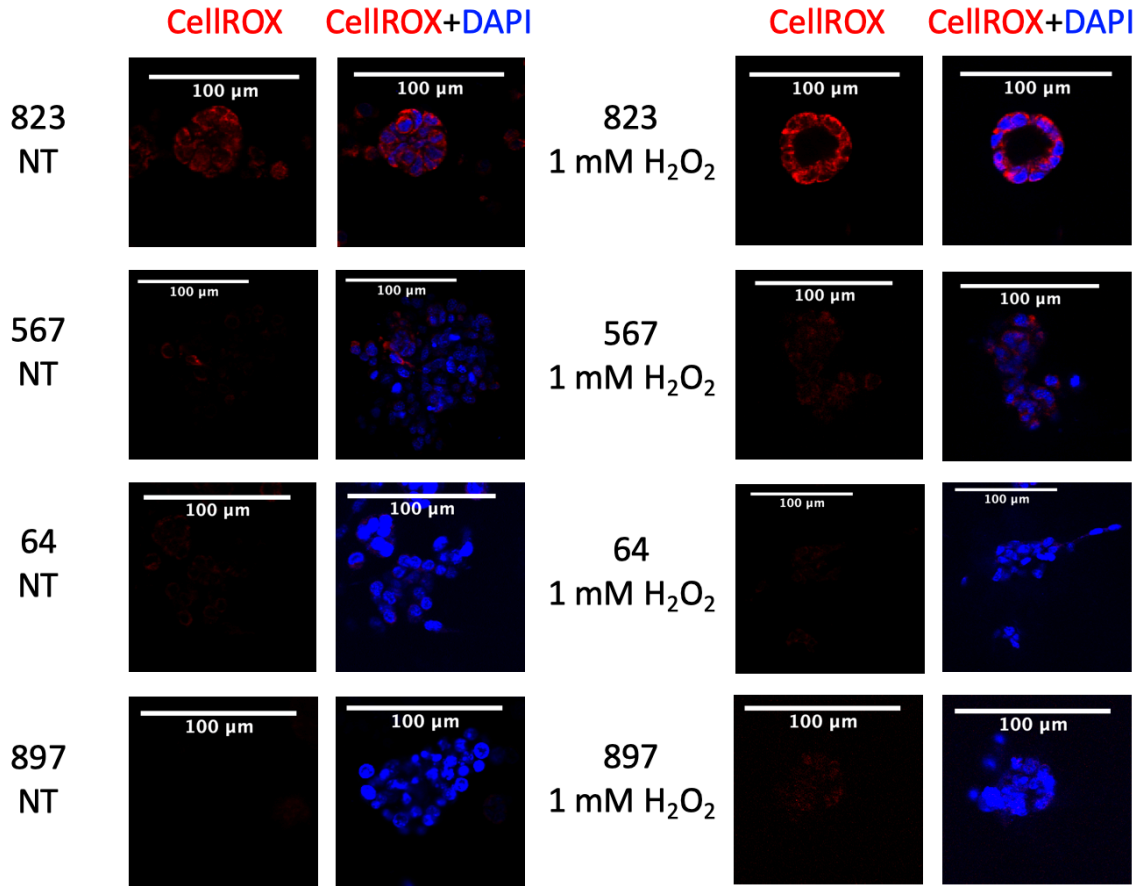


**Figure 21: Intracellular ROS increased in MMTV<sup>Cre-823</sup> spheroids after 24 hours of H<sub>2</sub>O<sub>2</sub> treatment but not in *Trim24*<sup>COE</sup> spheroids.**

CellIROX Deep Red (red), and CellIROX combined with DAPI nucleus stain (blue) showed increased CellIROX signal in MMTV<sup>Cre-823</sup> spheroids after H<sub>2</sub>O<sub>2</sub> treatment.

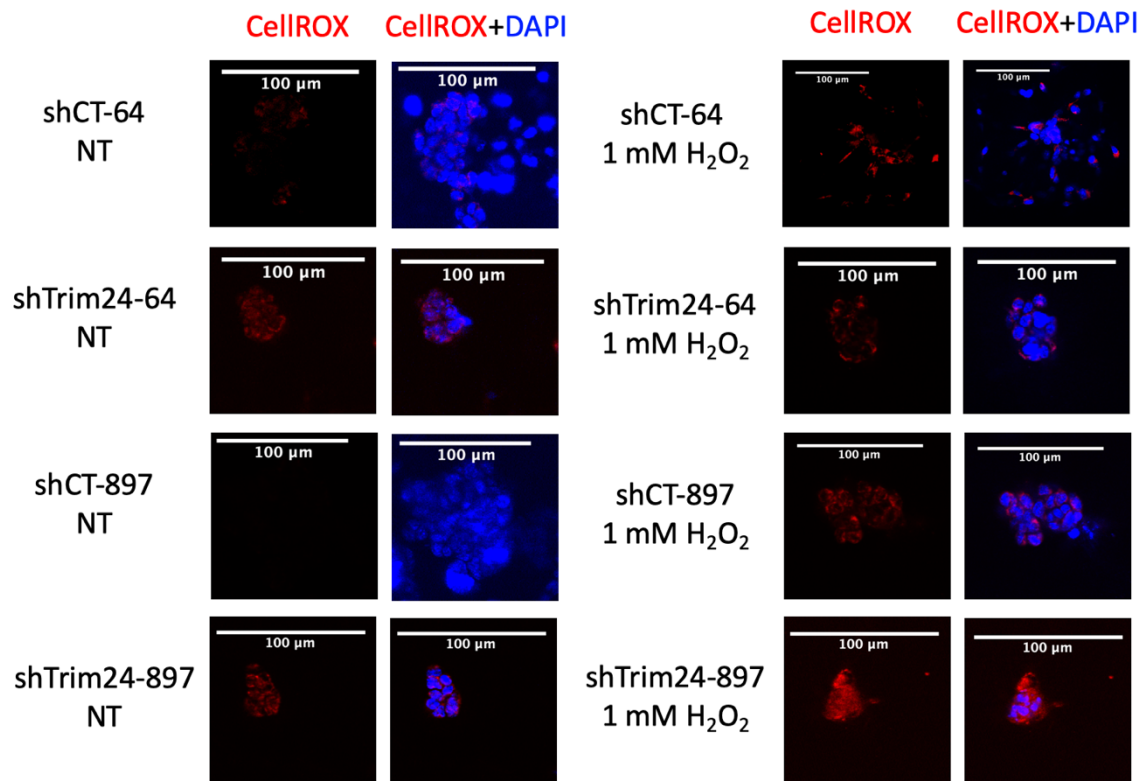


**Figure 22: Intracellular ROS increased in shTrim24-897 spheroids after 24 hours of  $H_2O_2$  treatment but not in shCT spheroids.**

CellROX Deep Red (red), and CellROX combined with DAPI nucleus stain (blue) showed increased CellROX signal in shTrim24-897 spheroids after  $H_2O_2$  treatment; while shTrim24-64 did not show increased CellROX signal after  $H_2O_2$  treatment.

To further investigate whether lower cellular ROS, observed in *Trim24*<sup>COE</sup> spheroids, is due to less mitochondrial activity or increased ROS scavenging, MitoSOX, a reagent that specially enters mitochondria, was used to determine the mitochondrial ROS level. Similar to CellROX signals, we found that *Trim24*<sup>COE</sup> spheroids exhibited lower mitochondrial ROS levels (Figure 23). The MitoSox signals were not affected by 1 mM  $H_2O_2$  treatment for 24 hours. Mitochondrial ROS level plays an important role in mitochondria-mediated cell death pathways [66]. Since addition of extracellular  $H_2O_2$  did not affect the ROS production in the mitochondria, the cell death triggered by 1 mM  $H_2O_2$

treatment for 24 hours was not mediated by mitochondria which will be elaborated in later section.

The mitochondrial stress test by Seahorse is an assay to assess mitochondrial function through measuring oxygen consumption rate (OCR) before and after drug administration. In the beginning, before any drug treatment, basal OCR was recorded. Then oligomycin was added to cells to block ATP synthase (complex V) of the electron transport chain (ETC), followed by carbonyl cyanide-4 (trifluoromethoxy) phenylhydrazone (FCCP) administration to break the mitochondrial membrane potential. Lastly Rotenone and antimycin was added to inhibit complex I and complex III respectively which resulted in shut down of mitochondrial respiration [67]. This assay revealed a lower basal respiration, maximal respiration and ATP-linked respiration, as well as lower spare capacity in *Trim24*<sup>COE-567</sup> and *Trim24*<sup>COE-897</sup> spheroids (Figure 24). Knocking-down TRIM24 in shTrim24-897 spheroids further decreased the mitochondrial capacity to respond to stress which caused further decreased in basal respiration, maximal respiration, ATP-linked respiration, and spare capacity (Figure 24). Lower mitochondrial activity could explain the lower mitochondrial and cellular ROS level in *Trim24*<sup>COE</sup> spheroids. Knocking down TRIM24 increased cellular ROS but further decreased mitochondrial activity, which indicated increased ROS upon TRIM24 knockdown was not contributed by mitochondria.

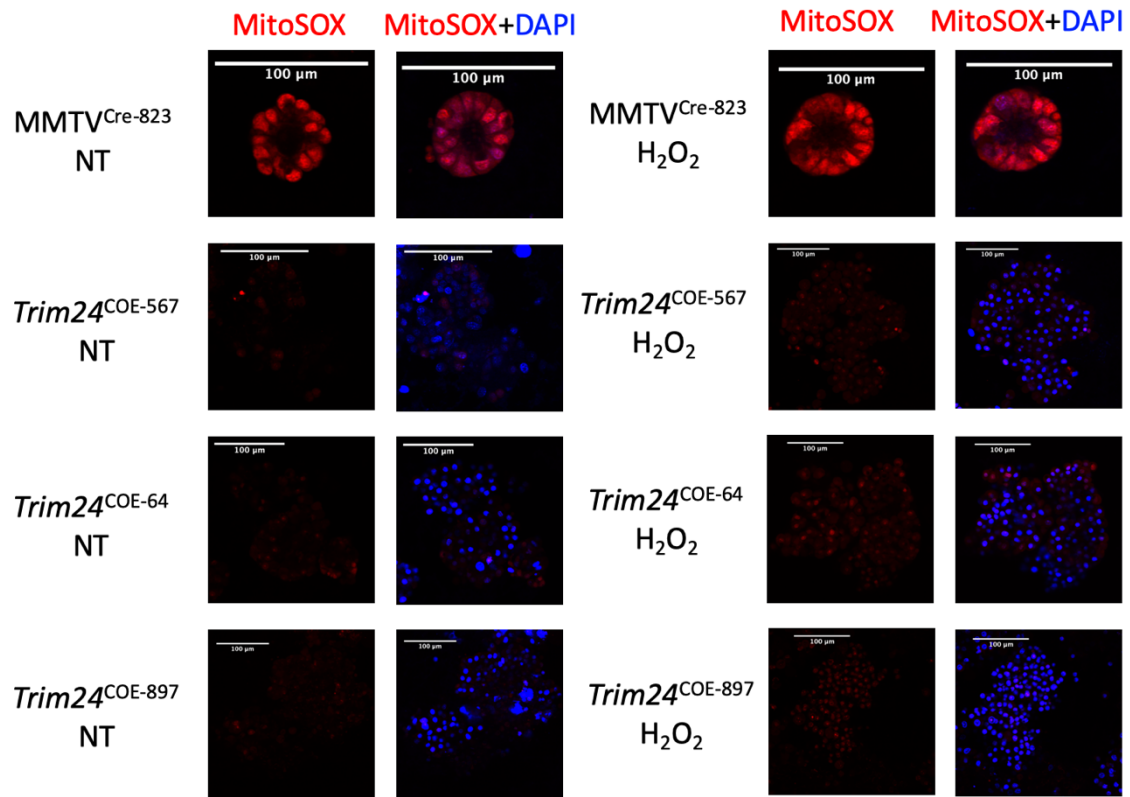


**Figure 23: MitoSOX staining of mitochondrial ROS after 24 hours of H<sub>2</sub>O<sub>2</sub> treatment did not change in MMTV<sup>Cre-823</sup> or *Trim24*<sup>COE</sup> spheroids.**

MitoSOX Orange (red), and MitoSOX combined with DAPI nucleus stain (blue) showed unchanged MitoSOX signal in all spheroid lines after H<sub>2</sub>O<sub>2</sub> treatment.



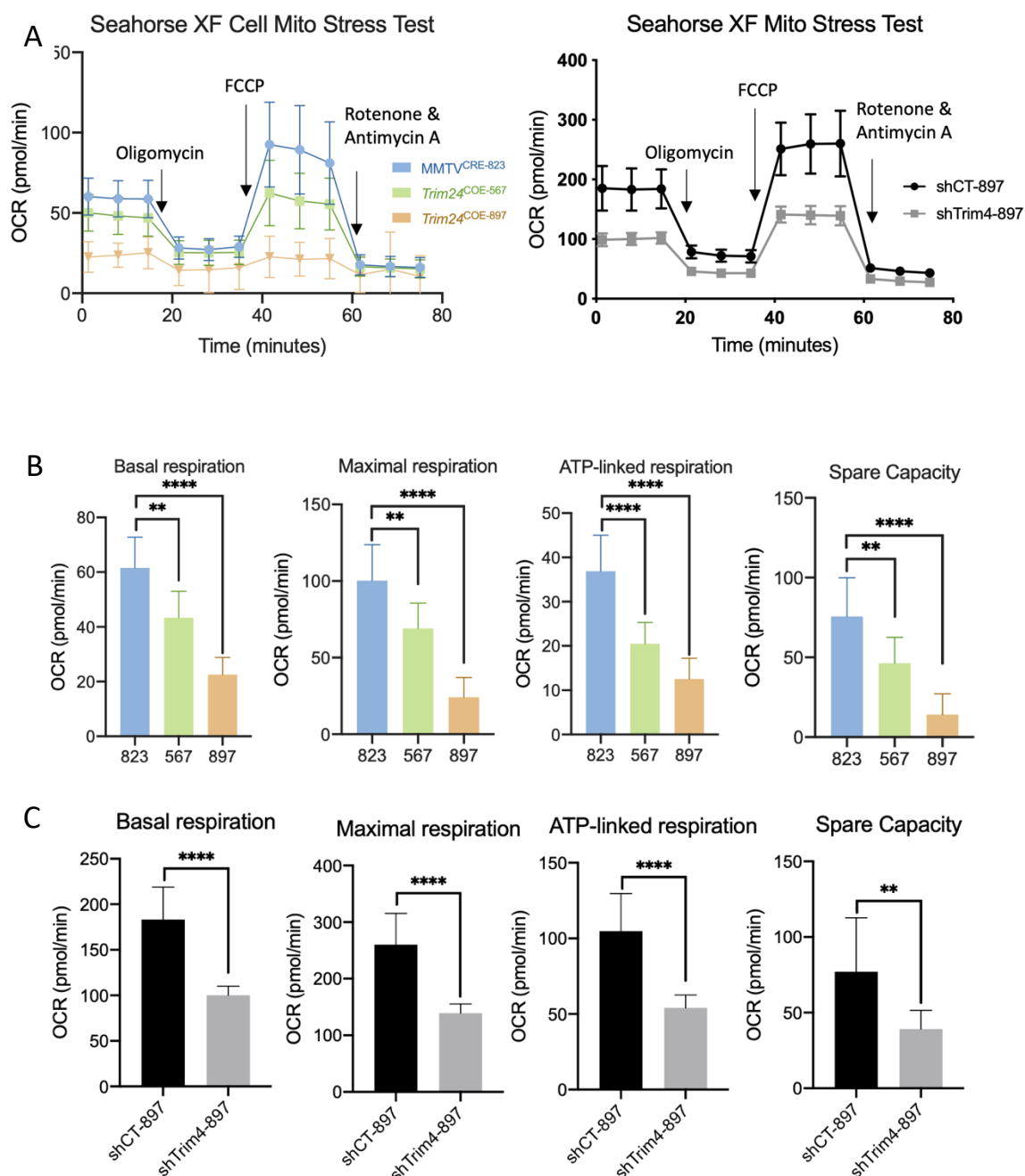


**Figure 24: *Trim24*<sup>COE</sup> spheroid showed decreased overall response to Seahorse Mito Stress Test and TRIM24 knock down further decreased the response.**

Basal respiration, the OCR reading before drug treatment; ATP-linked respiration, the absolute OCR reduction after oligomycin administration; Maximal respiration, the absolute OCR reading after FCCP administration; Spare capacity, the increase in OCR above baseline after FCCP treatment. ( $p < 0.0001$ , \*\*\*\*;  $p < 0.001$ , \*\*\*;  $p < 0.01$ , \*\*;  $p < 0.05$ , \*)



NADPH is an essential reducing equivalent that replenishes reduced glutathione (GSH) in order for cells to combat oxidative stress. Due to increased ROS level results from fast proliferation and oncogene signaling, proliferative cells are especially in greater need of NADPH [8, 11, 68-71]. With a colorimetric total NADP(H) assay, we found that total NADP<sup>+</sup> and NADPH levels as well as the reduced NADPH level were significantly higher in the *Trim24*<sup>COE</sup> spheroids (Figure 25). Upon TRIM24 knockdown, the total NADP(H) levels showed a 5-fold decrease in shTrim24-64 and a 2-fold decrease in shTrim24-897 versus parental controls. Reduced NADPH showed a 15% decrease upon TRIM24 knock-down, suggesting that TRIM24 knockdown greatly decreased the NADP<sup>+</sup> abundance instead of NADPH to cause a decrease in total NADP(H) (Figure 25).

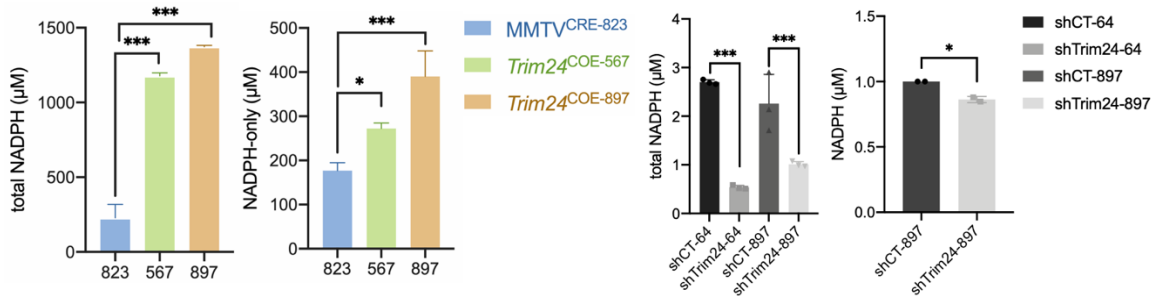


**Figure 25: Total NADP(H) and reduced NADPH levels were upregulated in *Trim24*<sup>COE</sup> spheroids while decreased upon TRIM24 knock down.**

NADP(H) and reduced NADPH abundance were determined using a total NADP(H) or reduced NADPH standard curve, triplicates of samples were used. *Trim24*<sup>COE</sup> spheroids showed about six to seven times higher total NADP(H) compared to the control. *Trim24*<sup>COE</sup> spheroids showed about two-fold increase in reduced NADPH level. ( $p < 0.0001$ , \*\*\*\*;  $p < 0.001$ , \*\*\*;  $p < 0.01$ , \*\*;  $p < 0.05$ , \*)

## TRIM24 over expression diverts glycolysis flux for more NADPH production

The most direct source of NADPH production in mammalian cell is the pentose phosphate pathway (PPP), mediated by glucose-6-phosphate dehydrogenase (G6PD) and 6-phosphogluconate dehydrogenase (PGD) [72, 73]. Additionally, quantitative flux analysis showed that a comparable amount of NADPH production is also contributed by serine-driven one-carbon metabolism [68]. In order to investigate the source of high NADPH found in *Trim24*<sup>COE</sup> spheroids, spheroid samples were incubated with medium with the desired isotope tracer for six hours before processing and metabolite abundance was detected by liquid chromatography and mass spectrometry (LC/MS) (Figure 3A). <sup>13</sup>C<sub>6</sub>-glucose isotope tracing revealed that *Trim24*<sup>COE-897</sup> spheroids divert the glycolysis flux to the PPP shunt (Figure 26), and enzyme levels of G6PD and PGD were significantly increased in *Trim24*<sup>COE-897</sup> compared to the MMTV<sup>CRE-823</sup> control and *Trim24*<sup>COE-567</sup> spheroids (Figure 27A).

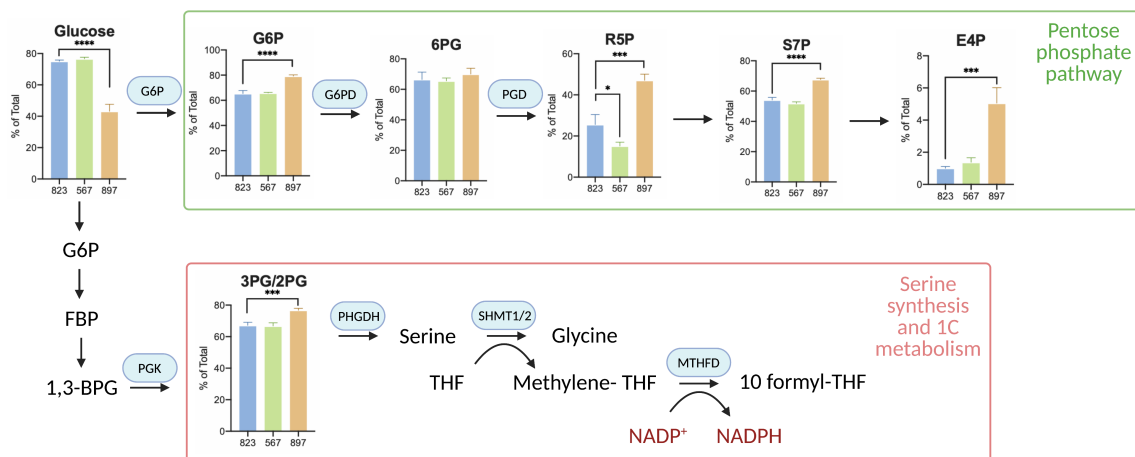


**Figure 26: <sup>13</sup>C<sub>6</sub>-glucose isotope tracing revealed increased glycolysis diversion to PPP shunt and 1C metabolism in *Trim24*<sup>COE-897</sup> spheroids.**

Metabolite abundance in PPP shunt (green square), and 1C-metabolism (pink square) indicated increased glycolysis diversion to those pathways. (p<0.0001, \*\*\*\*; p<0.001, \*\*\*; p<0.01, \*\*; p<0.05, \*)

There was also an increase in the glucose-derived total 3PG/2PG abundance. 3-phosphoglycerate (3PG) can be converted to serine through phosphoglycerate dehydrogenase (PHGDH) and phosphoserine aminotransferase (PSAT1), fueling one-carbon metabolism to produce folate and NADPH [74-77]. In TRIM24<sup>COE</sup> spheroids, the enzyme expression of PHGDH was also increased, as well as the downstream enzymes SHMT1, SHMT2, MTHFD1 (Figure 27B). The expression of PGK, PHGDH, SHMT1/2 was downregulated upon TRIM24 knockdown in shTrim24-897 spheroids, which indicated TRIM24-dependent glycolysis diversion to one-carbon metabolism (Figure 27C).

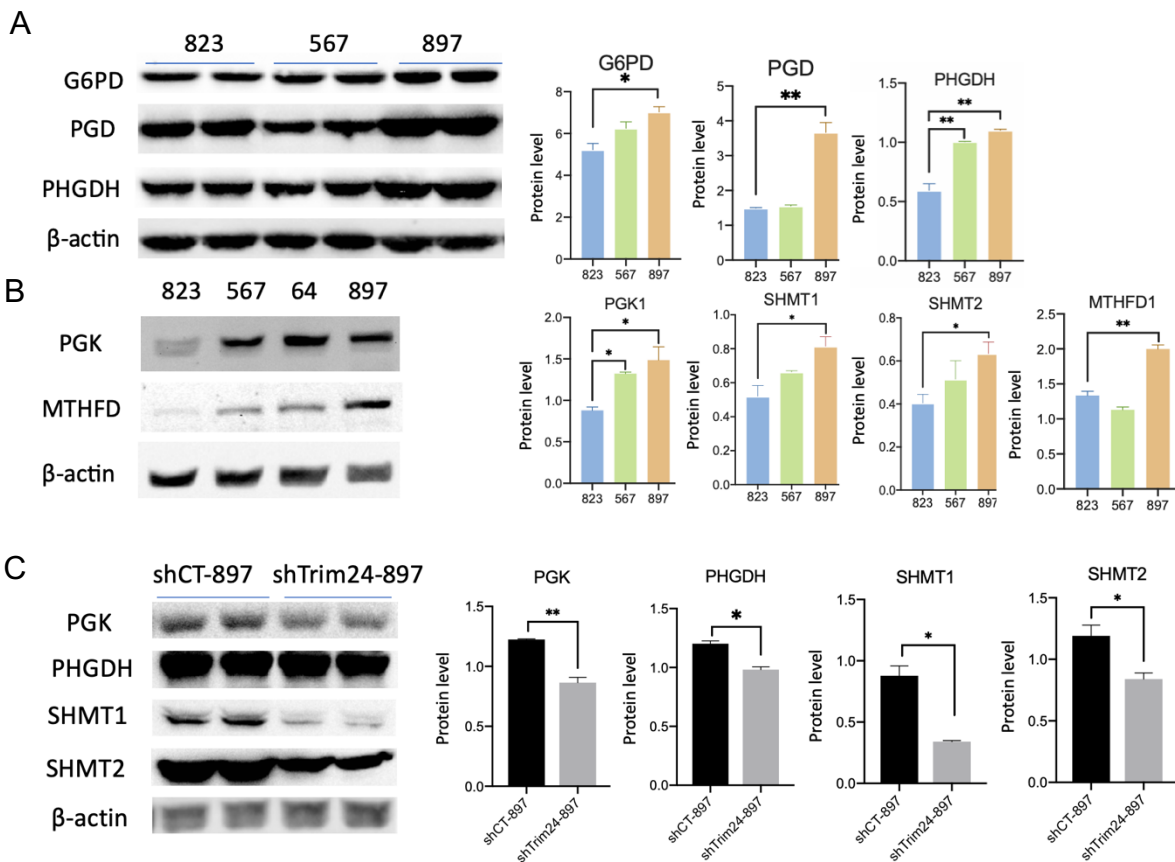


**Figure 27: Western blots of PPP and 1C metabolism pathway showed increased enzyme levels in *Trim24*<sup>COE</sup> spheroids TRIM24-dependent enzyme levels in 1C metabolism.**

Duplicates of each sample were load to run these western blots. 823 stands for MMTV<sup>CRE-823</sup> spheroid; 567 stands for *Trim24*<sup>COE-567</sup>; 64 stands for *Trim24*<sup>COE-64</sup>, and 897 stands for *Trim24*<sup>COE-897</sup>. (p<0.0001, \*\*\*\*; p<0.001, \*\*\*; p<0.01, \*\*; p<0.05, \*)

Serine is one of the non-essential amino acids (NEAAs) that has received increased attention in the field of cancer metabolism [77-79]. PHGDH, the first enzyme in *de novo* serine synthesis, is amplified in some triple-negative-breast cancers [75]. Efforts have been made to develop PHGDH-specific inhibitors to inhibit tumor growth. A selective small-molecule inhibitor of PHGDH, CBR5884, was identified through screening 800,000 drug-like compounds [80]. After treating two lines of TRIM24<sup>COE</sup> spheroids with 60  $\mu$ M of CBR5884 for 24 hours, the TRIM24<sup>COE</sup> spheroids both showed approximately 30% decrease in their viability (Figure 28) while not affecting the total NADP(H) level (Figure 28). TRIM24 knock-down sensitizes the spheroids to CBR5884: at 60  $\mu$ M, shTrim24-897 line had more than 90% decrease in its viability (Figure 28). This decrease in viability could be due to both less NADPH production and serine, glycine, and folate depletion. To investigate the NADP(H) status, we performed total NADP(H) assays as well as NADPH-only assays. Total NADP(H) was increased in *Trim24*<sup>COE-567</sup> and *Trim24*<sup>COE-897</sup> compared to the MMTV<sup>CRE-823</sup> control after 24hr-CBR5884 treatment, while the NADPH level alone was decreased in the two *Trim24*<sup>COE</sup> lines compared to the MMTV<sup>CRE-823</sup> control (Figure 29). This indicated that NADPH was reduced and NADP<sup>+</sup> was increased in both *Trim24*<sup>COE</sup> lines in response to PHGDH inhibitors.

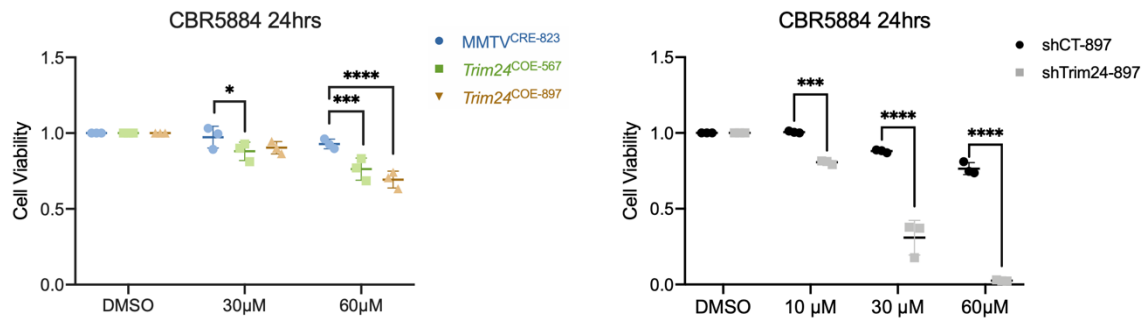


**Figure 28: CTG viability assays showed PHGDH inhibitor CBR5884 decreased *Trim24*<sup>COE</sup> spheroid viability; the decrease in viability was enhanced upon TIRM24 knock down.**

Triplicates were used for CellTitor-Glo viability assay. With 60 μM of CBR5884, both *Trim24*<sup>COE-567</sup> and *Trim24*<sup>COE-897</sup> spheroid showed significant decrease in their viability; viability of shTrim24-897 was greatly decreased upon 60 μM of CBR5884 treatment compared to the control. (p<0.0001, \*\*\*\*; p<0.001, \*\*\*; p<0.01, \*\*; p<0.05, \*)

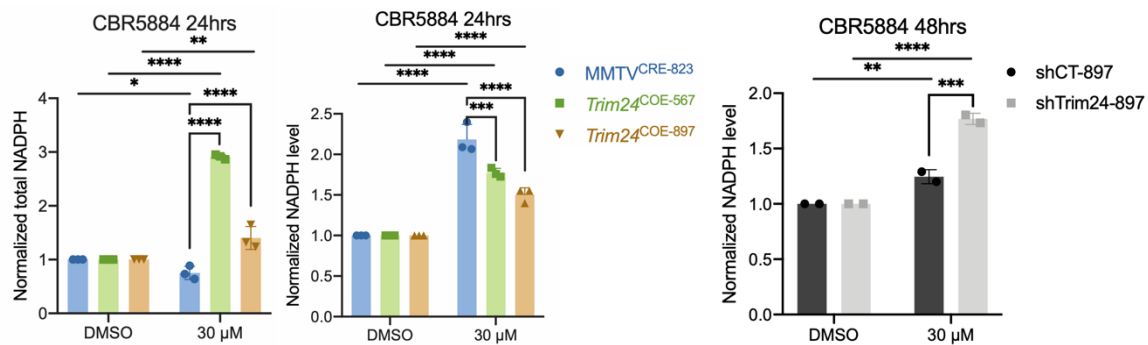


**Figure 29: Total NADP(H) and reduced NADPH assays revealed decreased reduced-NADPH level in *Trim24*<sup>COE</sup> spheroids after treated with CBR5884.**

Total NADP(H) and reduced NADPH were determined with a standard curve and CB839-treated samples were normalized to DMSO-treated control samples. Triplicates were used. (p<0.0001, \*\*\*\*; p<0.001, \*\*\*; p<0.01, \*\*; p<0.05, \*)

To test if one-carbon metabolism precursors were essential for the survival of the *Trim24*<sup>COE</sup> spheroids, we pre-treated the spheroids with CBR5884 for 24 hours then assessed rescue of spheroid viability by supplying 500  $\mu$ M 3PG in the culture media for an additional 24 hours. 3PG supplement rescued the *Trim24*<sup>COE-567</sup> and *Trim24*<sup>COE-897</sup> spheroids and increased viability more than 60% (Figure 30). Although 3PG supplement slightly rescued viability of shTrim24-897 spheroids, the effect of rescue was significantly lower than that in shCT-897 spheroids. These results indicated that TRIM24 knockdown lowers the flux of glycolysis to one-carbon metabolism, and inhibition of this diversion in the context of TRIM24 knockdown cannot be rescued by 3PG supplement (Figure 30).

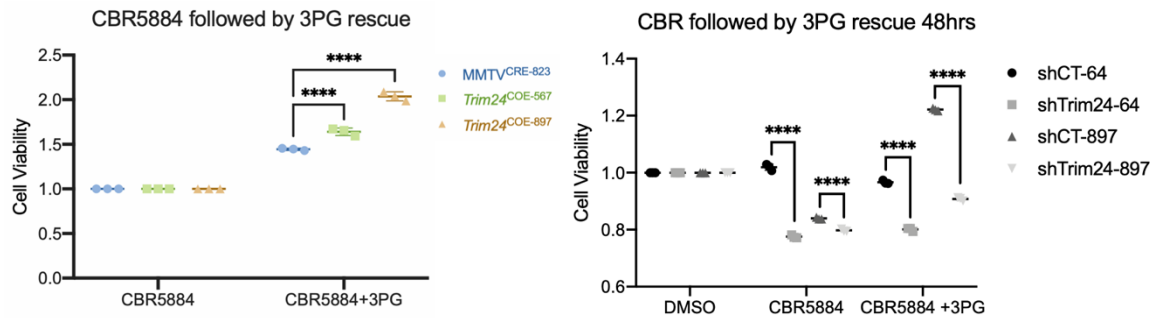


**Figure 30: 3PG supplement rescued *Trim24*<sup>COE</sup> spheroids viability but failed to rescue up TRIM24 knock down.**

Viability of *Trim24*<sup>COE-567</sup> and *Trim24*<sup>COE-897</sup> spheroids pre-treated with CBR5884 was increased after 3PG supplement. However, in shTrim24-64 and shTrim24-897, 3PG addition failed to rescued the decrease in viability due to CBR5884 treatment.

( $p < 0.0001$ , \*\*\*\*;  $p < 0.001$ , \*\*\*;  $p < 0.01$ , \*\*;  $p < 0.05$ , \*)

## TRIM24 over expression upregulated glutathione synthesis

Cancer cells often rely on high levels of glutamine and glutamate to fuel the TCA cycle for ATP production, as well as *de novo* reduced glutathione (GSH) synthesis for antioxidant defense [81-87]. With  $^{15}\text{C}_5$ -glutamine tracing, we found that *Trim24*<sup>COE-567</sup> and *Trim24*<sup>COE-897</sup> spheroids had a significantly higher abundance of glutamate and reduced glutathione compared to the MMTV<sup>CRE-823</sup> control, but not glutamine (Figure 31). This result was further validated by a GSH/GSSG ratio assay which showed that TRIM24 over expression induces *de novo* GSH synthesis from glutamate and increases the GSH/GSSG ratio (Figure 31).

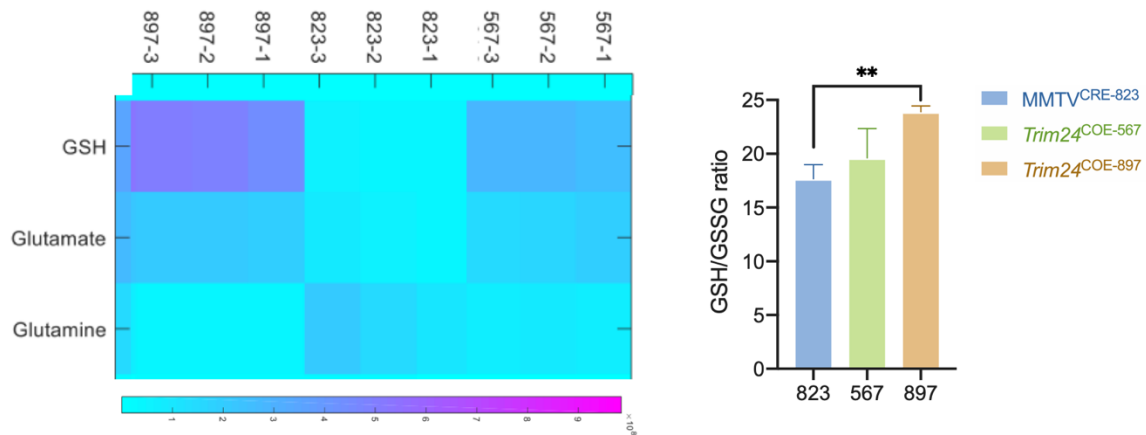


**Figure 31:  $^{15}\text{C}_5$ -glutamine tracing of *Trim24*<sup>COE</sup> spheroids and GSH/GSSG ratio assay revealed increased reduced glutathione level in *Trim24*<sup>COE</sup> spheroids.**

$^{15}\text{C}_5$ -glutamine tracing was performed with triplicate samples. 823-1/2/3 stands for MMTV<sup>CRE-823</sup> spheroid triplicate; 567-1/2/3 stands for *Trim24*<sup>COE-567</sup>; and 897-1/2/3 stands for *Trim24*<sup>COE-897</sup>. Heatmap generated from the tracing data showed *Trim24*<sup>COE-567</sup> and *Trim24*<sup>COE-897</sup> spheroids had a higher abundance of reduced glutathione, glutamate but not glutamine compared to the MMTV<sup>CRE-823</sup> control. Graph on the right showed the result of GSH/GSSG ratio assay which validated the high GSH level in *Trim24*<sup>COE-897</sup> spheroids. (p<0.0001, \*\*\*\*; p<0.001, \*\*\*; p<0.01, \*\*; p<0.05, \*)

We performed western blotting of enzymes in the GSH synthesis and recycling pathways to assess the levels of enzymes involved in GSH synthesis (Figure 32). We found that ASCT2 (SLC1A5), cystine-glutamate antiporter (SLC7A11) glutamine synthase (GluL), glutaminase (GLS1), glutamate dehydrogenase (GluD) and glutathione synthase (GSS) enzyme levels were significantly increased in *Trim24*<sup>COE-897</sup> spheroids but not in *Trim24*<sup>COE-567</sup> spheroids (Figure 4D). The Glutathione reductase (GSR) level was also upregulated in *Trim24*<sup>COE-897</sup> to increase GSH recycling from GSSG. Glutathione transferase (GST) and phosphorylated GST (GSTP) that were also significantly upregulated in *Trim24*<sup>COE-897</sup> but not *Trim24*<sup>COE-567</sup> spheroids (Figure 32).

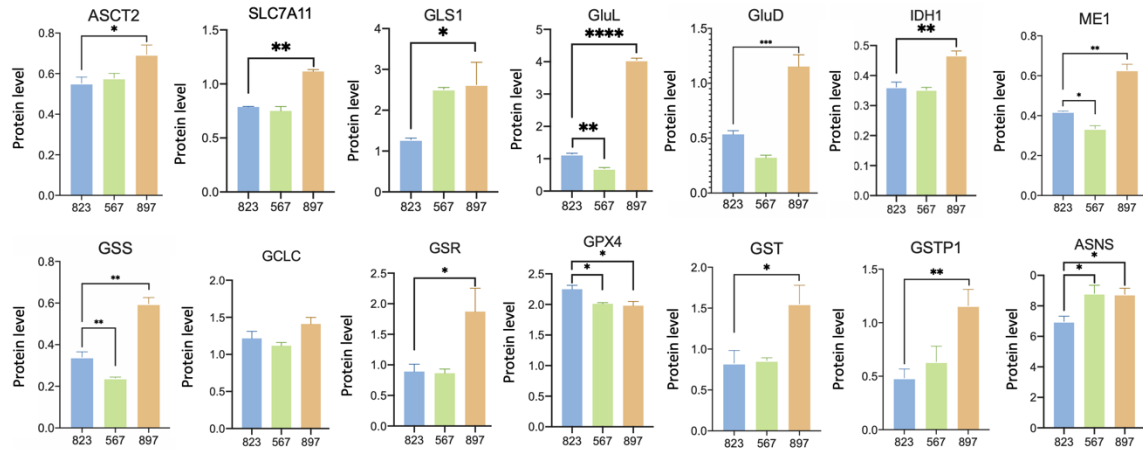


**Figure 32: Western blot quantification of enzyme levels showed increased glutaminolysis pathway and *de novo* GSH synthesis pathway in *Trim24*<sup>COE-897</sup> spheroids.**

Duplicates of each sample were load to run western blot. 823 stands for MMTV<sup>CRE-823</sup> spheroid; 567 stands for *Trim24*<sup>COE-567</sup>; 64 stands for *Trim24*<sup>COE-64</sup>; and 897 stands for *Trim24*<sup>COE-897</sup>. Glutamine transporters (ASCT2, SLC7A11), glutaminolysis-related enzyme (GLS1, ASNS), *de novo* GSH synthesis enzymes (GCLC, GSS) and GSH detoxification enzymes (GST, GSTP), and NADPH-producing enzymes (IDH1, ME1) were upregulated in *Trim24*<sup>COE-897</sup> spheroids. (p<0.0001, \*\*\*\*; p<0.001, \*\*\*; p<0.01, \*\*; p<0.05, \*)



Since the two *Trim24*<sup>COE</sup> spheroid lines were derived from two different endpoint mouse mammary gland tumors driven by TRIM24 over expression, the two spheroid lines exhibited heterogeneity and likely exploited different strategies to increase the cellular GSH pool. Unlike *Trim24*<sup>COE-897</sup>, *Trim24*<sup>COE-567</sup> spheroids showed a slight decrease in GSS expression compared to the MMTV<sup>CRE-823</sup> control. *Trim24*<sup>COE-567</sup> spheroids also exhibited a slight decrease in glutathione peroxidase 4 (GPX4) level, which suggested that *Trim24*<sup>COE-567</sup> spheroids decreased *de novo* glutathione synthesis while preserving the GSH pool. Interestingly, both spheroid lines had upregulated asparagine synthase (ASNS) levels compared to the control. ASNS also facilitates the conversion of glutamine to glutamate, and it has been reported to increase the expression of GluL to sustain *de novo* GSH synthesis [88].

In shTrim24-897 spheroids, enzyme expression of ASCT2, GluL, GLS1, GPX4, GSS, and GST, as well as ASNS, were all downregulated upon TRIM24 knockdown (Figure 33). This result illustrated that TRIM24 over expression drives the upregulation of *de novo* GSH synthesis from glutamate in *Trim24*<sup>COE-897</sup> spheroids.

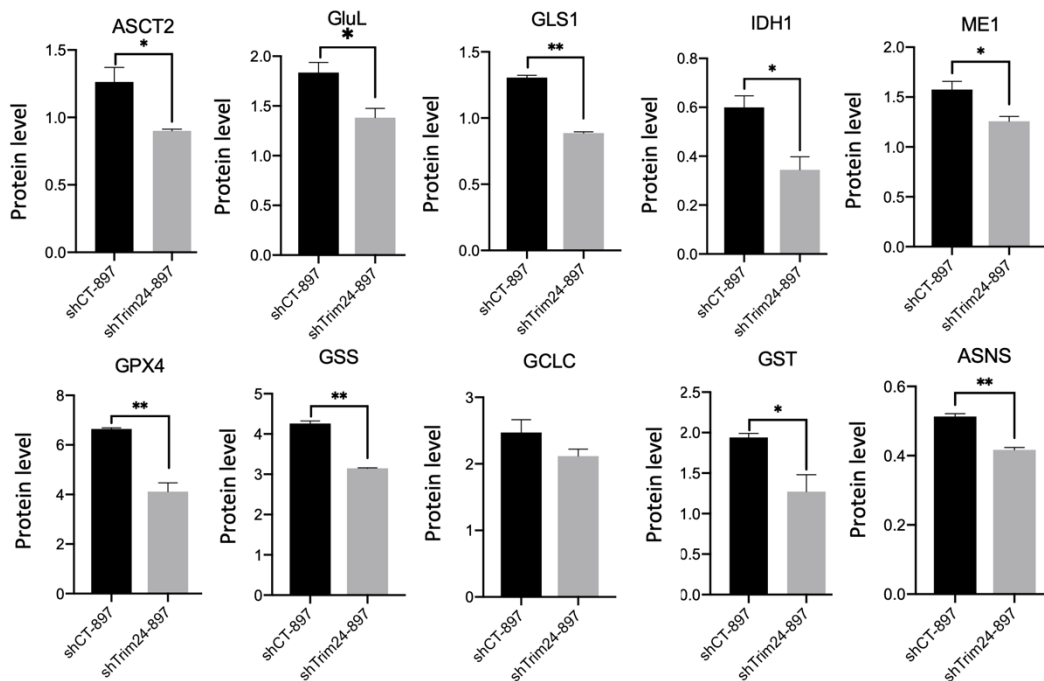


**Figure 33: Western blot quantification showed downregulated enzymes in glutamate metabolism pathway and *de novo* GSH synthesis pathway in shTrim24-897 spheroids**

Glutamine transporters (ASCT2), glutaminolysis-related enzyme (GLS1, ASNS), *de novo* GSH synthesis enzymes (GSS) and GSH detoxification enzymes (GST), and NADPH-producing enzymes (IDH1, ME1) were downregulated upon TRIM24 knock down.

( $p < 0.0001$ , \*\*\*\*;  $p < 0.001$ , \*\*\*;  $p < 0.01$ , \*\*;  $p < 0.05$ , \*)

A previous study showed that GLS1, the critical enzyme that converts glutamine to glutamate, is essential for progression of TNBC [89]. CB-389 is a small molecule inhibitor that targets GLS1 specifically (Figure 34), and it showed antiproliferative effects against a panel of TNBC cell lines grown in 2D [90]. CB839 is a potent glutaminase inhibitor that depletes the substrate for *de novo* GSH synthesis and thus increases intracellular ROS [91].

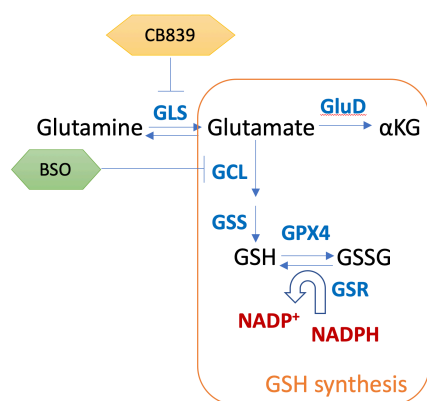


**Figure 34: GLS inhibitor CB839 inhibits the conversion of glutamine to glutamate.**

CB839 is an allosteric inhibitor specifically for GLS1. Upon glutaminase inhibition, CB839 depleted the substrate for *de novo* GSH synthesis.

We found the intracellular and mitochondrial ROS levels were increased in *Trim24*<sup>COE</sup> spheroids after treating with 10 μM CB-839 for 48 hours (Figure 35). *Trim24*<sup>COE-567</sup> showed a slight decrease in its viability while *Trim24*<sup>COE-897</sup> spheroids showed a 30% decrease in response to CB-839 treatment (Figure 36). When the drug was combined with TRIM24 knockdown, spheroid viability showed an approximately 50% decrease in the shTrim24-897 line (Figure 36). TRIM24 over expression led to increased levels of GLS1, and it is possible that *Trim24*<sup>COE</sup> spheroids develop addiction to GLS1 downstream metabolite glutamate. TRIM24 knockdown decreased the GLS1 expression, thus sensitizing the cells to further pharmacological inhibition of GLS1 by CB839.

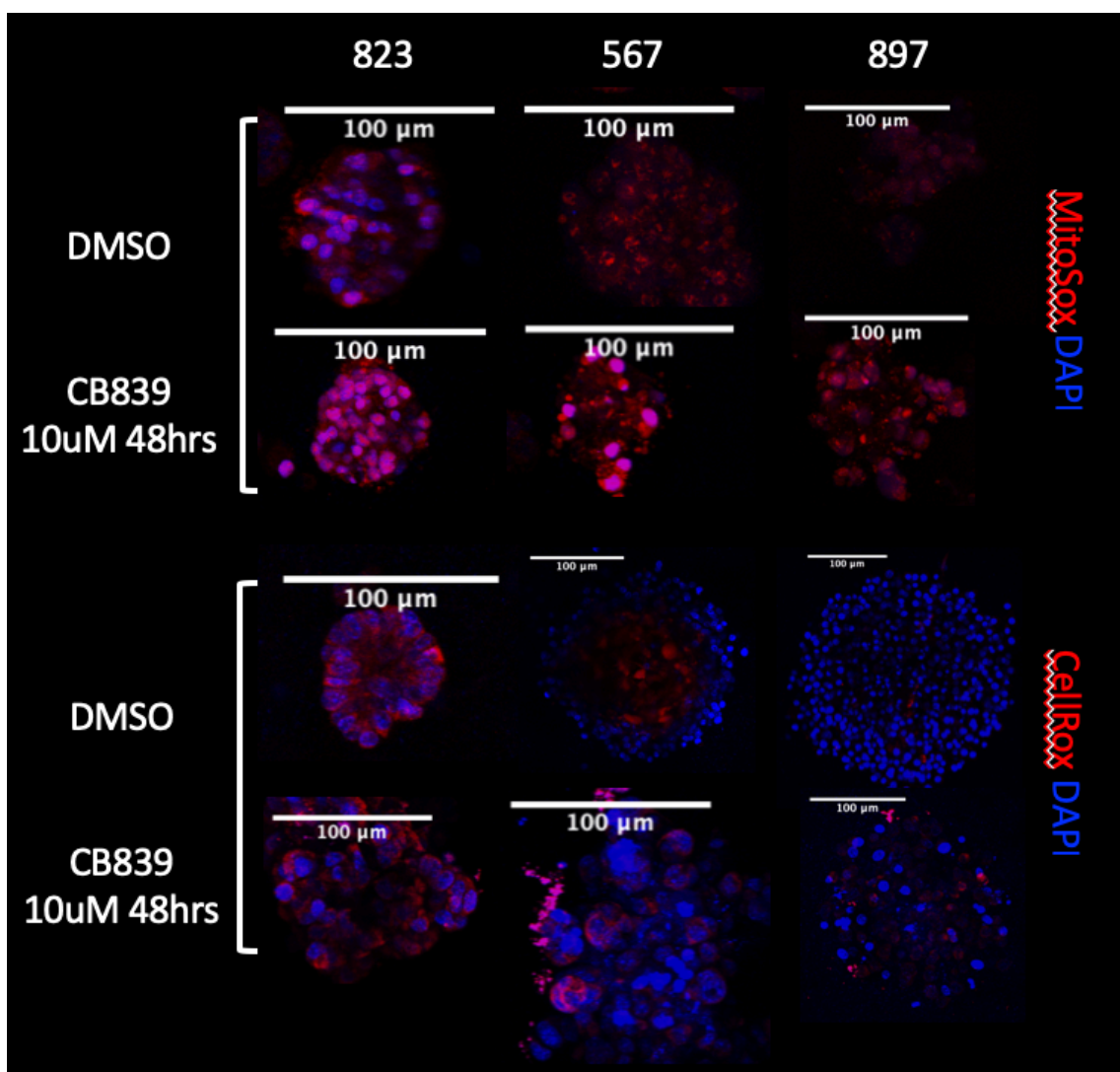


**Figure 35: CB839 treatment for 48 hours increased intracellular and mitochondrial ROS levels in *Trim24*<sup>COE</sup> spheroids.**

Both MitoSOX Orange (upper panel) and CellROX Orange (lower panel) signals were increased in *Trim24*<sup>COE-567</sup> spheroids and *Trim24*<sup>COE-897</sup> spheroids upon GLS1 inhibitor CB839 treatment.

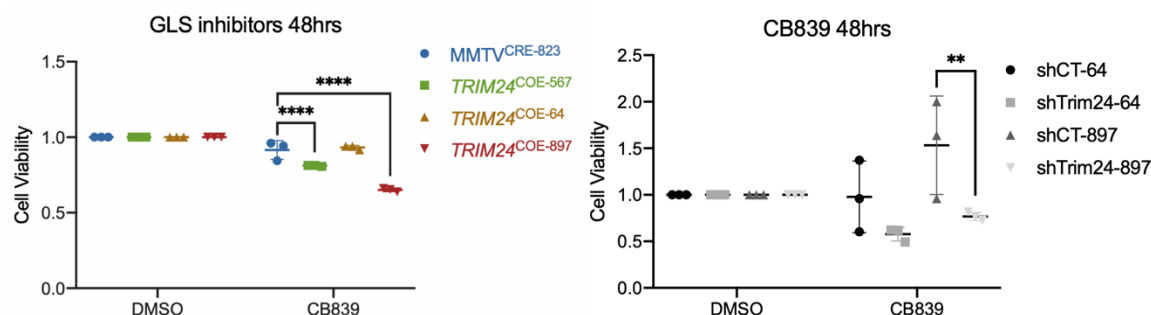


**Figure 36: Viability of *Trim24*<sup>COE</sup> spheroids was decreased after 48-hours CB839 treatment; the drug effect was enhanced by TRIM24 knock down.**

CTG luminescence was measured and CB839-treated samples were normalized against DMSO-treated control samples. Triplicates were used for CellTitor-Glo viability assay. With 10  $\mu$ M of CB839, both *Trim24*<sup>COE-567</sup> and *Trim24*<sup>COE-897</sup> spheroid showed significant decrease in their viability; viability of shTrim24-897 was greatly decreased upon CB839 treatment compared to the control. ( $p < 0.0001$ , \*\*\*\*;  $p < 0.001$ , \*\*\*;  $p < 0.01$ , \*\*;  $p < 0.05$ , \*)

To investigate how CB-839 affects the NADP(H) pool and NADP<sup>+</sup>/NADPH ratio, we performed a total NADPH assay and NADP<sup>+</sup>/NADPH ratio assay. The results revealed that the total NADPH level is decreased in the *Trim24*<sup>COE-567</sup> spheroids as well as the NADP<sup>+</sup>/NADPH ratio. Total NADPH levels were increased in control and *Trim24*<sup>COE-897</sup> spheroids and the increase was contributed by upregulated NADP<sup>+</sup> responding to GLS1 inhibition (Figure 37). The increased level of NADP<sup>+</sup> was likely a result of increased GSH recycling by GSR in *Trim24*<sup>COE-897</sup> spheroids. In shTrim24-897, GLS1 inhibitors CB-839 decreased the total NADP(H) level compared to the shCT-897 control.

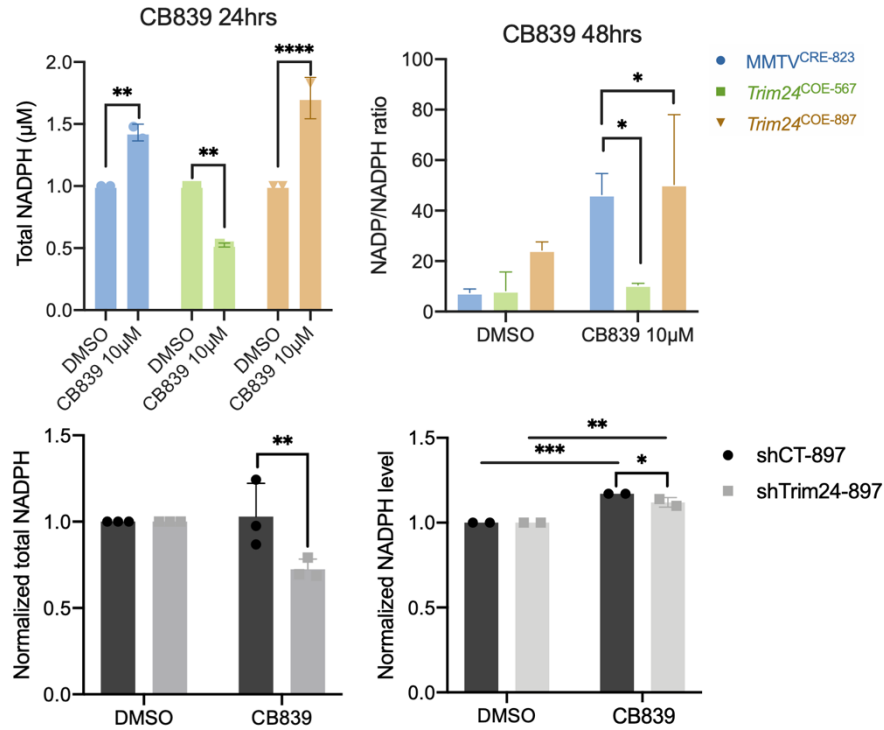


**Figure 37: Total NADP(H) and NADP<sup>+</sup>/NADPH ratio assay of *Trim24*<sup>COE</sup> spheroids, showed increased NADP<sup>+</sup> abundance after CB839 treatment.**

Total NADP(H) and reduced NADPH were determined with a standard curve and CB839-treated samples were normalized to DMSO-treated control samples. Triplicates were used for both assays. The total NADPH level increased after treated with CB839 in both MMTV<sup>Cre-823</sup> and *Trim24*<sup>COE-897</sup> spheroids. In NADP/NADPH ratio assay, *Trim24*<sup>COE-897</sup> spheroids had significantly higher NADP/NADPH ratio than MMTV<sup>Cre-823</sup> which indicated upregulated GSH recycling to replenish GSH pool after GLS inhibition.

(p<0.0001, \*\*\*\*; p<0.001, \*\*\*; p<0.01, \*\*; p<0.05, \*)

A more straightforward way to inhibit *de novo* GHS synthesis is by using an irreversible inhibitor of GCL, such as Buthionine sulfoximine (BSO) [92]. By targeting the enzyme that catalyzes the first and rate-limiting step of *de novo* GSH synthesis (Figure 34), BSO was reported to promote ROS accumulation and induce apoptotic cell death [93], as well as ferroptosis in a panel of established cancer cell lines grown as 2D-cultures [92].

In the context of TRIM24 over expression, 24-hour treatment of BSO was not effective in reducing spheroid viability (Figure 38). In shTrim24-897 spheroids, viability was significantly decreased with 20  $\mu$ M to 200  $\mu$ M BSO treatment for 24hrs, compared to shCT-897. TRIM24 knockdown sensitizes the cells to BSO treatment and induces more cell death compared to the shCT-897. The total NADPH level was not altered by BSO treatment in either *Trim24*<sup>COE-897</sup> or shTrim24-897 spheroids (Figure 39).

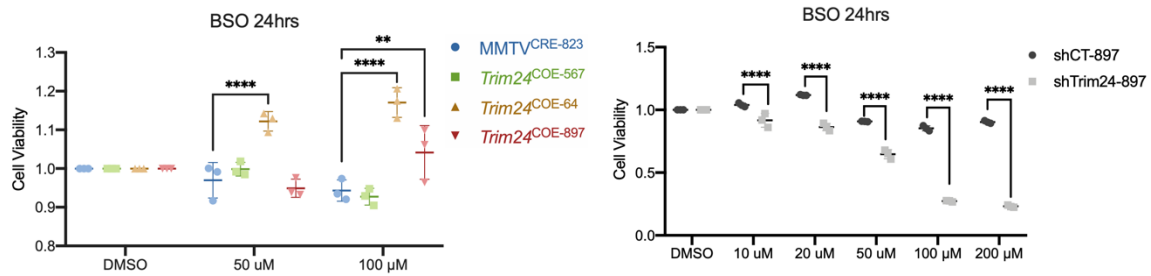


**Figure 38: CTG viability assay showed BSO treatment had additive effect with TRIM24 knock down.**

CTG luminescence was measured and BSO-treated samples were normalized against DMSO-treated control samples. BSO alone did not affect the viability of *Trim24*<sup>COE</sup> spheroids; however, spheroid viability drastically decreased upon TRIM24 knock down.

( $p < 0.0001$ , \*\*\*\*;  $p < 0.001$ , \*\*\*;  $p < 0.01$ , \*\*;  $p < 0.05$ , \*)

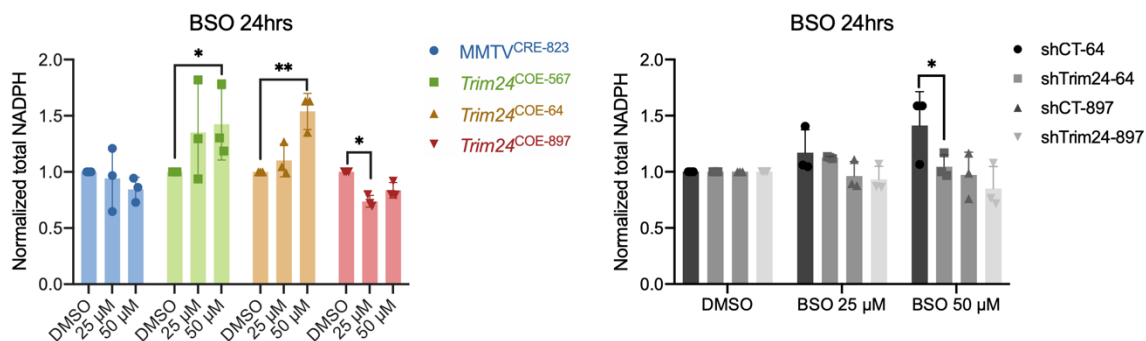


**Figure 39: Total NADP(H) levels were increased in *Trim24*<sup>COE-567</sup> and *Trim24*<sup>COE-64</sup> spheroids but not *Trim24*<sup>COE-897</sup> spheroids.**

Total NADP(H) levels were determined relative to a standard curve and BSO-treated samples were normalized to DMSO-treated control samples. Triplicates were used for both assays. (p<0.0001, \*\*\*\*; p<0.001, \*\*\*; p<0.01, \*\*; p<0.05, \*)

Since CB-839 and BSO both inhibit the GSH synthesis pathway, combining them with a GLS inhibitor upstream of a GCL inhibitor that directly targets the enzyme may enhance inhibitory effects on the viability of *Trim24*<sup>COE</sup> spheroids. A significant decrease in viability was observed in all three *Trim24*<sup>COE</sup> lines, as well as the MMTV<sup>CRE-823</sup> control, with the combined treatment, compared to BSO treatment alone (Figure 40). In the context of TRIM24 knockdown, combined treatment did not exhibit a greater effect than CB-839 alone or BSO alone in shCT-897 or shTrim24-897 spheroids. With combined drug treatment, the shTrim24-897 line also showed significantly decreased viability comparing to the shCT-897 line which meant TRIM24 knockdown sensitized the spheroids to the combined drug treatment (Figure 40).



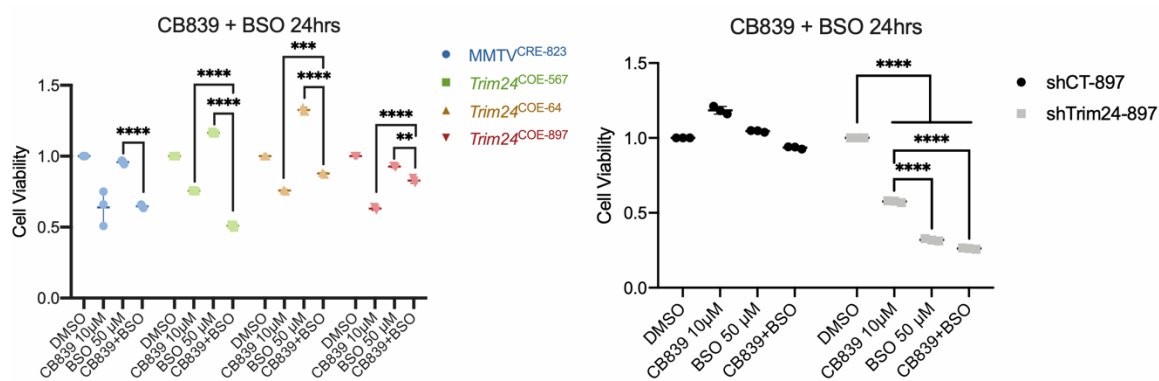


**Figure 40: CTG viability assay showed different responses to combined GSH synthesis inhibitor treatment in *Trim24*<sup>COE</sup> spheroids, shCT-897 and shTrim24-897.**

CTG luminescence was measured and CB839 and BSO-treated samples were normalized against DMSO-treated control samples, triplicates were used. CB839 and BSO combined treatment showed greater effect than these drugs alone in *Trim24*<sup>COE-567</sup>. Combined treatment did not work in shCT or shTrim24 spheroids. (p<0.0001, \*\*\*\*; p<0.001, \*\*\*; p<0.01, \*\*; p<0.05, \*)

## **TRIM24 over expression upregulates reducing power through increased NRF2 activity**

The Keap1-NRF2 pathway is the master regulator of cytoprotective defense under oxidative stress. Under normal physiological conditions, Kelch-like ECH-associated protein 1 (KEAP1) binds to nuclear factor erythroid2-related factor (NRF2) and promotes NRF2 degradation by Cullin 3 (CUL3) mediated-polyubiquitination [94, 95]. When ROS levels increase, KEAP1 oxidation leads to a conformational change of KEAP1, leading to release of NRF2. NRF2 then enters the nucleus, binds Maf and initiates transcription via interaction with antioxidant response elements (AREs) of target genes, such as *Nox1*, *Gcl*, and *Gst* [95]. This is a cytoprotective response to maintain homeostasis, oppose cellular damage and suppress tumor promotion. During tumorigenesis, DNA damage accumulates and leads to constitutive NRF2 nuclear translocation. NRF2-activated transcription of ARE element-regulated genes increases expression of *G6PD*, *PGD*, *TALDO1*, *MTHFD2*, *GCL*, *GSS*, *GSR* and *ME1* to enhance cryoprotection [86]. This provides advantages for cancer cells to endure high endogenous ROS and escape ROS-induced apoptosis. Therefore, NRF2 hyperactivity favors cancer cell survival, which can lead to resistance to chemotherapy [96-98]. Subsequent metabolic pathways regulated by NRF2 (GSH synthesis and recycling, NADPH regulation, antioxidant detoxification) will also enhance antioxidant defenses and promote cellular proliferation [8].

Extracellular H<sub>2</sub>O<sub>2</sub> addition is known to promote NRF2 translocation to the nucleus and activate ARE element-regulated transcription [99] [100]. To investigate if survival of *Trim24*<sup>COE</sup> spheroids under ROS stress depends on NRF2 activation, we first treated the spheroids with extracellular H<sub>2</sub>O<sub>2</sub> and found TRIM24 over expression increased resistance to H<sub>2</sub>O<sub>2</sub>. After 24-hours of 1 mM H<sub>2</sub>O<sub>2</sub> treatment, cell viability of control MMTV<sup>Cre-823</sup> spheroids was drastically decreased (Figure 41). In contrast, the viability of *Trim24*<sup>COE-567</sup> spheroids was not affected; and there was only about a 30% decrease of viability in the *Trim24*<sup>COE-897</sup> spheroids. When the dose of H<sub>2</sub>O<sub>2</sub> was increased to 2mM, both MMTV<sup>Cre-823</sup>

and *Trim24*<sup>COE-897</sup> spheroids exhibited very low or zero viability, while *Trim24*<sup>COE-567</sup> was still resistant to the high dose oxidative stress. In both shTrim24-64 and shTrim24-897, after 24 hours of 1 mM and 2 mM H<sub>2</sub>O<sub>2</sub> treatment, cell viability was significantly decreased compared to their sh-Controls (Figure 41). This finding indicates that TRIM24-knockdown sensitizes the cells to reactive oxygen species H<sub>2</sub>O<sub>2</sub>.

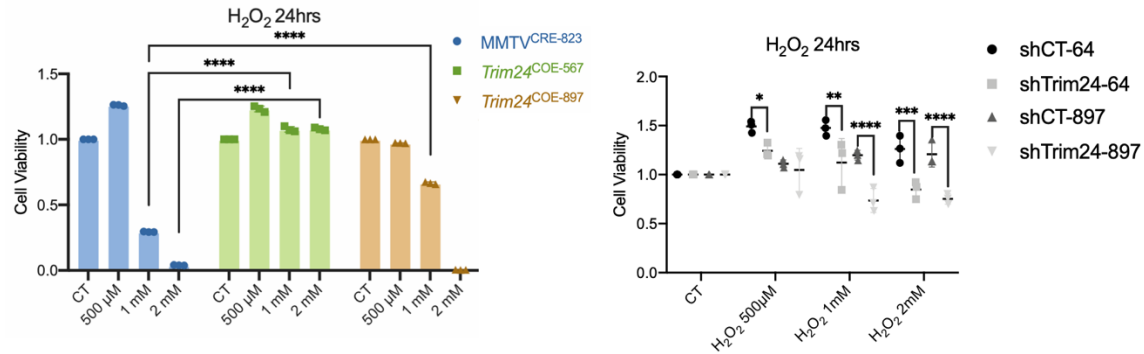


**Figure 41: CTG viability assay showed resistance to H<sub>2</sub>O<sub>2</sub> was TRIM24 dependent.**

CTG luminescence was measured and H<sub>2</sub>O<sub>2</sub> samples were normalized against DMSO-treated control samples. After 24-hours of 1mM H<sub>2</sub>O<sub>2</sub> treatment, spheroids with high TRIM24 levels (*Trim24*<sup>COE</sup>, shCT spheroids) showed resistance to H<sub>2</sub>O<sub>2</sub> treatment while spheroids with relatively lower TRIM24 levels (MMTV<sup>Cre-823</sup>, shTrim24 spheroids) showed significant decreased in viability upon 1mM H<sub>2</sub>O<sub>2</sub> treatment. (p<0.0001, \*\*\*\*, p<0.001, \*\*\*, p<0.01, \*\*, p<0.05, \*)

After 24 hours of 1 mM H<sub>2</sub>O<sub>2</sub> treatment, the total NADP(H) level was not significantly altered in the *Trim24*<sup>COE</sup> spheroids. However, the reduced NADPH abundance in *Trim24*<sup>COE-897</sup> spheroids was significantly decreased in response to 1 mM H<sub>2</sub>O<sub>2</sub>, indicating more NADPH was converted to NADP<sup>+</sup> by the spheroids to buffer oxidative stress (Figure 42). The shCT-897 line showed a moderate increase in total NADP(H) level while the shTrim24-897 spheroids failed to increase total NADP(H) level in response to H<sub>2</sub>O<sub>2</sub>. Similar to its parental line, shCT-897 spheroids had a decrease in reduced NADPH

abundance after 500  $\mu$ M and 1 mM  $\text{H}_2\text{O}_2$  treatment, and knocking down TRIM24 impairs the ability to utilize NADPH (Figure 42). Together, this result indicated that knocking down TRIM24 impaired the spheroids' adaptation to oxidative stress, failed to increase the total NADP(H) pool and utilize reduced NADPH as a part of an antioxidant defense in shTrim24-897.

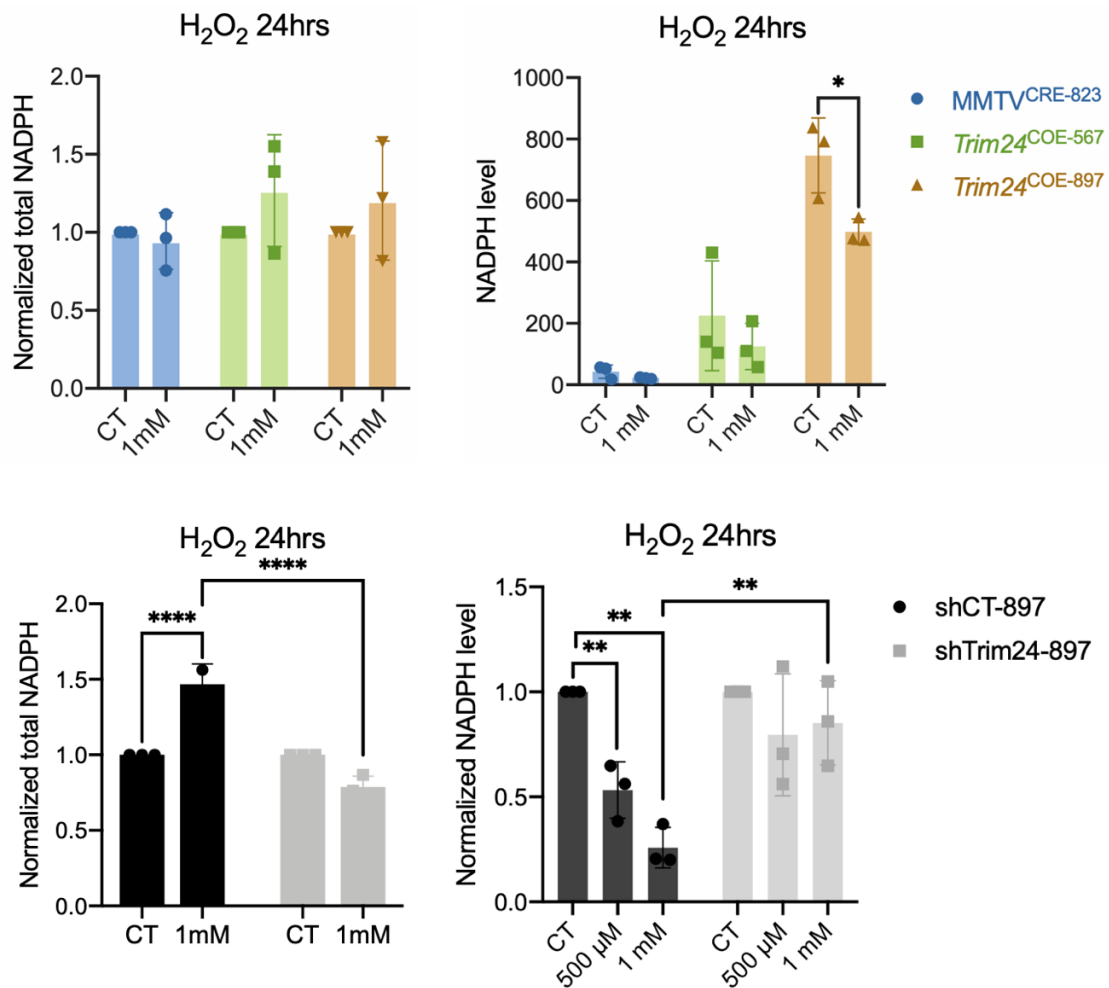


**Figure 42: Usage of reduced NADPH in response to  $\text{H}_2\text{O}_2$  treatment was impaired by TRIM24 knock down.**

Total NADP(H) and reduced NADPH were determined with a standard curve and 1 mM  $\text{H}_2\text{O}_2$ -treated samples were normalized to non-treated control samples. CT stands for non-treated negative control samples. ( $p < 0.0001$ , \*\*\*\*;  $p < 0.001$ , \*\*\*;  $p < 0.01$ , \*\*;  $p < 0.05$ , \*)

In previous results, we showed that *Trim24*<sup>COE</sup> spheroids increase antioxidant defense by upregulating NADP(H) production and *de novo* synthesis of GSH. Since *Trim24*<sup>COE</sup> spheroids exhibited high resistance to H<sub>2</sub>O<sub>2</sub>, which also activates an NRF2-mediated antioxidant response, I hypothesized that NRF2 is potential mediator between TRIM24 over expression and the upregulation of downstream pathways. We first assessed mRNA levels of Nrf2 and its known target genes by qRT-PCR. In the non-treated condition, *Trim24*<sup>COE-897</sup> spheroids had an approximately two-fold increase in *Me1*, *Phgdh*, *Mthfd2*, *Nampt*, and *Gclc* expression, compared to the MMTV<sup>Cre-823</sup> control (Figure 43). Of note, in spite of an upregulated TRIM24 protein level, *Trim24* mRNA was not overexpressed, compared to control levels, in *Trim24*<sup>COE-567</sup> or *Trim24*<sup>COE-897</sup> at this time point (day 4 of spheroid culture). After 24hrs 1mM H<sub>2</sub>O<sub>2</sub> treatment, both *Trim24*<sup>COE</sup> lines showed drastically increased *Nrf2* expression. *Trim24*<sup>COE-567</sup> also had significantly increased expression of NADPH dehydrogenase (*Nqo1*); *Pgd* in the PPP shunt; *Me1* in the TCA cycle; *Shmt1*, *Shmt2*, *Mthfd2* in the one-carbon metabolism; *Slc7A11*, *Asns*, *Gclc*, *Gclm*, *Gss*, *Gpx4*, and *Gspt* in the GSH synthesis and detoxification pathway. While slightly different from the response of *Trim24*<sup>COE-567</sup> to H<sub>2</sub>O<sub>2</sub>, *Trim24*<sup>COE-897</sup> had upregulated expression of *G6pd* and *Pgd* in the PPP pathway; *Slc7a11*, *Asns*, *Gclm*, *Gpx4*, and *Gsr* in the GSH synthesis and recycling pathway (Figure 43). The increase in *Nrf2* as well as Nrf2-targeted gene expression likely underpins the resistance to H<sub>2</sub>O<sub>2</sub> treatment in *Trim24*<sup>COE</sup> spheroids.

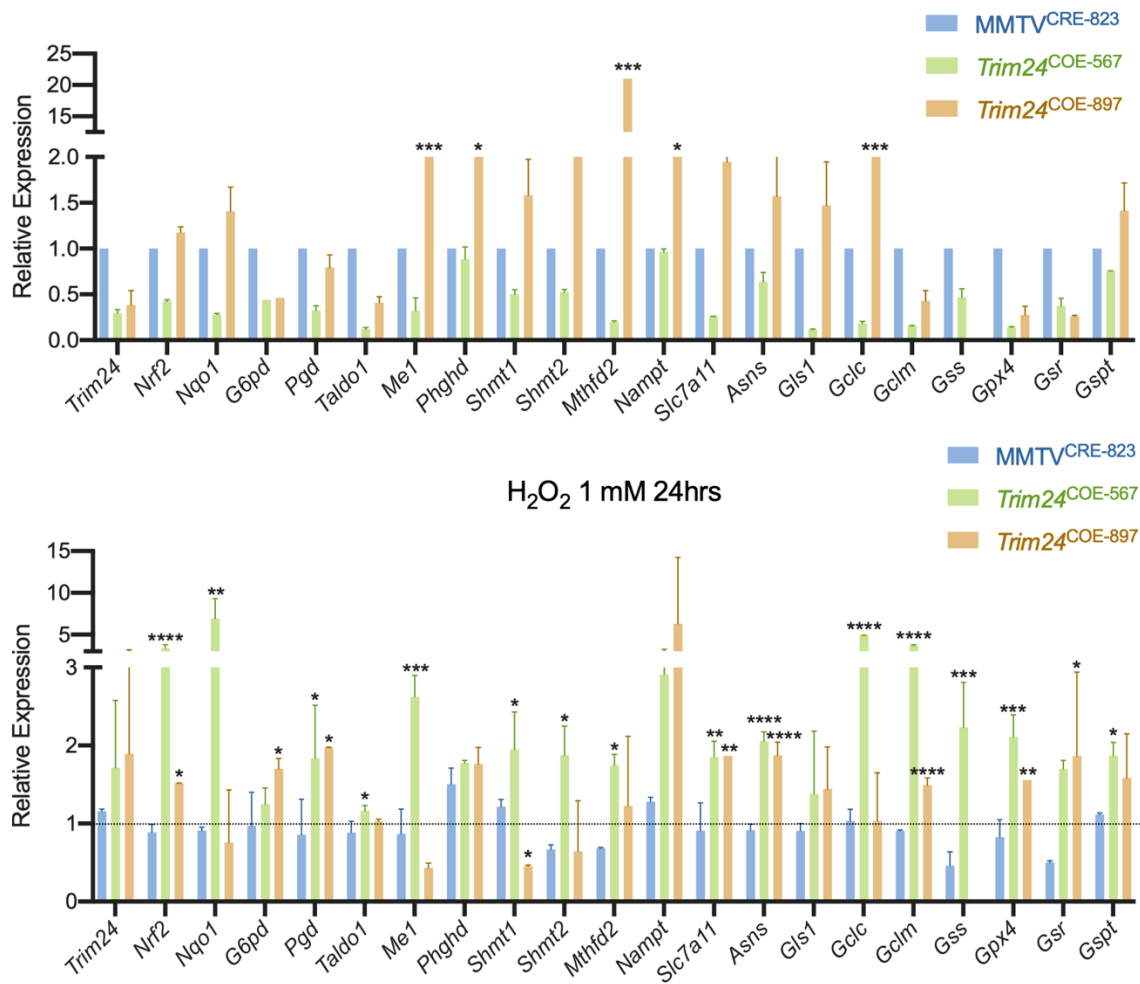


**Figure 43: Nrf2 and its target genes mRNA expression in *Trim24*<sup>COE</sup> spheroids was induced by 24-hour 1mM H<sub>2</sub>O<sub>2</sub> treatment.**

qRT-PCR data of non-treated *Trim24*<sup>COE</sup> spheroids were normalized with ribosomal gene 18S, then normalized against MMTV<sup>Cre-823</sup>. H<sub>2</sub>O<sub>2</sub>-treated samples were first normalized with 18S then normalized against non-treated control samples. After 1mM H<sub>2</sub>O<sub>2</sub> treatment, Nrf2-target genes in 1C metabolism, glutaminolysis and GSH synthesis pathway were significantly increased. (p<0.0001, \*\*\*\*; p<0.001, \*\*\*; p<0.01, \*\*; p<0.05, \*)

The expression of these genes is also Trim24-dependent— knocking down Trim24 in shTrim24-897 spheroids resulted in a more than 50% decrease in *Nrf2* and NRF2 targeted gene expression in the PPP shunt and one-carbon metabolism, as well as the GSH synthesis pathway (Figure 44). *Trim24* and *Nrf2* expression was induced by 500 mM

and 1mM H<sub>2</sub>O<sub>2</sub> treatment in shTrim24-897 spheroids. With high expression of *Nrf2* in response to H<sub>2</sub>O<sub>2</sub>, target genes in the downstream NADPH and GSH producing pathways were all upregulated in response (Figure 44).

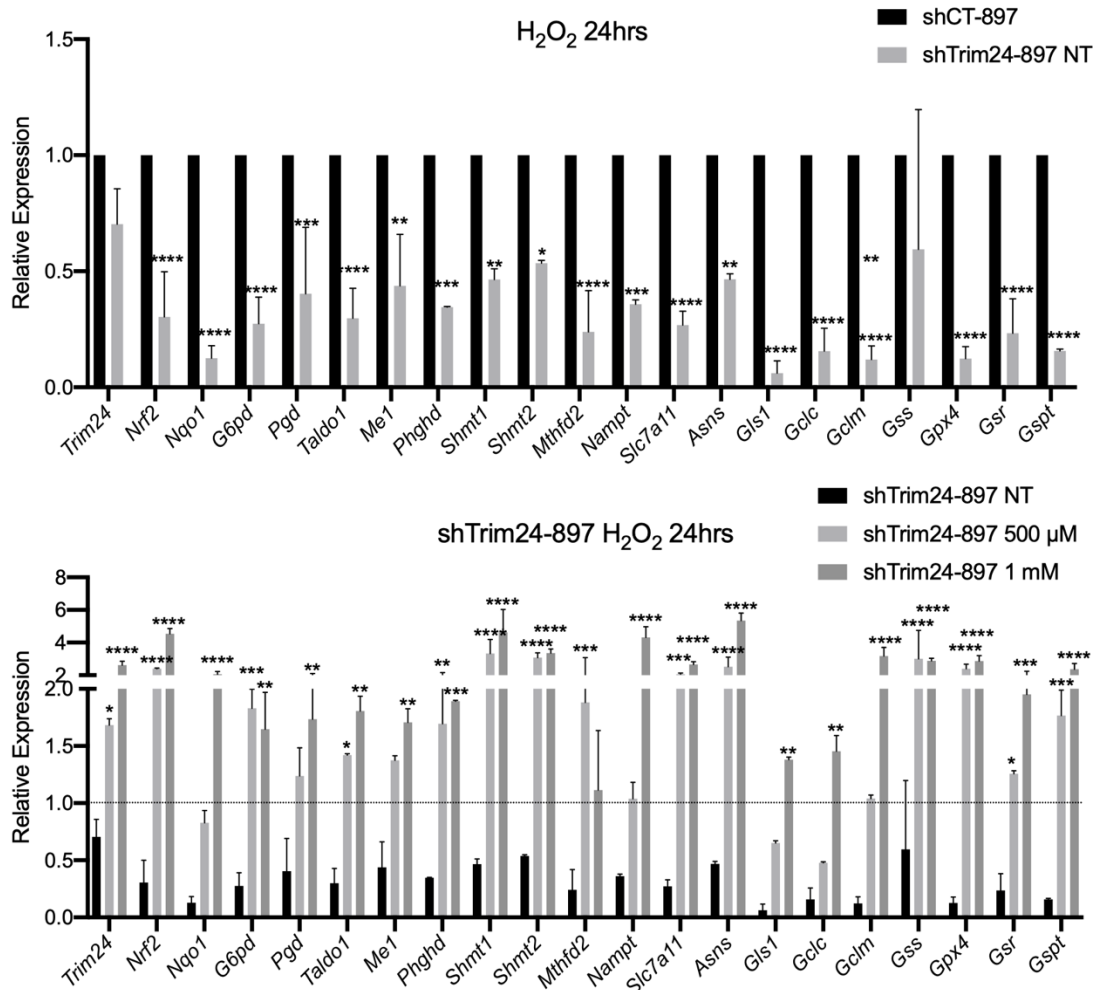


**Figure 44: *Nrf2* and its target gene mRNA expression was decreased upon Trim24 knock down but induced after 24-hour 1mM H<sub>2</sub>O<sub>2</sub> treatment in shTrim24-897.**

qRT-PCR data of non-treated shCT-897 and shTrim24-897 spheroids were normalized with house-keeping gene 18S, then normalized against shCT-897. H<sub>2</sub>O<sub>2</sub>-treated samples were first normalized with 18S then normalized against non-treated control samples. Upon Trim24 knock down, *Nrf2*-target genes in 1C metabolism, glutaminolysis and GSH synthesis pathway were significantly decreased compared to the shCT-897. *Nrf2*-target

gene expression was induced in shTrim24-897 compared to the shCT-897 after 1mM H<sub>2</sub>O<sub>2</sub> treatment. (p<0.0001, \*\*\*\*; p<0.001, \*\*\*; p<0.01, \*\*; p<0.05, \*)

To complement RNA assessments, I determined NRF2 protein levels. *Trim24*<sup>COE-567</sup> and *Trim24*<sup>COE-897</sup> exhibited increased expression of NRF2 protein level compared to MMTV<sup>CRE-823</sup> while knocking down TRIM24 decreased NRF2 expression in shTrim24-897 (Figure 44). After treatment with 1 mM of H<sub>2</sub>O<sub>2</sub>, NRF2 protein levels as well as GCL1, GCLC, PHGDH were slightly upregulated in *Trim24*<sup>COE-897</sup> (Figure 45). With 500  $\mu$ M and 1 mM of H<sub>2</sub>O<sub>2</sub> for 24 hours, shCT-897 responded with a significantly higher NRF2 expression while shTrim24-897 failed to increase the NRF2 level (Figure 47). In contrast to the *Trim24* mRNA level, H<sub>2</sub>O<sub>2</sub> treatment for 24 hours did not affect the TRIM24 protein levels in shCT or shTrim24-897 lines. PHGDH, the enzyme that leads glycolysis metabolite 3PG to one-carbon metabolism, was also upregulated by H<sub>2</sub>O<sub>2</sub> in shCT-897. PHGDH protein level was increased in shTrim24-897, as well, but still significantly lower compared to shCT-897. Similarly, GCLC and GLS1 also failed to increase in response to H<sub>2</sub>O<sub>2</sub> upon TRIM24 knockdown. Taken together, TRIM24 regulates *Nrf2* expression, NRF2 protein level as well NRF2 downstream enzyme levels; knocking down TRIM24 results in downregulated NRF2 level as well as NRF2 target enzyme levels.



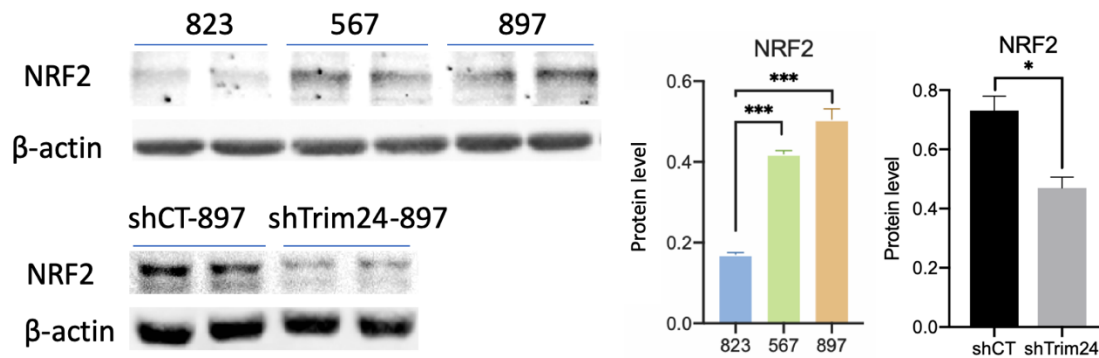


**Figure 45: Western blots and their quantification of NRF2 showed TRIM24-dependent NRF2 protein level.**

Duplicates of each sample were load to run this western blot. 823 stands for MMTV<sup>CRE-823</sup> spheroid; 567 stands for *Trim24*<sup>COE-567</sup>; 64 stands for *Trim24*<sup>COE-64</sup>; and 897 stands for *Trim24*<sup>COE-897</sup>. (p<0.0001, \*\*\*\*; p<0.001, \*\*\*; p<0.01, \*\*; p<0.05, \*)

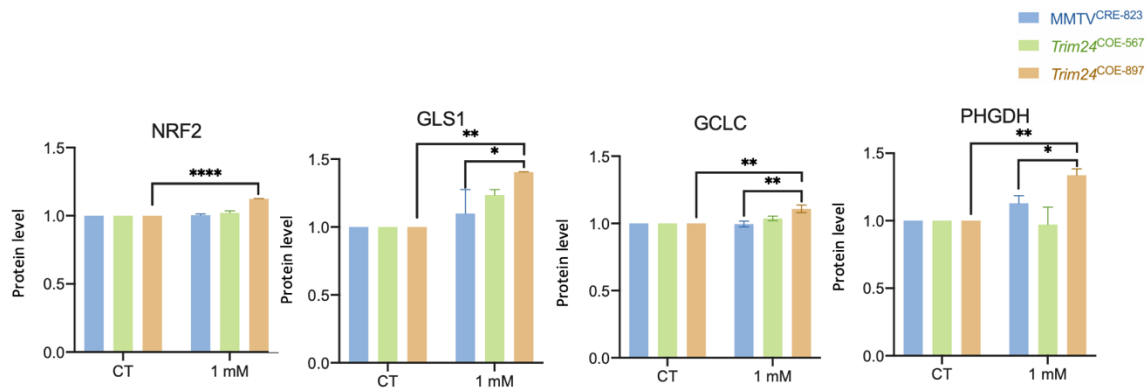


**Figure 46: Western blot quantification showed NRF2 downstream pathway enzyme levels were increased in *Trim24*<sup>COE</sup> spheroids after 24-hour 1mM H<sub>2</sub>O<sub>2</sub>.**

H<sub>2</sub>O<sub>2</sub>-treated samples were first normalized with beta-actin then normalized against non-treated control samples (CT). (p<0.0001, \*\*\*\*; p<0.001, \*\*\*; p<0.01, \*\*; p<0.05, \*)

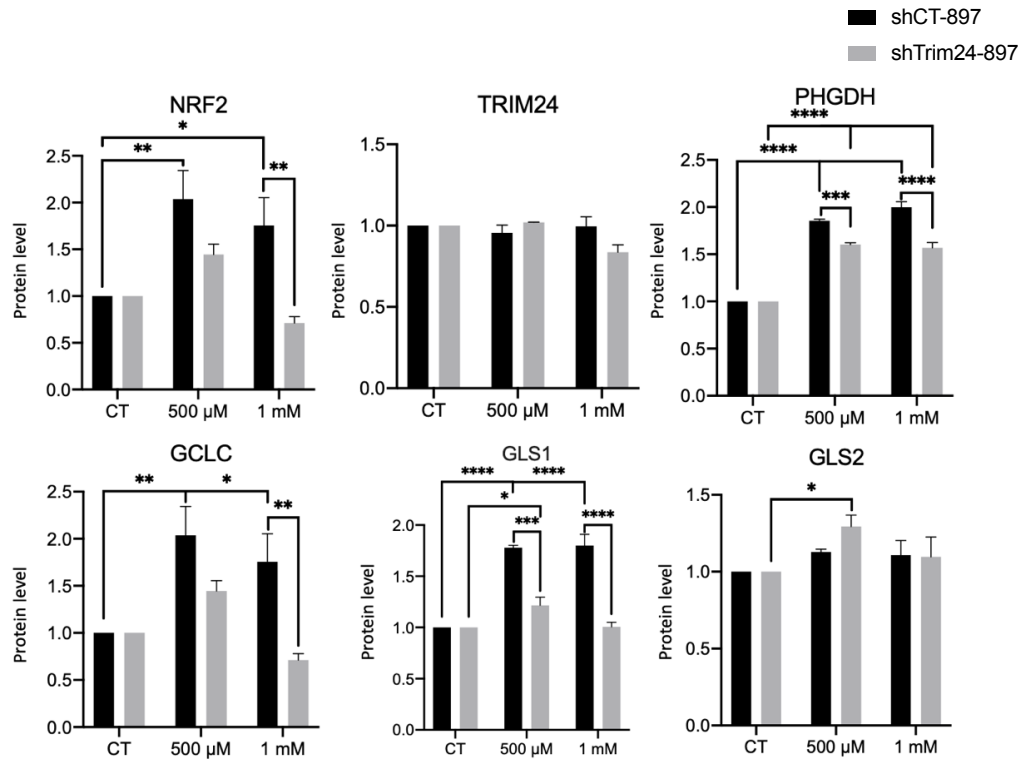


**Figure 47: Western blot quantification showed NRF2 downstream pathway enzyme levels were downregulated in shTrim24-897 spheroids compared to shCT-897 after 24-hour 1mM H<sub>2</sub>O<sub>2</sub>.**

H<sub>2</sub>O<sub>2</sub>-treated samples were first normalized with beta-actin then normalized against non-treated control samples (CT). (p<0.0001, \*\*\*\*; p<0.001, \*\*\*; p<0.01, \*\*; p<0.05, \*)

## Discussion

ROS is a double-edged sword in cancer biology, acting in both tumor suppression and tumor progression. It has been widely reported that intracellular and extracellular ROS promote cell proliferation and migration [101-104]. Administration of mitochondrial ROS scavengers to lower ROS level has been shown to block lung metastasis from MDA-MB231 human breast cancer cells [105]. In contrast, increasing ROS level is also an anticancer response to ionizing radiation and chemotherapy [106, 107].

The dynamic and complex interplay between ROS abundance and cancer is primarily based on the delicate balance between ROS production and scavenging. ROS generation, signaling and regulation are highly orchestrated processes which are rewired in cancer cells to benefit proliferation, invasion and epigenetic alterations that lead to tumor progression [14]. Numerous studies show that cancer cells exhibit persistently high ROS level due to their rapid growth, limited nutrients and oxygen availability, as well as stimuli from the tumor microenvironment [104, 108-110]. To compensate oxidative stress, cancer cells develop higher antioxidant capacity than their normal counterparts to preserve essential biological functions. Here in this study, we present that TRIM24 overexpression upregulates antioxidant defenses through NRF2; knocking down TRIM24 downregulates *Nrf2* expression and dampens cellular adaption to oxidative stress, thus further sensitizing spheroids to metabolic inhibitors that target NAPHD or GSH production.

Breast cancer cells bear higher ROS level compared to non-transformed cells, due to mitochondrial dysfunction [111]. Mitochondrial activities were indeed impaired in *Trim24*<sup>COE</sup> spheroids compared to the MMTV<sup>Cre</sup> control; however, MitoSox staining showed that mitochondrial ROS levels were lower instead of higher in *Trim24*<sup>COE</sup> spheroids. A recent study comparing redox balance across BC cell lines showed that extracellular H<sub>2</sub>O<sub>2</sub> treatment only increased ROS in the nontransformed MCF10A cell line; whereas, TNBC cell lines (BT549, MDA-MB-486 and MDA-MB-231) exhibited a greater

capacity to balance oxidative stress [112]. In accordance with this published work, *Trim24*<sup>COE</sup> spheroids also showed resistance to high-dose H<sub>2</sub>O<sub>2</sub> treatment. However, in contrast to 2D-cultured TNBC cell lines, baseline ROS levels in *Trim24*<sup>COE</sup> spheroids were lower than the MMTV<sup>Cre</sup> control which indicated a lower oxidant status. CellRox staining revealed that 24 hours of H<sub>2</sub>O<sub>2</sub> treatment visibly increased ROS levels in MMTV<sup>Cre</sup> control but not in *Trim24*<sup>COE</sup> spheroids, which remained low. Knocking down TRIM24 in shTrim24-897 spheroids increases the intracellular ROS level, which suggests TRIM24-dependent ROS scavenging.

Glycolysis was the first metabolic pathway studied in cancer and lactate dehydrogenase-A (LDH-A) was the first enzyme identified as a target of oncogene c-Myc [113]. Since then, extensive investigations found that aerobic glycolysis in cancer cells results from aberrant activation of oncogenes *Kras*, *c-Myc* and the PI3K-Akt-mTOR pathway [53, 114-116]. Other than a bioenergetic effect, a major advantage of high-rate glycolysis is an increased availability of anabolic pathway precursors [12]. Previous work in our lab and by others have shown that TRIM24 exploits glucose metabolism to promote malignant transformation [32, 117]. *Trim24*<sup>COE</sup> spheroids exhibited high glycolysis flux and an especially high abundance of 3PG/2PG, indicating increased diversion from glycolysis to 1C metabolism. It has been reported that the 1C pathway is particularly upregulated in MDA-MB231 metastatic subclones [118]. The expression of mitochondrial 1C pathway enzymes SHMT2 and MTHFD is also induced in breast cancer [77, 119]. *Trim24*<sup>COE-897</sup> but not *Trim24*<sup>COE-567</sup> spheroids had significantly upregulated 1C metabolism enzymes SHMT1/2 and MTHFD1; the diversion from glycolysis to the 1C pathway is also dependent on TRIM24 over expression in *Trim24*<sup>COE-897</sup>. Inhibition of this diversion decreased the viability of *Trim24*<sup>COE</sup> and subsequently decreased the NADPH level; knocking-down TRIM24 induces cell death and cannot be rescued by 3PG supplement.

Glutamate synthesis was upregulated in both *Trim24*<sup>COE</sup> lines while *de novo* glutathione synthesis was only regulated in *Trim24*<sup>COE-897</sup> spheroids. This indicated the

divergent utilization of glutamate in the two *Trim24*<sup>COE</sup> lines, the high abundance of glutamate in *Trim24*<sup>COE-567</sup> spheroids might be used for non-essential amino acid synthesis other than generating GSH [120]. Inhibition of glutaminolysis with CB839, but not direct inhibition of GSH synthesis with BSO, induced cell death in both *Trim24*<sup>COE</sup> lines. Reduced GSH consequently pushed the cells to compensate with increased GSH recycling, thus increasing the NADP<sup>+</sup>/NADPH ratio in *Trim24*<sup>COE-897</sup>. Interestingly, knocking-down TRIM24 sensitized the spheroids to both CB839 and BSO. Combining the two drugs with TRIM24-knockdown had an additive effect in reducing cell viability.

NRF2 has been report to exert both tumor suppressive and tumor promoting characteristics [121]. Under normal conditions, NRF2 activation is initiated by disrupted interactions with its binding partner KEAP1. It's well-established that NRF2 protein is aberrantly accumulated in many different types of cancers [98, 121, 122]. In cancer cells, *Nrf2* transcription can be activated independently of KEAP1, induced by oncogene *Kras*, *Braf* and *Myc* to promote tumorigenesis and protect them from oxidative stress [97]. *Trim24*<sup>COE-897</sup> spheroids showed more than two-fold increase in c-Myc protein level. Since oncogenic *Myc* is known to augment the transcription of *Nrf2* [97], upregulated c-MYC could be a potential mediator between TRIM24 over expression and high NRF2 level in *Trim24*<sup>COE-897</sup> spheroids. There is also a growing amount of evidence that crosstalk between NRF2 and tumor suppressor p53 impacts the capacity to mitigate oxidative stress. A p53 target gene p21 (*CDKN1A*) has been shown to interfere with NRF2 degradation by binding KEAP1, thus stabilizing NRF2 [123]. Other researchers reported that p53 counteracts the NRF2-mediated transcription of ARE element-containing genes through direct inhibition of these promoters [124]. In 3D spheroid culture, NRF2-p53 coregulation depends on context, as NRF2 signaling is reportedly independent of p53 in invasive TNBC spheroids [125].

Using ChIP-qPCR, Zhang *et al.* discovered that NRF2 regulates transcription of *TRIM24*. The phosphorylation of NRF2 is promoted by bone morphogenic protein 8A

(BMP8A), a member of transforming growth factor  $\beta$  (TGF $\beta$ ), to enhance survival and resistance to drug [126]. Here, we showed that NRF2 is induced by TRIM24 over expression. Through activating the transcription of ARE element-regulated genes, NRF2 plays a crucial role in activating enzymes that increase cytosolic NADPH production [94]. With high NRF2 protein levels in *Trim24*<sup>COE</sup> spheroids, the total NADP(H) and reduced NADPH abundance are also much greater, compared to controls. Inspired by the resistance of *Trim24*<sup>COE</sup> lines to high-dose H<sub>2</sub>O<sub>2</sub> treatment, we found that NRF2 and its known downstream target genes in the antioxidant program [86, 127] were upregulated in *Trim24*<sup>COE-897</sup> lines and downregulated upon TRIM24 knock-down. Under oxidative stress, created by extracellular H<sub>2</sub>O<sub>2</sub> addition, *Nrf2* mRNA expression was induced in both *Trim24*<sup>COE</sup> lines and shTrim24-897 lines. However, the NRF2 protein level was only induced in *Trim24*<sup>COE-897</sup> but downregulated in shTrim24-897. Knocking-down TRIM24 under oxidative stress abolished the increase of NRF2 protein but not the mRNA. It's possible that TRIM24 interferes with the NRF2 protein degradation process to increase the NRF2 level, instead of directly promoting *Nrf2* transcription. It would be interesting to learn if KEAP1 protein level is regulated by TRIM24 under oxidative stress in future studies.

Breast cancer is a highly heterogeneous disease, and several studies in recent years attempted to elucidate heterogeneous metabolic preferences or dependencies across BC subtypes. A recent single-cell RNA sequencing (scRNA-seq)-based, multi-omics study corroborated lineage-specific metabolic heterogeneity in mammary epithelial cells (MECs) [128]. This study highlighted that enrichment in glycolysis-related pathways occurred in basal epithelial cells and enriched oxidative respiration was present in luminal epithelial cells which indicates higher mitochondrial activity. Bioinformatics analysis further demonstrated that breast cancer cells retain the metabolic features of their cellular origin, for instance, a subgroup of TNBC cells that derived from the luminal progenitor cells display high oxidative respiration which is the same as their cell of origin [128]. TNBC can also be classified as metabolic-pathway-based subtypes (MPSs) and each subtype has

distinct molecular subtype distributions and genomic alterations [129]. With a multi-omics database of 465 TNBC patient samples, Gong *et al.* identified three MPSs: MPS1 with upregulated lipid metabolism; MPS2 with upregulated carbohydrate and nucleotide metabolism; and MPS3 with partial pathway dysregulation [129]. Given the metabolic heterogeneity of breast cancer, it is important to understand the mechanistic basis for variation in redox status between different breast cancer subtypes.

*Trim24*<sup>COE-567</sup> and *Trim24*<sup>COE-897</sup> lines are both derived from mouse mammary tumors driven by *Trim24* over expression. However, the primary cell lines were generated from endpoint tumors, which have distinct gene expression patterns as confirmed by RNA sequencing. Although all *Trim24*<sup>COE</sup> spheroid lines have a better capacity to handle oxidative stress, they may have rewired metabolic pathways in their own distinct way to achieve antioxidant defense, due to heterogeneity (Tables 1, 2 and 3). *Trim24*<sup>COE-897</sup> spheroids upregulated the PPP shunt, 1C-metabolism, glutamate synthesis, glutaminolysis, GSH synthesis, and NRF2 levels to enhance the production of reducing equivalents and GSH. On the other hand, *Trim24*<sup>COE-567</sup> spheroids only increased 1C-metabolism and glutamate synthesis. As *Trim24*<sup>COE-567</sup> spheroids showed remarkable increases in proline abundance, compared to the control and *Trim24*<sup>COE-897</sup>, it's possible that *Trim24*<sup>COE-567</sup> spheroids are using proline anabolism/catabolism pathways to diminish the deleterious effect of ROS [130, 131]. This is an avenue of potential future determinations.

	TRIM24 <sup>COE-567</sup> (COE line)	TRIM24 <sup>COE-897</sup> (COE line)	shCT-897	shTrim24-897	Increased Decreased
↓ ROS production	Cellular ROS	Cellular ROS	Cellular ROS	Cellular ROS	↑ ROS
	Mito ROS	Mito ROS	Mito ROS	Mito ROS	
	TCA activity	TCA activity	TCA activity	TCA activity	
GSH level	Glutamate synthesis	Glutamate synthesis	Glutamate synthesis	Glutamate synthesis	GSH level
	GSH synthesis	GSH synthesis	GSH synthesis	GSH synthesis	
	GSH/GSSG ratio	GSH/GSSG ratio	GSH/GSSG ratio	GSH/GSSG ratio	
Drug response	Viability – GLS1 inhibitor	Viability – GLS1 inhibitor	Viability – GLS1 inhibitor	Viability – GLS1 inhibitor	Drug response
	Viability – GSS inhibitor	Viability – GSS inhibitor	Viability – GSS inhibitor	Viability – GSS inhibitor	
	Viability – GLS+GSS inhibitor	Viability – GLS+GSS inhibitor	Viability – GLS+GSS inhibitor	Viability – GLS+GSS inhibitor	

**Table 1: Summary of rewired glycolysis and 1C-metabolism in *Trim24*<sup>COE</sup> spheroids and shCT/shTrim24-897 spheroids**

	TRIM24 <sup>COE-567</sup> (COE line)	TRIM24 <sup>COE-897</sup> (COE line)	shCT-897	shTrim24-897	Increased Decreased
↓ ROS production	Cellular ROS	Cellular ROS	Cellular ROS	Cellular ROS	↑ ROS
	Mito ROS	Mito ROS	Mito ROS	Mito ROS	
	TCA activity	TCA activity	TCA activity	TCA activity	
GSH level	Glutamate synthesis	Glutamate synthesis	Glutamate synthesis	Glutamate synthesis	GSH level
	GSH synthesis	GSH synthesis	GSH synthesis	GSH synthesis	
	GSH/GSSG ratio	GSH/GSSG ratio	GSH/GSSG ratio	GSH/GSSG ratio	
Drug response	Viability – GLS1 inhibitor	Viability – GLS1 inhibitor	Viability – GLS1 inhibitor	Viability – GLS1 inhibitor	Drug response
	Viability – GSS inhibitor	Viability – GSS inhibitor	Viability – GSS inhibitor	Viability – GSS inhibitor	
	Viability – GLS+GSS inhibitor	Viability – GLS+GSS inhibitor	Viability – GLS+GSS inhibitor	Viability – GLS+GSS inhibitor	

**Table 2: Summary of rewired GSH synthesis pathway in *Trim24*<sup>COE</sup> spheroids and shCT/shTrim24-897 spheroids**



	TRIM24 <sup>COE-567</sup> (COE line) – H <sub>2</sub> O <sub>2</sub>	TRIM24 <sup>COE-897</sup> (COE line) – H <sub>2</sub> O <sub>2</sub>	shCT-897 – H <sub>2</sub> O <sub>2</sub>	shTrim24-897 – H <sub>2</sub> O <sub>2</sub>	Increased Decreased
↓ ROS production	Cellular ROS	Cellular ROS	Cellular ROS	Cellular ROS	↑ ROS
	Mito ROS	Mito ROS	Mito ROS	Mito ROS	
	TCA activity	TCA activity	TCA activity	TCA activity	
GSH level	NRF2 expression	NRF2 expression	NRF2 expression	NRF2 expression	GSH level
	glutaminolysis	glutaminolysis	glutaminolysis	glutaminolysis	
	GSH/GSSG ratio	GSH/GSSG ratio	GSH/GSSG ratio	GSH/GSSG ratio	
	viability	viability	viability	viability	
	NADPH	NADPH	NADPH	NADPH	
	Total NADPH	Total NADPH	Total NADPH	Total NADPH	

**Table 3: Summary of NRF2-regulated response under oxidative stress in *Trim24*<sup>COE</sup> spheroids and shCT/shTrim24-897 spheroids**

In conclusion, TRIM24-overexpressing mammary tumor spheroids have less intracellular ROS level compared to the MMTV<sup>Cre</sup> control breast cancer spheroids. The low ROS level is the result of low mitochondrial ROS production, as well as increased NADPH and GSH production driven by TRIM24 over expression. The upregulated reducing power and antioxidant pathways in *Trim24*<sup>COE</sup> spheroids promote cell survival under oxidative-stress conditions. NRF2, as a transcription target of TRIM24, acts as a central mediator between TRIM24 over expression and downstream metabolic reprogramming. Metabolic heterogeneity exists between TRIM24-overexpressing spheroid lines. Although mammary tumorigenesis was driven by the same oncoprotein, *Trim24*<sup>COE-567</sup> and *Trim24*<sup>COE-897</sup> spheroids exhibited different degrees of TRIM24 over expression and, likely, took different routes to achieve higher antioxidant defense to combat oxidative stress. As tumors respond differently to specific inhibitors, metabolic heterogeneity needs to be taken into account when designing potential therapeutic plans. Knocking-down or inhibiting TRIM24 in combination with metabolic inhibitors may offer a

promising direction in treating MpBC tumors, which requires considerable preclinical assessments and further investigations to determine.

## Appendix

### Appendix 1: List of antibodies used for immunoblots

Antibody	species	MW	Dilution	Catalog#
Trim24	Rb	130 KD	1 in 2000	14208-1-AP
beta-actin	Ms	42 KD	in 10000	
SMA	Rb	42 KD	1 in 1000	ab4694
PGK	Rb	45 KD	in 1000	ab154613
PGM1	Rb	61 KD	1 in 2000	ab192876
Enolase1	Rb	47 KD	1 in 1000	3810T
PCK1	Rb	69 KD	1 in 1000	ab70358
GLS	Rb	58,65kD	1 in 2000	12855
HIF1-a	Ms	93 KD	1 in 2000	400080
ASNS	Rb	64 KD	1 in 2000	14681-1-AP
Cytokeratin 5	Rb	62 KD	1 in 1000	ab53121
cytokeratin14	Ma	40, 68 KD	1 in 200	ab7800
Cytokeratin8	Rb	52 KD	1 in 10000	ab53280
Cadherin E	Rb	135 KD	1 in 1000	24-E-10
Cadherin N	Rb	130 KD	1 in 2000	GTX112733
GluD1	Rb	45-55 KD	1 in 2000	14299-1-AP
GluL	Rb	42 KD	1 in 1000	ab73593
PHGDH	Rb	57 KD	1 in 1000	ab211365
Aldolase	Rb	40 KD	1 in 1000	#3188
FBP1	Rb	36 KD	1 in 2000	ab109732
SNAI1	Rb	26 KD	1 in 2000	GTX125918
NAMPT	Rb	56 KD	1 in 250	ab45890
G6PD	Rb	59 KD	1 in 1000	ab76598
Vimentin	Rb	54 KD	1 in 1000	ab92547
PGD	Rb	45 KD	1 in 1000	ab129199
NRF2	Rb	110 KD	1 in 2000	ab137550
GSR	Rb	53 KD	1 in 2000	18257-1-AP
GPX4	Rb	17 KD	1 in 2000	ab125066
GSS	Rb	52 KD	1 in10000	ab124811
GLS2	Rb	66 KD	1 in 2000	ab113509
PGAM1	Rb	28 KD	1 in 2000	ab247037
SOD1	Rb	20 KD	1 in 2000	10269-1-AP
GST	Rb	46 KD	1 in 1000	#2625
GSTP1	Rb	23 KD	1 in 1000	GTX112695
GOT1	Rb	55KD	1 in 5000	ab239487
GOT2	Rb	43 KD	1 in 2000	ab171739
Caspase 3	Rb	35 KD	1 in 1000	#9662

cleaved Caspase3	Rb	17 KD	1 in 1000	#9664S
PSAT1	Rb	37-45 KD	1 in 1000	10501-1-AP
ME1	Rb	55-64 KD	1 in 1000	16619-1-AP
TALDO1	Rb	38 KD	1 in 1000	12378-1-AP
IDH1	Rb	46 KD	1 in 1000	3997S
ASCT2	Rb	49, 75 KD	1 in 1000	#5345S
P53	Rb	53 KD	1 in 2000	10442-1-AP
SHMT1	Rb	53 KD	1 in 1000	14149-1-AP
SHMT2	Rb	55 KD	1 in 1000	11099-1-AP
TWIST1/2	Rb	21 KD	1 in 2000	GTX127310
TGFβ	Rb	44 KD	1 in 1000	ab179695
SOX2	Ms	34 KD	1 in 1000	ab171380
ZO-1	Rb	230 KD	1 in 2000	21773-1-AP
GCLC	Rb	73 KD	1 in 2000	12601-1-AP
MTHFD	Rb	101 KD	1 in 1000	10794-1-AP
SLC7a11 (xCT)	Rb	35 KD	1 in 1000	#12691
KLF4	Rb	50-60 KD	1 in 1000	11880-1-AP
GLP	Rb	141 KD	1 in 5000	ab231224
G9A	Rb	160 KD	1 in 1000	ab285050
Integrin β4	Rb	200- 240KD	1:500,1000	21738-1-AP
CD44	Rb	80-95KD	1 in 2000	15675-1-AP
PKM2	Rb	58 KD	1 in 1000	15822-1-AP
ATF4	Rb	49 KD	1 in 1000	#118155
ER	Rb	68 KD	1:500,1000	NBP1- 04936
PR	Rb	90,118 KD	1 in 1000	#3153
HER2	Rb	185 KD	1 in 1000	#2165
ZEB1	Rb	190-210 KD	1 in 1000	21544-1-AP
PRODH	Rb	56,66 KD	1 in 1000	22980-1-AP
PYCR	Rb	33,35 KD	1 in 500	13108-1-AP
ALDH1A4 (P5CDH)	Rb	62 KD	in in 500	11604-1-AP

## Appendix 2: List of primers

Primer name	Sequence
<i>18S-Fw</i>	TCAAGAACGAAAGTCGGAGGTT
<i>18S-Rv</i>	GGACATCTAAGGGCATCACAG
<i>Asns-Fw</i>	GCCTCCAACCGGTCTTGTC
<i>Asns-Rv</i>	CACACATGCTACAGGCGGAC
<i>G6PD-Fw</i>	GGGAAGAGTTGTACCAGGGTG
<i>G6PD-Rv</i>	TCTTCAGGTAGAAGGCCATCCC
<i>Gclc-Fw</i>	CACATCTACCACGCAGTCAAG
<i>Gclc-Rv</i>	AGGACACCAACATGTACTCCAC
<i>Gclm-Fw</i>	AGTTGACATGGCATGCTCCG
<i>Gclm-Rv</i>	TCCATCTTCAATCGGAGGCG
<i>GLS1-Fw</i>	CTCGGAGAGAAGGAGGTGAT
<i>GLS1-Rv</i>	ATCTCCAGTGTATGCGGCAA
<i>GLS2-Fw</i>	AGGGAAGGAGGAGAGGTTTCG
<i>GLS2-Rv</i>	CCATGGCCGACAATGCAAAC
<i>GluD-Fw</i>	AGCTGGCCAAGAAGGGTTTT
<i>GluD-Rv</i>	GCATAGGTGTCAGCGATCCA
<i>GluL- Rv</i>	GGATGGGTGAACAGGTCAGG
<i>GluL-Fw</i>	GCGGAGAATGGGAGTAGAGC
<i>Gpx4-Fw</i>	CCGTCTGAGCCGCTTACTTA
<i>GPx4-Rv</i>	GGCTGAGAATTCGTGCATGG
<i>Gsr-Fw</i>	TGGCACTTGCGTGAATGTTG
<i>Gsr-Rv</i>	TGTTCAGGCGGCTCACATAG
<i>Gss-Fw</i>	CCAAAGCCTGGGAGCTCTAT
<i>Gss-Rv</i>	ACGGCACGCTGGTCAAATA
<i>Gstp1-Fw</i>	GCGGCAAATATGTCACCCTCA
<i>Gstp2-Rv</i>	GAAAGCTTTGCCTCCCTGGT
<i>HIF1<math>\alpha</math>-Fw</i>	TTCTCTGCCAGTTTTCTGGG
<i>HIF1<math>\alpha</math>-Rv</i>	ACTCTTTGCTTCGCCGAGAT
<i>IDH1-Fw</i>	TGCAAGGAGATGAAATGACACG
<i>IDH1-Rv</i>	TGGTGGCATCACGATTCTCT
<i>ME1-Fw</i>	GGGACCCGCATCTCAACAAG
<i>ME1-Rv</i>	TCGAAGTCAGAGTTCAGTCGT
<i>MTHFD1-Fw</i>	ATCCTGTCACTGCAAAGCCC
<i>MTHFD1-Rv</i>	CACCAGGGACGGGAGTGATA
<i>N-Cadherin-Fw</i>	AGGATGTGCACGAAGGACAG
<i>N-Cadherin-Rv</i>	CTTGAAATCTGCTGGCTCGC

<i>NAMPT-Fw</i>	CTGTGGCGGGAATTGCTCTA
<i>Nampt-Fw</i>	CATTCAAGGAGATGGCGTGGA
<i>NAMPT-Rv</i>	GTCTTTCCCCCAAGCCGTTA
<i>Nampt-Rv</i>	CACCAGAACCGAAGGAGACA
<i>Nqo1-Fw</i>	ACGTCATTCTCTGGCCGATT
<i>Nqo1-Rv</i>	TCTCCTCCCAGACGGTTTCC
<i>NRF2-Fw</i>	AATTCCTCCCAATTCAGCCG
<i>NRF2-Rv</i>	TGTTTGGGAATGTGGGCAAC
<i>P5cdh-fw</i>	AACGCTGCTGGCAACTTCTA
<i>P5cdh-Rv</i>	CCTCCTGGCTTGTCATTGGT
<i>P5cs-Fw</i>	AGTCTCGCCCTGACTGTCTA
<i>P5cs-rv</i>	CCCACCTTTGAGCAACAAGC
<i>PGD-Fw</i>	TCCTCGACTCTGCTTCGTCT
<i>PGD-Rv</i>	GACTGTGCACCAACCACCTT
<i>PGK1-Fw</i>	TGCTGGAAAACCTCCGCTTT
<i>PGK1-Rv</i>	TGAGGCTCGGAAAGCATCAA
<i>Phgdh-Fw</i>	GGCCTCGGCAGAATTGGAA
<i>Phgdh-Rv</i>	TCAGGAGAGATGATGGGGTCA
<i>Prodh-Fw</i>	TGATGGTGGCTTCCCACAAC
<i>Prodh-Rv</i>	CGAAGCACACCTGACCATCA
<i>Pycr-Fw</i>	CGCGTGGCGAATGCAAG
<i>Pycr-Rv</i>	GCTGGCCATTATCTTGTGTGC
<i>Shmt1-Fw</i>	GGAACAGACGTTTACGGCCA
<i>Shmt1-Rv</i>	GTCTGCCATTGCACTGGTTC
<i>Shmt2-Fw</i>	GCCTCCTGTAGCGATGGTAT
<i>Shmt2-Rv</i>	GACCAGCTGACCACATCTC
<i>Slc7a11-Fw</i>	TCTGGGTGGAAGTCTCGTA
<i>Slc7a11-Rv</i>	GTTCCAGGATGTAGCGTCCA
<i>Snai1-Fw</i>	GTCTGCACGACCTGTGGAAA
<i>Snai1-Rv</i>	GGTCAGCAAAAGCACGGTTG
<i>TALDO1-Fw</i>	ATCATCAACCTGGGAGGGGA
<i>TALDO1-Rv</i>	GTCATGTTGCAGTGGATGCC
<i>Twist1-Fw</i>	GTCCCACTAGCAGCGGAG
<i>Twist1-Rv</i>	CCAGAGTCTCTAGACTGTCCAT
<i>Zeb1-Fw</i>	GTGTAAGCGCAGAAAGCAGG
<i>Zeb1-Rv</i>	TGGAGTTTGTCTTCATCATCGGA

### Appendix 3: List of drug and reagents

Reagents	Company	Dilution	Catalog#
30 % H <sub>2</sub> O <sub>2</sub>	Fisher Scientific	500 µM, 1 mM	H325-500
CB-839 (Telaglenastat)	Selleckchem	10 µM, 20 µM	S7655
BPTE	Sigma	10 µM, 20 µM	SML0601-25MG
CBR5884	Millipore Sigma	30 µM, 60 µM	SML1656-5MG
L-Buthionine-sulfoximine	Millipore Sigma	50 µM, 100 µM	B2515
CellRox Deep Red	Life Technologies	1:1000	C10422
MitoSox Orange	Life Technologies	1:1000	M36008

## References

- 1 Koppenol WH, Bounds PL, Dang CV. Otto Warburg's contributions to current concepts of cancer metabolism. *Nat Rev Cancer* 2011; 11: 325-337.
- 2 DeBerardinis RJ, Chandel NS. We need to talk about the Warburg effect. *Nature Metabolism* 2020; 2: 127-129.
- 3 Racker E. Bioenergetics and the problem of tumor growth. *American Scientist* 1972; 60: 56-63.
- 4 Wang T, Marquardt C, Foker J. Aerobic glycolysis during lymphocyte proliferation. *Nature* 1976; 261.
- 5 Warburg O. On the origin of cancer cells. *Science* 1956; 123.
- 6 Jose C, Bellance N, Rossignol R. Choosing between glycolysis and oxidative phosphorylation: a tumor's dilemma? *Biochim Biophys Acta* 2011; 1807: 552-561.
- 7 Katsyuba E, Romani M, Hofer D, Auwerx J. NAD<sup>+</sup> homeostasis in health and disease. *Nature Metabolism* 2020; 2: 9-31.
- 8 Purohit V, Simeone DM, Lyssiotis CA. Metabolic Regulation of Redox Balance in Cancer. *Cancers (Basel)* 2019; 11.



- 9 Perillo B, Di Donato M, Pezone A, Di Zazzo E, Giovannelli P, Galasso G, Castoria G, Migliaccio A. ROS in cancer therapy: the bright side of the moon. *Exp Mol Med* 2020; 52: 192-203.
- 10 Srinivas US, Tan BWQ, Vellayappan BA, Jeyasekharan AD. ROS and the DNA damage response in cancer. *Redox Biol* 2019; 25: 101084.
- 11 Chio IIC, Tuveson DA. ROS in Cancer: The Burning Question. *Trends Mol Med* 2017; 23: 411-429.
- 12 DeBerardinis RJ, Chandel NS. Fundamentals of cancer metabolism. *Sci Adv* 2016; 2: 18.
- 13 Anderson NM, Mucka P, Kern JG, Feng H. The emerging role and targetability of the TCA cycle in cancer metabolism. *Protein Cell* 2018; 9: 216-237.
- 14 Chaiswing L, St Clair WH, St Clair DK. Redox Paradox: A Novel Approach to Therapeutics-Resistant Cancer. *Antioxid Redox Signal* 2018; 29: 1237-1272.
- 15 Global Cancer Observatory, vol. 2021. World Health Organization.
- 16 Harbeck N, Gnant M. Breast cancer. *The Lancet* 2017; 389: 1134-1150.
- 17 Ciriello G, Gatza ML, Beck AH, Wilkerson MD, Rhie SK, Pastore A, Zhang H, McLellan M, Yau C, Kandoth C, Bowlby R, Shen H, Hayat S, Fieldhouse R, Lester SC, Tse GMK, Factor RE, Collins LC, Allison KH, Chen YY, Jensen K,

- Johnson NB, Oesterreich S, Mills GB, Cherniack AD, Robertson G, Benz C, Sander C, Laird PW, Hoadley KA, King TA, TCGA Research Network, Perou CM. Comprehensive Molecular Portraits of Invasive Lobular Breast Cancer. *Cell* 2015; 163: 506-519.
- 18 Eliyatkin N, Yalcin E, Zengel B, Aktas S, Vardar E. Molecular Classification of Breast Carcinoma: From Traditional, Old-Fashioned Way to A New Age, and A New Way. *J Breast Health* 2015; 11: 59-66.
- 19 Bianchini G, Balko JM, Mayer IA, Sanders ME, Gianni L. Triple-negative breast cancer: challenges and opportunities of a heterogeneous disease. *Nat Rev Clin Oncol* 2016; 13: 674-690.
- 20 Al-Mahmood S, Sapiezynski J, Garbuzenko OB, Minko T. Metastatic and triple-negative breast cancer: challenges and treatment options. *Drug Deliv Transl Res* 2018; 8: 1483-1507.
- 21 Burstein MD, Tsimelzon A, Poage GM, Covington KR, Contreras A, Fuqua SAW. Comprehensive Genomic Analysis Identifies Novel Subtypes and Targets of Triple-Negative Breast Cancer. *Clinical Cancer Research* 2014; 21: 1688-1698.
- 22 Cortazar P, Zhang J, Untch M, Mehta K, Costantino JP, Wolmark N. Pathological complete response and long-term clinical benefit in breast cancer: the CTNeoBC pooled analysis. *The Lancet* 2014; 384: 164-172.

- 23 Sun X, Wang M, Wang M, Yu X, Guo J, Sun T, Li X, Yao L, Dong H, Xu Y. Metabolic Reprogramming in Triple-Negative Breast Cancer. *Front Oncol* 2020; 10: 428.
- 24 Gandhi N, Das GM. Metabolic Reprogramming in Breast Cancer and Its Therapeutic Implications. *Cells* 2019; 8.
- 25 Sanchez-Vega F, Mina M, Armenia J, Chatila WK, Luna A, La KCI. Oncogenic Signaling Pathways in The Cancer Genome Atlas. *Cell* 2018; 173: 321-337 e310.
- 26 Tray N, Taff J, Adams S. Therapeutic landscape of metaplastic breast cancer. *Cancer Treat Rev* 2019; 79: 101888.
- 27 Park HS, Park S, Kim JH, Lee JH, Choi SY, Park BW. Clinicopathologic features and outcomes of metaplastic breast carcinoma: comparison with invasive ductal carcinoma of the breast. *Yonsei Med J* 2010; 51: 864-869.
- 28 Tsai WW, Wang Z, Yiu TT, Akdemir KC, Xia W, Winter S, Tsai CY, Shi X, Schwarzer D, Plunkett W, Aronow B, Gozani O, Fishle W, Hung MC, Patel DJ, Barton MC. TRIM24 links a non-canonical histone signature to breast cancer. *Nature* 2010; 468: 927-932.
- 29 Appikonda S, Thakkar KN, Barton MC. Regulation of gene expression in human cancers by TRIM24. *Drug Discov Today Technol* 2016; 19: 57-63.

- 30 Jain AK, Allton K, Duncan AD, Barton MC. TRIM24 is a p53-induced E3-ubiquitin ligase that undergoes ATM-mediated phosphorylation and autodegradation during DNA damage. *Mol Cell Biol* 2014; 34: 2695-2709.
- 31 Allton K, Jain AK, Herz HM, Tsai WW, Jung SY, Qin J, Bergmann A, Johnson RL, Barton MC. Trim24 targets endogenous p53 for degradation. *Proc Natl Acad Sci U S A* 2009; 106: 11612-11616.
- 32 Pathiraja TN, Thakkar KN, Jiang S, Stratton S, Liu Z, Gagea M, Shi X, Shah PK, Phan L, Lee MH, Anderson J, Stampfer M, Barton MC. TRIM24 links glucose metabolism with transformation of human mammary epithelial cells. *Oncogene* 2015; 34: 2836-2845.
- 33 Shah VV, Duncan AD, Jiang S, Stratton SA, Allton KL, Yam C, Jain A, Krause PM, Lu Y, Cai Shirong, Tu Y, Zhou X, Zhang X, Jiang Y, Carroll CL, Kang Z, Liu B, Shen J, Gagea M, Manu SM, Huo L, Gilcrease M, Powell RT, Guo L, Stepha C, Davies PJ, Parker-Thornburg J, Lozano G, Behringer RR, Piwnica-Worms H, Chang JT, Moulder SL, Barton MC. Mammary-specific expression of Trim24 establishes a mouse model of human metaplastic breast cancer *Nat Commun* 2021.
- 34 Nguyen-Ngoc KV, Shamir ER, Huebner RJ, Beck JN, Cheung KJ, Ewald AJ. 3D culture assays of murine mammary branching morphogenesis and epithelial invasion. *Methods Mol Biol* 2015; 1189: 135-162.

- 35 Jardé T, Lloyd-Lewis B, Thomas M, Kendrick H, Melchor L, Bougaret L. Wnt and Neuregulin1/ErbB signalling extends 3D culture of hormone responsive mammary organoids. *Nature Communications* 2016; 7.
- 36 Bolger AM, Lohse M, Usadel B. Trimmomatic: a flexible trimmer for Illumina sequence data. *Bioinformatics* 2014; 30: 2114-2120.
- 37 Dobin A, Davis CA, Schlesinger F, Drenkow J, Zaleski C, Jha S, Batut P, Chaisson M, Gingerass TR. STAR: ultrafast universal RNA-seq aligner. *Bioinformatics* 2013; 29: 15-21.
- 38 Anders S, Pyl PT, Huber W. HTSeq--a Python framework to work with high-throughput sequencing data. *Bioinformatics* 2015; 31: 166-169.
- 39 Love MI, Huber W, Anders S. Moderated estimation of fold change and dispersion for RNA-seq data with DESeq2. *Genome Biol* 2014; 15: 550.
- 40 Subramanian A, Tamayo P, Mootha VK, Mukherjee S, Ebert BL, Gillette MA. Gene set enrichment analysis: A knowledge-based approach for interpreting genome-wide expression profiles. *Proceedings of the National Academy of Sciences* 2005; 102: 15545-15550.
- 41 Sachs N, de Ligt J, Kopper O, Gogola E, Bounova G, Weeber F, Balgobind AV, Wind K, Gracanin A, Begthel H, Korving J, van Boxtel R, Duarte AA, Lelieveld D, van Hoeck A, Ernst RF, Blokzijl F, Nijman IJ, Hoogstraat M, van de Ven M, Egan DA, Zinzalla V, Moll J, Boj SF, Voest EE, Wessels L, van Diest PJ, Rottenberg S,

- Vries RGJ, Cuppen E, Clevers H. A Living Biobank of Breast Cancer Organoids Captures Disease Heterogeneity. *Cell* 2018; 172: 373-386.e310.
- 42 VanderVorst K, Hatakeyama J, Berg A, Lee H, Carraway KL, 3rd. Cellular and molecular mechanisms underlying planar cell polarity pathway contributions to cancer malignancy. *Semin Cell Dev Biol* 2018; 81: 78-87.
- 43 MacMillan CD, Leong HS, Dales DW, Robertson AE, Lewis JD, Chambers A. Stage of breast cancer progression influences cellular response to activation of the WNT/planar cell polarity pathway. *Sci Rep* 2014; 4: 6315.
- 44 Bill R, Christofori G. The relevance of EMT in breast cancer metastasis: Correlation or causality? *FEBS Lett* 2015; 589: 1577-1587.
- 45 Vasaikar SV, Deshmukh AP, den Hollander P, Addanki S, Kuburich NA, Kudaravalli S, Joseph R, Chang JT, Soundararajan R, Mani SA. EMTome: a resource for pan-cancer analysis of epithelial-mesenchymal transition genes and signatures. *Br J Cancer* 2021; 124: 259-269.
- 46 Fischer KR, Durrans A, Lee S, Sheng J, Li F, Wong ST, Choi H, Rayes TE, Ryu S, Troeger J, Schwabe RF, Vahdat LT, Altorki NK, Mittal V, Gao D. Epithelial-to-mesenchymal transition is not required for lung metastasis but contributes to chemoresistance. *Nature* 2015; 527: 472-476.
- 47 Saitoh M. Involvement of partial EMT in cancer progression. *J Biochem* 2018; 164: 257-264.

- 48 Yang J, Antin P, Berx G, Blanpain C, Brabletz T, Bronner M, Campbell K, Cano A, Casanova J, Christofori G, Dedhar S, Derynck R, Ford HL, Fuxe J, Herreros AG, Goodall GJ, Hadjantonakis AK, Huang RJY, Kalcheim C, Kalluri R, Kang Y, Khew-Goodall Y, Levine H, Jinsong Liu, Longmore GD, Mani SA, Massagué J, Mayor R, McClay D, Mostov KE, Newgreen DF, Nieto MA, Puisieux A, Runyan R, Savagner P, Stanger B, Stemmler MP, Takahashi Y, Takeichi M, Thevenneau E, Thiery JP, Thompson EW, Weinberg RA, Williams ED, Xing J, Zhou BP, Sheng G. Guidelines and definitions for research on epithelial-mesenchymal transition. *Nat Rev Mol Cell Biol* 2020; 21: 341-352.
- 49 Liu X, Fan D. The Epithelial-Mesenchymal Transition and Cancer Stem Cells: Functional and Mechanistic Links. *Current Pharmaceuticla Design* 2015; 21: 13.
- 50 Mani SA, Guo W, Liao MJ, Eaton EN, Ayyanan A, Zhou AY, Brooks M, Reinhard, F, Zhang CC, Shipitsin M, Campbell LL, Polyak K, Briskin C, Yang J, Weinberg RA. The epithelial-mesenchymal transition generates cells with properties of stem cells. *Cell* 2008; 133: 704-715.
- 51 Wu HT, Zhong HT, Li GW, Shen JX, Ye QQ, Zhang ML, Lu J. Oncogenic functions of the EMT-related transcription factor ZEB1 in breast cancer. *J Transl Med* 2020; 18: 51.
- 52 Bocci F, Tripathi SC, Vilchez Mercedes SA, George JT, Casabar JP, Wong PK Hanash SM, Levine H, Casabar JP, Wong PK, Hanash SM, Levine H, Onuchic JN, Jolly MK. NRF2 activates a partial epithelial-mesenchymal transition and is

- maximally present in a hybrid epithelial/mesenchymal phenotype. *Integr Biol (Camb)* 2019; 11: 251-263.
- 53 Stine ZE, Walton ZE, Altman BJ, Hsieh AL, Dang CV. MYC, Metabolism, and Cancer. *Cancer Discov* 2015; 5: 1024-1039.
- 54 Wise DR, DeBerardinis RJ, Mancuso A, Sayed N, Zhang XY, Pfeiffer HK. Myc regulates a transcriptional program that stimulates mitochondrial glutaminolysis and leads to glutamine addiction. *Proc Natl Acad Sci U S A* 2008; 105: 18782-18787.
- 55 Yin S, Cheryan VT, Xu L, Rishi AK, Reddy KB. Myc mediates cancer stem-like cells and EMT changes in triple negative breast cancers cells. *PLoS One* 2017; 12: e0183578.
- 56 Zhang J, Li G, Feng L, Lu H, Wang X. Kruppel-like factors in breast cancer: Function, regulation and clinical relevance. *Biomed Pharmacother* 2020; 123: 109778.
- 57 Xu H, Tian Y, Yuan X, Wu H, Liu Q, Pestell RG, Wu K. The role of CD44 in epithelial-mesenchymal transition and cancer development. *Onco Targets Ther* 2015; 8: 3783-3792.
- 58 Zhang LH, Yin YH, Chen HZ, Feng SY, Liu JL, Chen L, Fu WL, Sun GC, Yu XG, Xu DG. TRIM24 promotes stemness and invasiveness of glioblastoma cells via activating Sox2 expression. *Neuro Oncol* 2020; 22: 1797-1808.



- 59 Vidi PA, Bissell MJ, Lelievre SA. Three-dimensional culture of human breast epithelial cells: the how and the why. *Methods Mol Biol* 2013; 945: 193-219.
- 60 Clevers DTH. Cancer modeling meets human organoid technology 2019; 364: 952-955.
- 61 Sachs N, Clevers H. Organoid cultures for the analysis of cancer phenotypes. *Curr Opin Genet Dev* 2014; 24: 68-73.
- 62 Xu H, Lyu X, Yi M, Zhao W, Song Y, Wu K. Organoid technology and applications in cancer research. *J Hematol Oncol* 2018; 11: 116.
- 63 Cockfield JA, Schafer ZT. Antioxidant Defenses: A Context-Specific Vulnerability of Cancer Cells. *Cancers (Basel)* 2019; 11.
- 64 Hecht F, Cazarin JM, Lima CE, Faria CC, Leitao AA, Ferreira AC, Carvalho DP, Fortunato RS. Redox homeostasis of breast cancer lineages contributes to differential cell death response to exogenous hydrogen peroxide. *Life Sci* 2016; 158: 7-13.
- 65 Jiang L, Shestov AA, Swain P, Yang C, Parker SJ, Wang QA, Deberardinis RJ. Reductive carboxylation supports redox homeostasis during anchorage-independent growth. *Nature* 2016; 532: 255-258.
- 66 Kubli DA, Gustafsson AB. Mitochondria and mitophagy: the yin and yang of cell death control. *Circ Res* 2012; 111: 1208-1221.

- 67 Agilent Seahorse XF Cell Mito Stress Test Kit User Guide2019.
- 68 Fan J, Ye J, Kamphorst JJ, Shlomi T, Thompson CB, Rabinowitz JD.  
Quantitative flux analysis reveals folate-dependent NADPH production. *Nature*  
2014; 510: 298-302.
- 69 Keibler MA, Wasylenko TM, Kelleher JK, Iliopoulos O, Vander Heiden MG,  
Stephanopoulos G. Metabolic requirements for cancer cell proliferation. *Cancer*  
*Metab* 2016; 4: 16.
- 70 Tao R, Zhao Y, Chu H, Wang A, Zhu J, Chen X, Zou Y, Shi M, Liu R, Su N, Du J,  
Zhou HM, Zhu L, Qian X, Liu H, Loscalzo J, Yang Y. Genetically encoded  
fluorescent sensors reveal dynamic regulation of NADPH metabolism. *Nat*  
*Methods* 2017; 14: 720-728.
- 71 Zhu J, Schworer S, Berisa M, Kyung J, Ryu KW, Yi J, Jiang X, Cross JR,  
Thompson CB. Mitochondrial NADP(H) generation is essential for proline  
biosynthesis. *Science* 2021; 372: 968-972.
- 72 Kruger A, Gruning NM, Wamelink MM, Kerick M, Kirpy A, Parkhomchuk D,  
Bluemlein K, Schweiger MR, Soldatov A, Lehrach H, Jakobs C, Ralser M. The  
pentose phosphate pathway is a metabolic redox sensor and regulates  
transcription during the antioxidant response. *Antioxid Redox Signal* 2011; 15:  
311-324.

- 73 Sun Y, Bandi M, Lofton T, Smith M, Bristow CA, Carugo A, Rogers N, Leonard P, Chang Q, Mullinax R, Han J, Shi X, Seth S, Meyers BA, Miller M, Miao L, Ma X, Feng N, Virginia Giuliani, Do MG, Czako B, Palmer WS, Mseeh F, Asara JM, Jiang Y, Morlacchi P, Zhao S, Peoples M, Tieu TN, Warmoes MO, Lorenzi PL, Muller FL, DePinho RA, Draetta GF, Toniatti C, Jones P, Heffernan TF, Marszalek JR. Functional Genomics Reveals Synthetic Lethality between Phosphogluconate Dehydrogenase and Oxidative Phosphorylation. *Cell Rep* 2019; 26: 469-482 e465.
- 74 Hitosugi T, Zhou L, Elf S, Fan J, Kang HB, Seo JH, Shan C, Dai Q, Zhang L, Xie J, Gu TL, Jin P, Aleckovic M, LeRoy G, Kang Y, Sudderth JA, DeBerardinis RJ, Luan CH, Chen GZ, Muller S, Shin DM, Owonikoko TK, Lonial S, Arellano ML, Khoury HJ, Khuri FR, Lee BH, Ye K, Boggon TJ, Kang S, He C, Chen J. Phosphoglycerate mutase 1 coordinates glycolysis and biosynthesis to promote tumor growth. *Cancer Cell* 2012; 22: 585-600.
- 75 Locasale JW, Grassian AR, Melman T, Lyssiotis CA, Mattaini KR, Bass AJ, Heffron G, Metallo CM, Muranen T, Sharfi H, Sasaki AT, Anastasiou D, Mullarky E, Vokes NI, Sasaki M, Beroukhim R, Stephanopoulos G, Ligon AH, Meyerson M, Richardson AL, Chin L, Wagner G, Asara JM, Brugge JS, Cantley LC, Vander Heiden MG. Phosphoglycerate dehydrogenase diverts glycolytic flux and contributes to oncogenesis. *Nat Genet* 2011; 43: 869-874.
- 76 Mullarky E, Lucki NC, Zabka TS, Anglin JL, Gomes AP, Nicolay BN, Wong JCY, Christen S, Takahashi H, Singh PK, Blenis J, Warren JD, Fendt SM, Asara JM, DeNicola GM, Lyssiotis CA, Lairson LL, Cantley LC. Identification of a small

- molecule inhibitor of 3-phosphoglycerate dehydrogenase to target serine biosynthesis in cancers. *Proc Natl Acad Sci U S A* 2016; 113: E1585.
- 77 Ye J, Fan J, Venneti S, Wan YW, Pawel BR, Zhang J. Serine catabolism regulates mitochondrial redox control during hypoxia. *Cancer Discov* 2014; 4: 1406-1417.
- 78 Ohshima K, Nojima S, Tahara S, Kurashige M, Kawasaki K, Hori Y. Serine racemase enhances growth of colorectal cancer by producing pyruvate from serine. *Nat Metab* 2020; 2: 81-96.
- 79 Maddocks OD, Berkers CR, Mason SM, Zheng L, Blyth K, Gottlieb E. Serine starvation induces stress and p53-dependent metabolic remodelling in cancer cells. *Nature* 2013; 493: 542-546.
- 80 Correction for Mullarky E, Lucki NC, Zabka TS, Anglin JL, Gomes AP, Nicolay BN, Wong JCY, Christen S, Takahashi H, Singh PK, Blenis J, Warren JD, Fendt SM, Asara JM, DeNicola GM, Lyssiotis CA, Lairson LL, Cantley LC. Identification of a small molecule inhibitor of 3-phosphoglycerate dehydrogenase to target serine biosynthesis in cancers. *Proc Natl Acad Sci U S A* 2016; 113: E1585.
- 81 Jiang J, Srivastava S, Zhang J. Starve Cancer Cells of Glutamine: Break the Spell or Make a Hungry Monster? *Cancers (Basel)* 2019; 11.
- 82 Bott AJ, Maimouni S, Zong WX. The Pleiotropic Effects of Glutamine Metabolism in Cancer. *Cancers (Basel)* 2019; 11.

- 83 Choi BH, Coloff JL. The Diverse Functions of Non-Essential Amino Acids in Cancer. *Cancers (Basel)* 2019; 11.
- 84 DeBerardinis RJ, Cheng T. Q's next: the diverse functions of glutamine in metabolism, cell biology and cancer. *Oncogene* 2010; 29: 313-324.
- 85 DeBerardinis RJ, Mancuso A, Daikhin E, Nissim I, Yudkoff M, Wehrli S. Beyond aerobic glycolysis: transformed cells can engage in glutamine metabolism that exceeds the requirement for protein and nucleotide synthesis. *Proc Natl Acad Sci U S A* 2007; 104: 19345-19350.
- 86 Mitsuishi Y, Taguchi K, Kawatani Y, Shibata T, Nukiwa T, Aburatani H, Yamamoto M, Motohashi H. Nrf2 redirects glucose and glutamine into anabolic pathways in metabolic reprogramming. *Cancer Cell* 2012; 22: 66-79.
- 87 Son J, Lyssiotis CA, Ying H, Wang X, Hua S, Ligorio M, Perera RM, Ferrone CR, Mullarky E, Shyh-Chang N, Kang Y, Fleming JB, Bardeesy N, Asara JM, Haigis MC, DePinho RA, Cantley LC, Kimmelman AC. Glutamine supports pancreatic cancer growth through a KRAS-regulated metabolic pathway. *Nature* 2013; 496: 101-105.
- 88 Wei Q, Qian Y, Yu J, Wong CC. Metabolic rewiring in the promotion of cancer metastasis: mechanisms and therapeutic implications. *Oncogene* 2020; 39: 6139-6156.

- 89 Lampa M, Arlt H, He T, Ospina B, Reeves J, Zhang B, Murtie J, Deng G, Barberis C, Hoffmann D, Cheng H, Pollard J, Winter C, Richon V, Garcia-Escheverria C, Adrian F, Wiederschain D, Srinivasan L. Glutaminase is essential for the growth of triple-negative breast cancer cells with a deregulated glutamine metabolism pathway and its suppression synergizes with mTOR inhibition. *PLoS One* 2017; 12: e0185092.
- 90 Gross MI, Demo SD, Dennison JB, Chen L, Chernov-Rogan T, Goyal B, Janes JR, Laidig JG, Lewis ER, Li J, MacKinnon AL, Parlati F, Rodriguez MLM, Shwonek PJ, Sjogren EB, Stanton TF, Wang T, Yang J, Zhao F, Bennett MK. Antitumor activity of the glutaminase inhibitor CB-839 in triple-negative breast cancer. *Mol Cancer Ther* 2014; 13: 890-901.
- 91 Wolpaw AJ, Dang CV. Exploiting Metabolic Vulnerabilities of Cancer with Precision and Accuracy. *Trends Cell Biol* 2018; 28: 201-212.
- 92 Desideri E, Ciccarone F, Ciriolo MR. Targeting Glutathione Metabolism: Partner in Crime in Anticancer Therapy. *Nutrients* 2019; 11.
- 93 Nishizawa S, Araki H, Ishikawa Y, Kitazawa S, Hata A, Soga T, Hara T. Low tumor glutathione level as a sensitivity marker for glutamate-cysteine ligase inhibitors. *Oncol Lett* 2018; 15: 8735-8743.
- 94 Huang Y, Li W, Su ZY, Kong AN. The complexity of the Nrf2 pathway: beyond the antioxidant response. *J Nutr Biochem* 2015; 26: 1401-1413.

- 95 Kansanen E, Kuosmanen SM, Leinonen H, Levonen AL. The Keap1-Nrf2 pathway: Mechanisms of activation and dysregulation in cancer. *Redox Biol* 2013; 1: 45-49.
- 96 Fox DB, Garcia NMG, McKinney BJ, Lupo R, Noteware LC, Newcomb R. NRF2 activation promotes the recurrence of dormant tumour cells through regulation of redox and nucleotide metabolism. *Nat Metab* 2020; 2: 318-334.
- 97 DeNicola GM, Karreth FA, Humpton TJ, Gopinathan A, Wei C, Frese K, Mangal D, Yu KH, Yeo CJ, Calhoun ES, Scrimieri F, Winter JM, Hruban RH, Iacobuzio-Donahue C, Kern SE, Blair LA, Tuveson DA. Oncogene-induced Nrf2 transcription promotes ROS detoxification and tumorigenesis. *Nature* 2011; 475: 106-109.
- 98 Suzuki T, Motohashi H, Yamamoto M. Toward clinical application of the Keap1-Nrf2 pathway. *Trends Pharmacol Sci* 2013; 34: 340-346.
- 99 Raghunath A, Sundarraj K, Nagarajan R, Arfuso F, Bian J, Kumar AP, Sethi G, Perumal E. Antioxidant response elements: Discovery, classes, regulation and potential applications. *Redox Biol* 2018; 17: 297-314.
- 100 Tomar D, Prajapati P, Lavie J, Singh K, Lakshmi S, Bhatelia K, Roy M, Singh R, Bénard G, Singh R. TRIM4; a novel mitochondrial interacting RING E3 ligase, sensitizes the cells to hydrogen peroxide (H<sub>2</sub>O<sub>2</sub>) induced cell death. *Free Radic Biol Med* 2015; 89: 1036-1048.

- 101 Kumari S, Badana AK, M. MG, G. S, Malla R. Reactive Oxygen Species: A Key Constituent in Cancer Survival. *Biomaker Insights* 2018; 13: 1-9.
- 102 Ishikawa K, Koshikawa N, Takenaga K, Nakada K, Hayashi J. Reversible regulation of metastasis by ROS-generating mtDNA mutations. *Mitochondrion* 2008; 8: 339-344.
- 103 Pascual G, Dominguez D, Benitah SA. The contributions of cancer cell metabolism to metastasis. *Dis Model Mech* 2018; 11.
- 104 Liou GY, Storz P. Reactive oxygen species in cancer. *Free Radic Res* 2010; 44: 479-496.
- 105 Porporato PE, Payen VL, Perez-Escuredo J, De Saedeleer CJ, Danhier P, Copetti T, Dhup S, Tardy M, Vazeille T, Bouzin C, Feron O, Michiels C, Gallez B, Sonveaux P. A mitochondrial switch promotes tumor metastasis. *Cell Rep* 2014; 8: 754-766.
- 106 Conklin KA. Chemotherapy-associated oxidative stress: impact on chemotherapeutic effectiveness. *Integr Cancer Ther* 2004; 3: 294-300.
- 107 Riley PA. Free radicals in biology: oxidative stress and the effects of ionizing radiation. *Int J Radiat Biol* 1994; 65: 27-33.
- 108 Weinberg F, Ramnath N, Nagrath D. Reactive Oxygen Species in the Tumor Microenvironment: An Overview. *Cancers (Basel)* 2019; 11.



- 109 Panieri E, Santoro MM. ROS homeostasis and metabolism: a dangerous liason in cancer cells. *Cell Death Dis* 2016; 7: e2253.
- 110 Jin MZ, Jin WL. The updated landscape of tumor microenvironment and drug repurposing. *Signal Transduct Target Ther* 2020; 5: 166.
- 111 Dias AS, Almeida CR, Helguero LA, Duarte IF. Metabolic crosstalk in the breast cancer microenvironment. *Eur J Cancer* 2019; 121: 154-171.
- 112 Sarmiento-Salinas FL, Delgado-Magallon A, Montes-Alvarado JB, Ramirez-Ramirez D, Flores-Alonso JC, Cortes-Hernandez P. Breast Cancer Subtypes Present a Differential Production of Reactive Oxygen Species (ROS) and Susceptibility to Antioxidant Treatment. *Front Oncol* 2019; 9: 480.
- 113 Shim H, Dolde C, Lewis B, Wu CS, Dang G, Jungmann R. c-Myc transactivation of LDH-A: Implications for tumor metabolism and growth. *Proc Natl Acad Sci U S A* 1997; 94: 6658-6663.
- 114 Pavlova NN, Thompson CB. The Emerging Hallmarks of Cancer Metabolism. *Cell Metab* 2016; 23: 27-47.
- 115 Ying H, Kimmelman AC, Lyssiotis CA, Hua S, Chu GC, Fletcher-Sananikone. Oncogenic Kras maintains pancreatic tumors through regulation of anabolic glucose metabolism. *Cell* 2012; 149: 656-670.

- 116 Yuneva MO, Fan TW, Allen TD, Higashi RM, Ferraris DV, Tsukamoto T. The metabolic profile of tumors depends on both the responsible genetic lesion and tissue type. *Cell Metab* 2012; 15: 157-170.
- 117 Wang H, Xue W, Jiang X. Overexpression of TRIM24 Stimulates Proliferation and Glucose Metabolism of Head and Neck Squamous Cell Carcinoma. *Biomed Res Int* 2018; 2018: 6142843.
- 118 Li AM, Ducker GS, Li Y, Seoane JA, Xiao Y, Melemenidis S, Zhou Y, Liu Y, Vanharanta S, Graves EE, Rankin EB, Curtis C, Massagué J, Rabinowitz JD, Thompson CB, Ye J. Metabolic Profiling Reveals a Dependency of Human Metastatic Breast Cancer on Mitochondrial Serine and One-Carbon Unit Metabolism. *Mol Cancer Res* 2020; 18: 599-611.
- 119 Nilsson R, Jain M, Madhusudhan N, Sheppard NG, Strittmatter L, Kampf C, Huang J, Asplund A, Mootha VK. Metabolic enzyme expression highlights a key role for MTHFD2 and the mitochondrial folate pathway in cancer. *Nat Commun* 2014; 5: 3128.
- 120 Combs JA, DeNicola GM. The Non-Essential Amino Acid Cysteine Becomes Essential for Tumor Proliferation and Survival. *Cancers (Basel)* 2019; 11.
- 121 Rojo de la Vega M, Chapman E, Zhang DD. NRF2 and the Hallmarks of Cancer. *Cancer Cell* 2018; 34: 21-43.
- 122 Chen D, Tavana O, Chu B, Erber L, Chen Y, Baer R. NRF2 Is a Major Target of ARF in p53-Independent Tumor Suppression. *Mol Cell* 2017; 68: 224-232 e224.

- 123 Chen W, Sun Z, Wang XJ, Jiang T, Huang Z, Fang D. Direct interaction between Nrf2 and p21(Cip1/WAF1) upregulates the Nrf2-mediated antioxidant response. *Mol Cell* 2009; 34: 663-673.
- 124 Faraonio R, Vergara P, Di Marzo D, Pierantoni MG, Napolitano M, Russo T. p53 suppresses the Nrf2-dependent transcription of antioxidant response genes. *J Biol Chem* 2006; 281: 39776-39784.
- 125 Pereira E, Burns JS, Lee CY, Marohi T, Calderon D, Wang L . Sporadic activation of an oxidative stress-dependent NRF2-p53 signaling network in breast epithelial spheroids and premalignancies. *Sci Signal* 2020; 13.
- 126 Yu YP, Cai LC, Wang XY, Cheng SY, Zhang DM, Jian WG/. BMP8A promotes survival and drug resistance via Nrf2/TRIM24 signaling pathway in clear cell renal cell carcinoma. *Cancer Sci* 2020; 111: 1555-1566.
- 127 Sayin VI, LeBoeuf SE, Singh SX, Davidson SM, Biancur D, Guzelhan BS/. Activation of the NRF2 antioxidant program generates an imbalance in central carbon metabolism in cancer. *Elife* 2017; 6.
- 128 Mahendralingam MJ, Kim H, McCloskey CW, Aliar K, Casey AE, Tharmapalan P, Pellacani D, Ignatchenko V, Garcia-Valero M, Palomero L, Sinha A, Cruickshank J, Shetty R, Vellanki RN, Koritzinsky M, Stambolic V, Alam M, Schimmer AD, Berman HK, Eaves CJ, Pujana MA, Kislinger T, Khokha R. Mammary epithelial cells have lineage-rooted metabolic identities. *Nat Metab* 2021; 3: 665-681.

- 129 Gong Y, Ji P, Yang YS, Xie S, Yu TJ, Xiao Y, Jin ML, Ma D, Guo LW, Pei YC, Chai WJ, Li DQ, Bai F, Bertucci F, Hu X, Yi-Zhou Jiang, Shao ZM. Metabolic-Pathway-Based Subtyping of Triple-Negative Breast Cancer Reveals Potential Therapeutic Targets. *Cell Metab* 2021; 33: 51-64 e59.
- 130 D'Aniello C, Patriarca EJ, Phang JM, Minchiotti G. Proline Metabolism in Tumor Growth and Metastatic Progression. *Front Oncol* 2020; 10: 776.
- 131 Krishnan N, Dickman MB, Becker DF. Proline modulates the intracellular redox environment and protects mammalian cells against oxidative stress. *Free Radic Biol Med* 2008; 44: 671-681.

## **Vita**

Shucheng Miao “Anna” is the daughter of Xuguang Cheng and Zexun Miao. After completing her work at Tianjin TEDA Maple Leaf International School, TEDA, Tianjin, China in 2014, she entered McGill University in Montreal, Quebec, Canada. She received the degree of Bachelor of Science with an Honor in Pharmacology from McGill in May, 2018. For the next year, she worked as a research technician in Masonic Medical Research Institute, Utica, New York. In August of 2019, she entered The University of Texas MD Anderson Cancer Center UTHealth Graduate School of Biomedical Sciences.

Permanent address:

No.10-1-402, B3 Area Xinghai Square

Dalian, China

116021